UNIVERSITY OF CALIFORNIA

SANTA CRUZ

NANO-OPTO-MECHANICAL TOOLS FOR MULTISCALE BIOMEDICAL APPLICATIONS: FROM EXOSOMES TO RARE CELLS

A dissertation submitted in partial satisfaction

of the requirements for the degree of

DOCTOR OF PHILOSOPHY

in

ELECTRICAL ENGINEERING

by

Xiangchao Zhu

June 2019

The Dissertation of Xiangchao Zhu
is approved by:

_____
Professor Ahmet Ali Yanik, Chair

_____
Professor Holger Schmidt

_____
Professor Marco Rolandi

_____

Quentin Williams
Interim Vice Provost and Dean of Graduate Studies

Table of Contents

List of Figures

List of Tables

Table 1-1. Physical constants of elastic materials used in the ARF function calculation 32

Table 1-2. Basic parameters of the finite element model. 41

Abstract

NANO-OPTO-MECHANICAL TOOLS FOR MULTISCALE BIOMEDICAL APPLICATIONS: FROM EXOSOMES TO RARE CELLS

by

Xiangchao Zhu

We are living in an exciting era of a fast-paced confluence of wide-ranging research fields and technological breakthroughs that are profoundly altering our biomedical practices. In particular, the marriage of micro-nanotechnology and biotechnology is propelling our technical capabilities to new horizons. Despite tremendous progress made over the past 20 years, many challenges still exist for a broad range of biomedical applications spanning from few nanometers to tens of microns.

In this thesis, I aim to address three important biomedical problems at three different length scales. I first present an innovative and low-cost acousto-microfluidic approach that overcomes the diffusion limitations imposed by laminar flow profile in microfluidic channels at a challenging flow regime corresponding to extremely low Reynolds (Re~10^{-4}) and high Péclet (Pe~10^{6}) numbers. Using this novel approach, we achieve immunoaffinity based isolation of cells using a simple rectangular channel without resorting to chaotic mixing processes or magnetic forces. Our acousto-microfluidic method uses a combination of pure and quasi-standing surface acoustic waves that are generated at a safe power (~ 1-10 W/cm^2) and frequency (~10 MHz)

regime comparable to those used in ultrasound imaging (e.g. fetal imaging). By exploiting the local shear forces in the vicinity of the bottom channel boundary (defined capture surface), we achieve selective separation of desired particles/cells using pre-functionalized cell specific biomolecules. We demonstrate selective enrichment of low-abundance T lymphocyte cells with a separation efficiency of about 80% at a high flow rate of 1.2 mL/hr, a separation efficiency that is comparable to most advanced rare cell isolation technologies. In the second part of my thesis (Chapter 2), I introduce a novel nanophotonic approach for enhanced inactivation of multidrug-resistant bacterial pathogens using visible light at 405 nm. To achieve this, I introduce precisely engineered aluminum nanoantenna arrays using a space mapping algorithm enabling inverse design of nanostructures from the desired spectral response. The nanoantenna arrays are optimized using radiative decay engineering principles to maximize the near-field enhancements and photothermal heating at 405 nm, a wavelength which bacteria is extremely sensitive to light and used as an emerging light-based disinfection technology alternative to ultraviolent (UV) light. In our experiments with low illumination intensities (2.5 mW/mm^2), we demonstrate that our aluminum nanoantenna array (ANA) enables rapid eradication (~20 min) of multidrug-resistant *Vibrio Cholerae* biofilms with more than 500-fold inactivation efficiency (~99.995%) with respect to the 405 nm light alone. In the final part of my thesis (Chapter 3), I introduce a subwavelength thick (<200 nm) Optofluidic PlasmonIC (OPtIC) microlens that effortlessly achieves objective-free focusing and self-alignment of opposing

optical scattering and fluidic drag forces for selective separation of exosome size bioparticles at low flow rates (< 5 μm/s). Our optofluidic microlens provides a self-collimating mechanism for particle trajectories with a spatial dispersion that is inherently minimized by the optical gradient and radial fluidic drag forces working together to align the particles along the optical axis. I demonstrate that this facile platform facilitates complete separation of small size bioparticles (i.e., exosomes) from a heterogenous mixture through negative depletion and provides a robust selective separation capability for same size nanoparticles based on their differences in chemical composition. Unlike existing optical chromatography techniques that require complicated instrumentation (lasers, objectives and precise alignment stages), our OPtIC microlenses with a foot-print of 4 μm × 4 μm open up the possibility of multiplexed sorting of nanoparticles on a chip using low-cost broadband light sources (LEDs).

To God
To my father Zhian Zhu, and my mother Hongying Qian

Acknowledgement

I am very grateful for all I have been blessed with an amazing family, wonderful friends, and fantastic mentors.

First, I would like to express my deepest gratitude and appreciation to my thesis advisor, Prof. Ahmet Ali Yanik, for his constant encouragement, infinite patience, continued support, and the opportunity to work in an exciting multi-disciplinary UCSC Nanoengineering lab on a variety of fascinating projects. I would also like to thank Prof. Holger Schmidt and Prof. Marco Rolandi for reading my thesis and being on my defense committee. I am deeply grateful for our collaborators, Prof. Fitnat Yildiz in microbiology and environmental toxicology at UCSC, and Prof. Camilla Forsberg in Biomolecular Engineering at UCSC.

Last but not least, I would like to take this opportunity to sincerely thank my colleagues and friends for their endless support, constructive and insightful discussions. I thank Dr. Thomas Yuzvinsky, Imran Hossain, Dr. Ahmet Cicek, Jianhong Chen, Evan Peterson, Reem Rashid, Matthew Menning, Ahsan Habib, Sierra Catelani, Yixiang Li, Jose Fuentes, Nathan Ng, Christopher Espino, Misbah Khan, Joshua Passmore, Eduardo Hirata, Ali Aljuraidan, Aditya Gumparthi, Melvin Abzun, Joseph Adamson, Mingran Liu, Michael Trebino, Dr. Jin Hwan Park, Haofan Sun, Mustafa Mutlu, Maverick McLanahan, Stephanie Smith-Berdan, Yi Peng, Yuanran Zhu, Peizhi Mai, Jingwen Xue, Le Zheng, Zhiguang Chen.

Chapter 1

Acoustic Drifting Effect: Breaking Mass Transport Barrier and Selective Isolation of Biological Cells in Laminar Flow Microfluidics

This chapter presents an innovative and low-cost acousto-microfluidic approach that overcomes the diffusion limitations imposed by laminar flow profile in microfluidic channels at a challenging flow regime corresponding to extremely low Reynolds ($Re \sim 10^{-4}$) and high Péclet ($Pe \sim 10^{6}$) numbers. Using this novel approach, we achieve immunoaffinity based isolation of cells using a simple rectangular channel without resorting to chaotic mixing processes or magnetic forces. Our acousto-microfluidic method uses a combination of pure and quasi-standing surface acoustic waves that are generated at a safe power (~ 1-10 W/cm^2) and frequency (~10 MHz) regime that is comparable to those used in ultrasound imaging (e.g. fetal imaging). By exploiting the local shear forces in the vicinity of the bottom channel boundary (defined capture surface), we achieve selective separation of desired particles/cells using pre-functionalized cell specific biomolecules. We demonstrate selective enrichment of low-abundance T lymphocyte cells with a separation efficiency of about 80% at a high flow rate of 1.2 mL/hr, a separation efficiency that is comparable to most advanced rare cell isolation technologies.

1.1 Motivation

The capability to analyze cells using small sample volumes are among the most attractive advantages of miniaturized and microfluidic lab-on-a-chip platforms over batch purification techniques [1-4]. In particular, use of microfluidics for efficient isolation of rare cells is of great interest for clinical and precision medicine applications [5, 6]. However, the laminar fluidic flow profile in microfluidic systems poses a fundamental challenge. Translation of micrometer scale cells towards channel surfaces is extremely limited in typical microfluidic channels, preventing efficient use of adhesion-based (immunoaffinity) cell isolation techniques [7, 8]. This limitation, commonly known as mass transport barrier, has received significant attention during the last two decades. Various attempts, including breaking up the fluidic streamlines to enhance diffusion, has been made to overcome it [9, 10]. Yet, there are two main drawbacks present in these approaches severely restricting their practical use for rare cell isolation in blood-based point-of-care diagnostics. First, these fluidic flow only approaches introduce instabilities and turbulence that considerably disrupt the flow dynamics, giving rise to large and uncontrollable local shear stresses near target capture surfaces. As a result, the enhanced shear forces close to channel surfaces lead to reduced adhesion-based surface capture efficiencies. Second, fabrication of these microfluidic devices (such as herringbone, micropost bas-relief structures) are complex and yield unpredictable device characteristics. Since turbulent flow is extremely sensitive to small perturbations in channel features, the operation conditions and efficiencies of these device are extremely susceptible to fabrication imperfections.

Therefore, there is a strong need for alternative strategies that can achieve efficient transport and high-throughput capture of desired bioparticles (e.g. cells) using structures that can be readily fabricated with high-yield at a low-cost .

1.2 Laminar Flow in Microfluidic Channels

Hydrodynamic flow of common liquids in fluidic channels is governed by dimensionless Reynolds numbers, $Re = \rho u D_H/\mu$, where ρ is the density of the fluid, u is average fluid velocity, D_H is the hydraulic diameter ($D_H = 2AB/(A+B)$, A is the width/height of a rectangular duct and B is the height/width of this duct), and μ is the dynamic viscosity of the fluid [11]. Typically, fluidic flow in microfluidic channels corresponds to a low Reynolds number regime, $Re = \rho u D_H/\mu < 1$. For example, flow of water at a velocity of 1 mm/sec in a microfluidic channel of 1000 μm width and 100 μm height leads to a Reynolds number of $Re = 0.1$ [10^3 (kg/m^3) × 10^{-3} (m/sec) × 10^{-4} (m)]/[10^{-3} (Pa·sec)]. Fluidic flow in this regime ($Re < 1$) is mainly controlled by the viscous (Stokes drag) forces rather than the inertial forces (mass acceleration of fluid elements), rendering the pressure driven flow to be strictly laminar and uniaxial. Hence, in the absence of instabilities and turbulence, mixing of fluidic flow between different streamlines is purely diffusive and based on random events. Typically, the flow distance L required for the mixing to take place is characterized by the dimensionless Péclet number ($Pe = uD_H/D$, D is the molecular diffusivity) as in: $L = uD_H^2/D = Pe \times D_H$. This means a flow distance of 20 cm is required to mix proteins (diffusion coefficient $D = 10^{-6}$ cm^2/s) in the microfluidic channel discussed above. As illustrated

in Fig. 1-1, distinct streams of two different solutions filling the opposite halves of a rectangular microfluidic channel are still distinguishable even at the exit port of a very long channel due to limited mixing at this high Peclet number regime (10^6) [8].

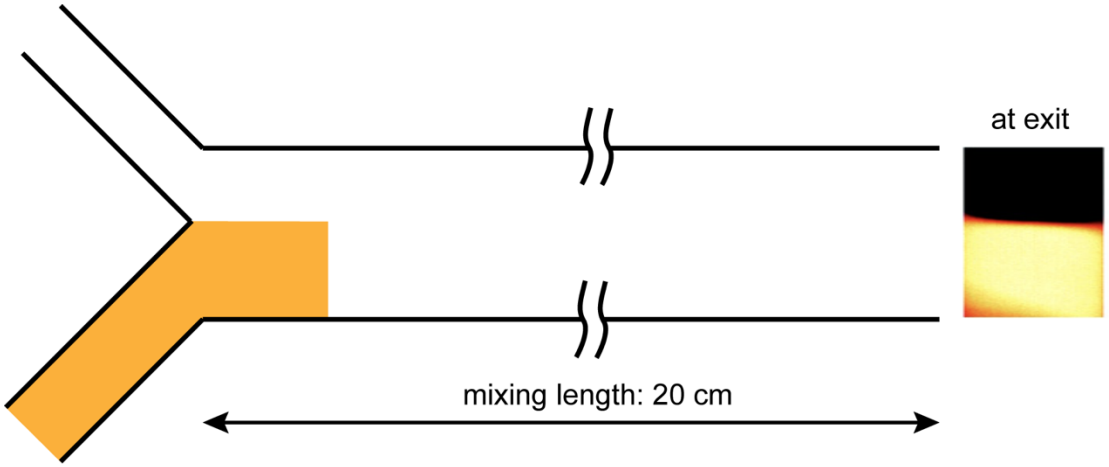

Figure 1- 1. Schematic diagram of mixing two different solutions, one is clear, the other is fluorescent (highlighted in yellow), in a straight and smooth microfluidic channel. At the exit of the channel, negligible mixing of these solutions occurs [8].

For many practical applications, laminar flow profile providing a predictable and controllable fluidic follow in microchannels is advantageous and useful. However, in applications that require translation of micrometer scale targets (4-20 μm) towards microfluidic channel surfaces, laminar flow profile can lead to prohibitively strong mass transport limitations due to low diffusion coefficients (~10^{-9} cm^2/s). For example, for the microfluidic flow conditions discussed above, Péclet number and mixing length for cell size particles can be extremely large, i.e., 10^6 and 200 m, respectively. Therefore, cross-streamline translation of neutrally buoyant particles is absent in the laminar flow regime, leading to same particle distribution seen at the inlet, along the

length, and at the outlet of a microchannel [12]. It should be also noted that fluidic and particle flow Reynolds number differ when fluidic flow of micrometer size particles are considered. When the particle diameter must be taken into account, the Reynolds number for the particle flow is defined as $Re_p = Re_c \times a^2/D_H^2 = \rho u D_H/\mu \times a^2/D_H^2 = \rho u a^2/\mu D_H$, where Re_p is the channel Reynolds numbers. For cell size particles is (10 μm), Re_c and Re_p become 0.1 and 10^{-4} for the microfluidic conditions given above. This extremely low-value particle Reynolds number ($Re_p \sim 10^{-4}$) indicates the impracticality of mixing cells in a laminar flow regime.

1.3 Shear stress and lift force

Viscosity is the measure of a fluid's ability to resist gradual deformation by force or tension. In the laminar flow regime, the fluid dynamics of an incompressible and Newtonian fluid (e.g. water) is dictated by the Hagen–Poiseuille law [11]; the shear stress in the pressure-driven Poiseuille flow is defined by the proportionality relationship with the velocity gradient

$$\tau_{lam} = \eta \frac{du}{dz} \tag{1.1}$$

where τ is the shear stress distribution across the channel cross-section (xz plane in Figure 1-2a), η the viscosity of fluid, u the velocity of the fluid flow. As schematically shown by Fig. 1-2a, fully-developed Poiseuille flow has a parabolic velocity profile, where the fluid velocity is maximum along the center but vanishes along the boundary of the channel. According to the equation (1.1), the corresponding shear stress is maximum along the boundary and minimum along the center of the channel. This flow

conditions causes minimal cross-migration of solid particles (e.g. cells) across the fluidic flow lines as dictated by the Stokes drag law. Hence, particles are kept at a distance from the channel walls close to the center of the channel (Fig. 1-2b).

With the introduction of some instabilities into the Poiseuille flow, the fluid streamlines can be disrupted and the fluid dynamics can transition from laminar to turbulent flow in character, leading to the emergence of a time-dependent chaotic flow behavior in the channel. The turbulent flow corresponds to a large Reynolds number (Re >>1) regime, where the inertial effects become dominant over the viscous (Stokes drag) forces. Turbulent flow is irregular, stochastic, dominated by fluctuations. Accordingly, velocity and pressure fields are a rapid varying random function of time and space [11]. Therefore, averaged or mean values for the velocity and pressure are used to characterize the turbulent flow. Unlike the laminar flow, the shear stress in the turbulent flow is composed of two parts: the viscous and turbulent components

$$\tau_{turb} = \eta \frac{d\overline{u}}{dz} - \rho \delta \overline{u}_i \delta \overline{u}_j \tag{1.2}$$

where τ_{turb} is the shear stress distribution across the channel cross-section ($\underline{xz}$ plane), η the viscosity of fluid, ρ the mass density of the fluid, $\overline{u}$ the mean velocity of the fluid flow, $\overline{u}_i$ and $\overline{u}_j$ the fluctuation about the time–averaged, mean velocity $\overline{u}$. The laminar flow contribution at the channel boundary is consider in equation (1.2) since the tangential stress along the boundary should be also considered [13]. Fig. 1-2a exemplifies a typical turbulent flow profile, where the fluid velocity remains nearly constant in the vicinity of the centerline of the channel (free stream flow layer), slowly

decays towards the channel boundary and eventually vanishes at the boundary (boundary layer flow layer). Between these two adjacent flow layers, rotational eddy currents redirecting the particle flow is established, resulting in a vertical fluctuation that creates momentum exchange or mixing [14]. As illustrated by Fig. 1-2c, irregular fluidic microvortices created by the turbulent flow may facilitate advective transport of particles in an arbitrary way, driving them towards and away from the channels walls. In turbulent flow regime, typical fluidic shear stress along the channel boundary could be two to three orders of magnitude higher than that of the laminar flow. High shear forces can considerably accelerate the particle motion at the channel boundary surface, and significantly reduce the interaction times between the particles and the surface. Hence, there is no simple way to control particle delivery and shear stress using conventional "fluidic flow only" approaches.

In this thesis, I will introduce a novel acousto-microfluidic approach to overcome mass transport limitation and achieve efficient immunoaffinity isolation of cells on microfluidic channel walls. We achieve this without resorting to chaotic fluidic flow and creating high local shear stress along channel boundaries. Instead of using disrupted fluidic flow lines to bring particles on channel walls, we separate particle trajectories from the fluidic flow lines using a perpendicularly acting acoustic force field (F_{ext}), physically pushing particles through the fluidic flow planes towards the channel wall. [15] As illustrated by Fig. 1-2d, our approach is advantageous since the laminar flow profile providing controllable the shear stress along the boundary in a predictable manner is not disrupted. To achieve efficient capturing of particles, we

create a strong enough acoustic radiation force that is not harmful to cells, but strong enough to overcome the fluidic lifting forces, as illustrated by the inset in Fig. 1-2d. [12, 16, 17].

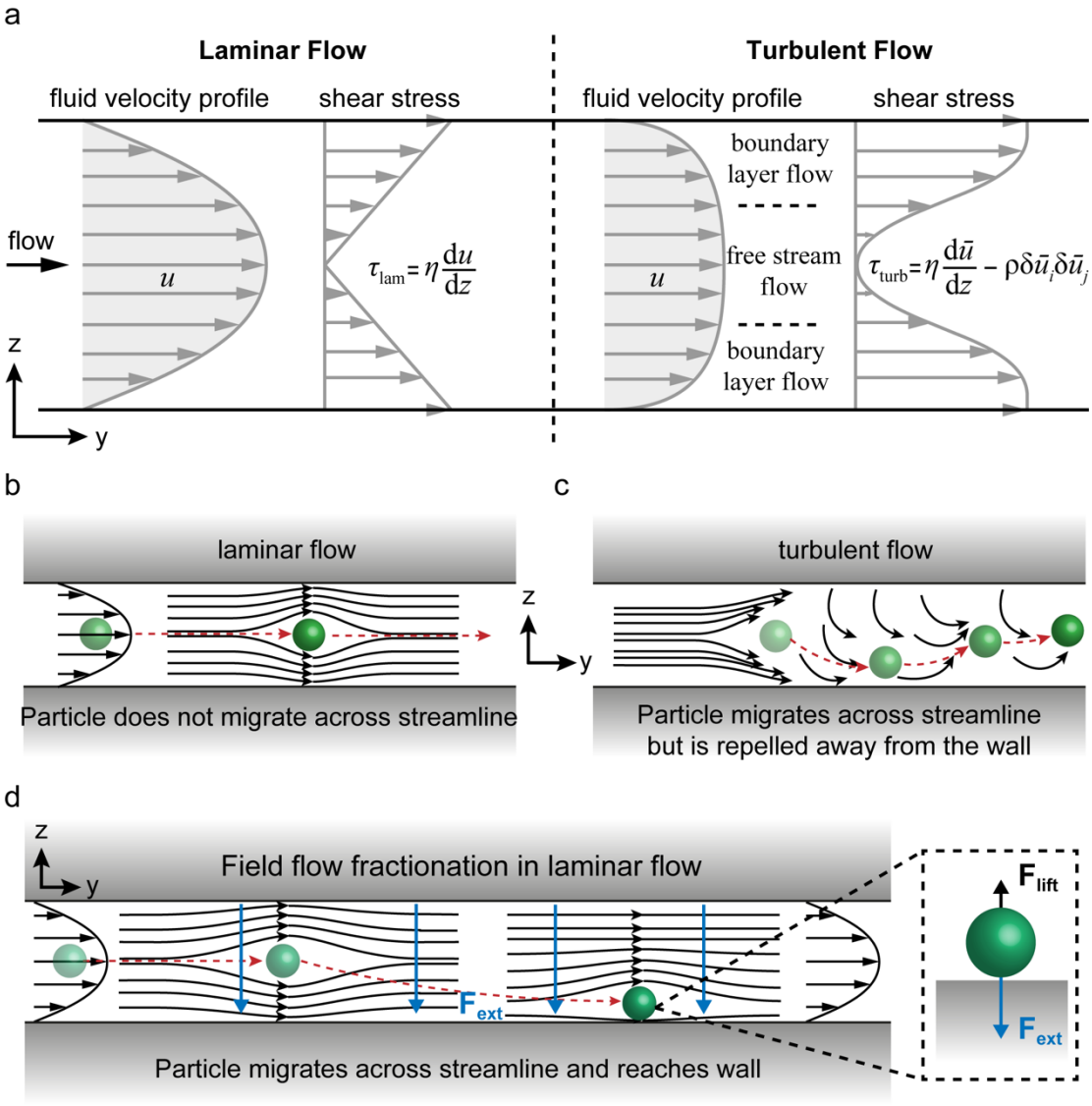

Figure 1-2. (a) Fluid velocity and shear stress distributions in the laminar and turbulent flow regimes. (b) In the laminar flow regime, solid particle does not migrate across fluid streamlines due to the dominant viscous force relative to the inertial one. (c) In

the turbulent flow regime, the established irregular fluidic microvortices enable the particle to migrate across the streamline towards the channel wall. However, strong lift force near the wall repels particle away from the it. (d) Field flow fractionation in laminar flow.

1.4 Overview of ADE Enabled Field Flow Fractionation in Laminar Flow

To date, optical [7, 18], hydrodynamic [2, 19-21], electrostatic [22, 23], electrokinetic [24-27], magnetic [28-30], and acoustic radiation forces [31-35] have been extensively studied for contactless manipulation, sorting, and isolation of bioparticles (e.g., cells, bacteria, exosomes) in microfluidic systems. Among these techniques, acoustic radiation force (ARF) presents some unique opportunities [4, 36]. Minimal absorption of acoustic radiation by biological materials, lack of magnetic labeling agents, and electrokinetic charging effects mean ARF provide a remote, non-harmful, and non-invasive way to handle biological targets [37, 38]. ARF has been used for size-based isolation of bioparticles (bacteria, white blood cells, and tumor cells), or acoustophoresis [31-33, 39] as it can be generated at a power (~ 1 W/cm^2) and frequency (~10 MHz) regime that is similar to ultrasound imaging (e.g. fetal imaging) [4, 31, 40], which is safe to use for cell isolation applications [41, 42]. However, ARF has not been used for overcoming mass transport limitations and immuno-affinity based isolation of cell before.

In this thesis, we introduce a novel phenomenon, acoustic drifting effect (ADE), enabling us to overcome mass transport limitations in the laminar-flow regime and achieve efficient capturing of micrometer scale particles on channel walls. Our ADE platform merges the uniform flow profile and low local shear stress of laminar flow regime with the precise, label-free and contactless bioparticle manipulation capabilities of surface acoustic waves (SAWs). Our platform uses a straight and uniform microfluidic channel that is integrated with a pair of metallic interdigitated transducers (IDTs) that are lithographically deposited on a transparent piezoelectric substrate. By applying a sinusoidal radio frequency (RF) voltage signal to the IDTs, a three-dimensional (3D) ARF field is created within the channel (Fig. 1-3a). By engineering the device dimensions and using proper channel materials, the 3D ARF potential, or Gor'kov potential [43], is precisely configured with minimum radiation force potential region at the bottom channel boundary, and maximum radiation force potential in the middle of the channel. Solid bioparticles moving along the microfluidic channel, when exposed to this precisely defined potential field, are pushed towards lower radiation force potential regions. Furthermore, the acoustic streaming in our devices is negligibly small and do not disrupt the laminar flow profile. ADE effect based capturing of particles is illustrated in Fig. 1-3a, where a randomly distributed green particles injected from the channel inlet . As these green particles translate through the 3D ARF region, they move towards the centerline of the channel in the *xy* plane of the fluid channel (Fig. 1-3b) and simultaneously follow a path towards the bottom channel boundary in the *yz* plane of the fluid channel (Fig. 1-3c). With sufficiently strong ARFs, the “wall

effect" induced lift force exerted on the particles near the channel boundary are overcome. This relatively strong ARF enables the particles to drift closer towards and eventually to arrive on the substrate. To capture the particles selectively on the substrate, a well-established receptor-ligand bond chemistry is exploited. Particles are successfully arrested on the surface of the piezoelectric substrate that is pre-functionalized with the complementary molecules (Fig. 1-3c).

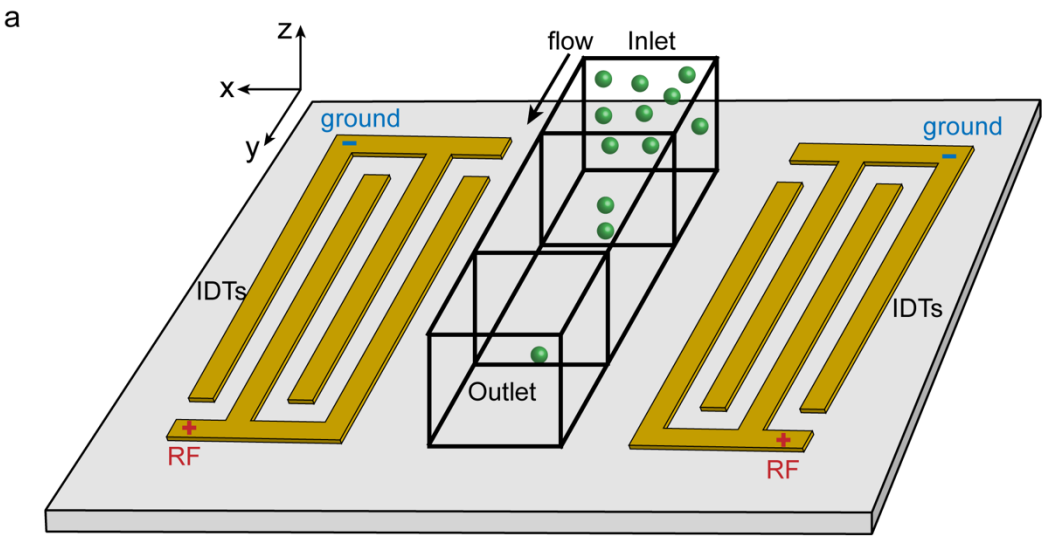
a
z
x
y
flow
Inlet
ground
ground
IDTs
IDTs
Outlet
RF
RF

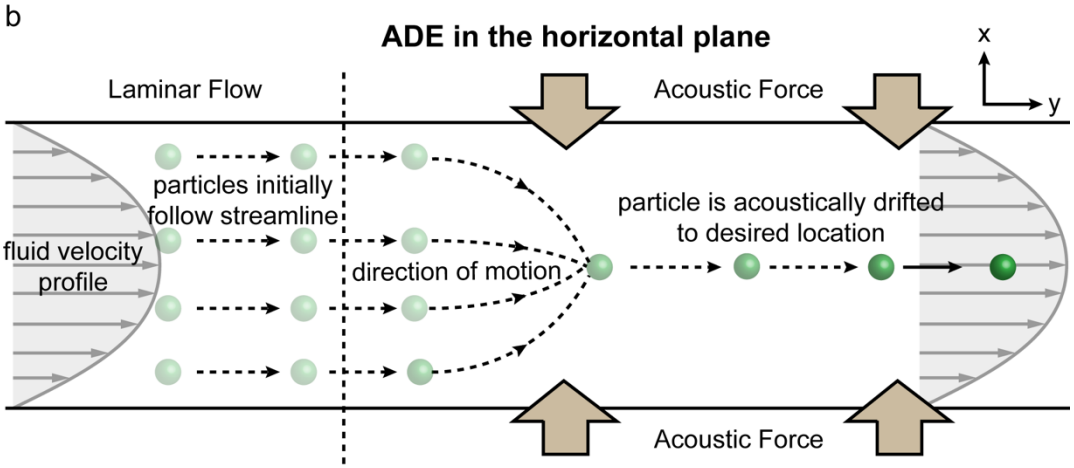
b
ADE in the horizontal plane
x
y
Laminar Flow
Acoustic Force
particles initially
follow streamline
fluid velocity
profile
direction of motion
particle is acoustically drifted
to desired location
Acoustic Force

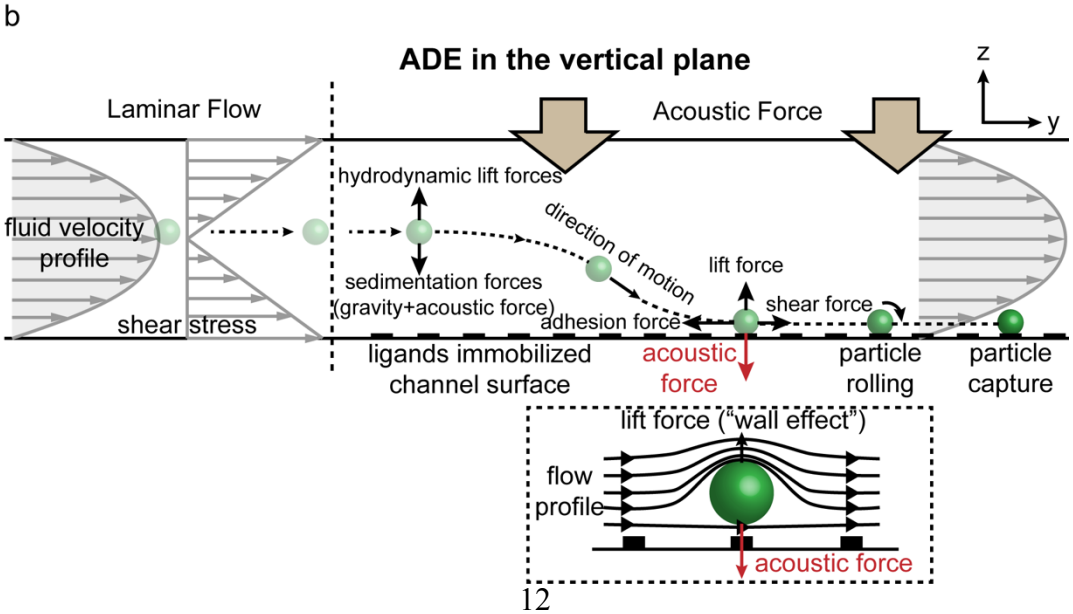
b
ADE in the vertical plane
z
y
Laminar Flow
Acoustic Force
hydrodynamic lift forces
fluid velocity
profile
direction of motion
lift force
sedimentation forces
(gravity+acoustic force)
shear force
adhesion force
shear stress
ligands immobilized
channel surface
acoustic
force
particle
rolling
particle
capture
lift force ("wall effect")
flow
profile
acoustic force

Figure 1-3. (a) The ADE platform is composed of a straight and rectangular microfluidic channel and a pair of metallic interdigitated transducers (IDTs) that are lithographically deposited on a transparent piezoelectric substrate with high electro-mechanical coupling efficiencies. By applying a sinusoidal radio frequency voltage signal to the IDTs, a 3D ARF field is created within the channel, resulting in precise alignment of randomly introduced green particles. (b) Green particles entering the 3D ARF region move towards the centerline of the channel along the *xy* plane and (c) follow a path towards the bottom channel boundary along the *xz* plane. Using a standard receptor-ligand adhesive bonding mechanism enables us to capture and arrest the green particles on the piezoelectric substrate surface.

1.5 Acoustofluidics

1.5.1 Interdigitated Transducers (IDTs) and Surface Acoustic Wave (SAW)

In a linear piezoelectric material, mechanical strain S and electric field E are coupled to each other through constitutive equations [44]:

$$\begin{aligned} T &= -e^T \cdot E + C^E : S \\ D &= \varepsilon^S \cdot E + e : S \end{aligned} \tag{1.3}$$

where T and S are the stress and strain vectors, D is the vector of electric displacement, ε^S is the matrix of the dielectric constants at constant strain, and C^E is the stiffness matrix at constant electric field. Also, e is the matrix of piezoelectric stress constants.

Through this coupling mechanism, Rayleigh waves that are composed of elliptical displacement of atoms (mechanical oscillations) can be generated on piezoelectric substrates by applying a spatially modulated RF electric signal using an IDT (as shown in Fig. 1-4a). These Rayleigh waves, known as surface acoustic waves (SAWs), are bound to the interface between a semi-infinite solid substrate and the surrounding medium [45, 46]. In order to generate pure Rayleigh waves, a specific wafer cut is carefully chosen [47]. Meanwhile, the thickness of substrate must be at least one acoustic wavelength in order to prevent Lamb wave excitations [48]. Generally, the efficient generation of Rayleigh waves requires utilization of proper crystalline orientation of an anisotropoc piezoelectric substrate. Substrates with high electromechanical coupling coefficients are preferred to achieve high power conversion efficiencies from RF electrical input to propagating SAWs [45, 49]. As experimentally demonstrated, 128° YX $LiNbO_3$ turns out to be the best wafer cut for the applications of manipulation, sorting, and isolation of bioparticles [31, 32, 46]. When IDT finger width and spacing are both $\lambda/4$, λ being the wavelength, an applied RF signal excites a SAW with λ, as shown in Fig. 1-4a.

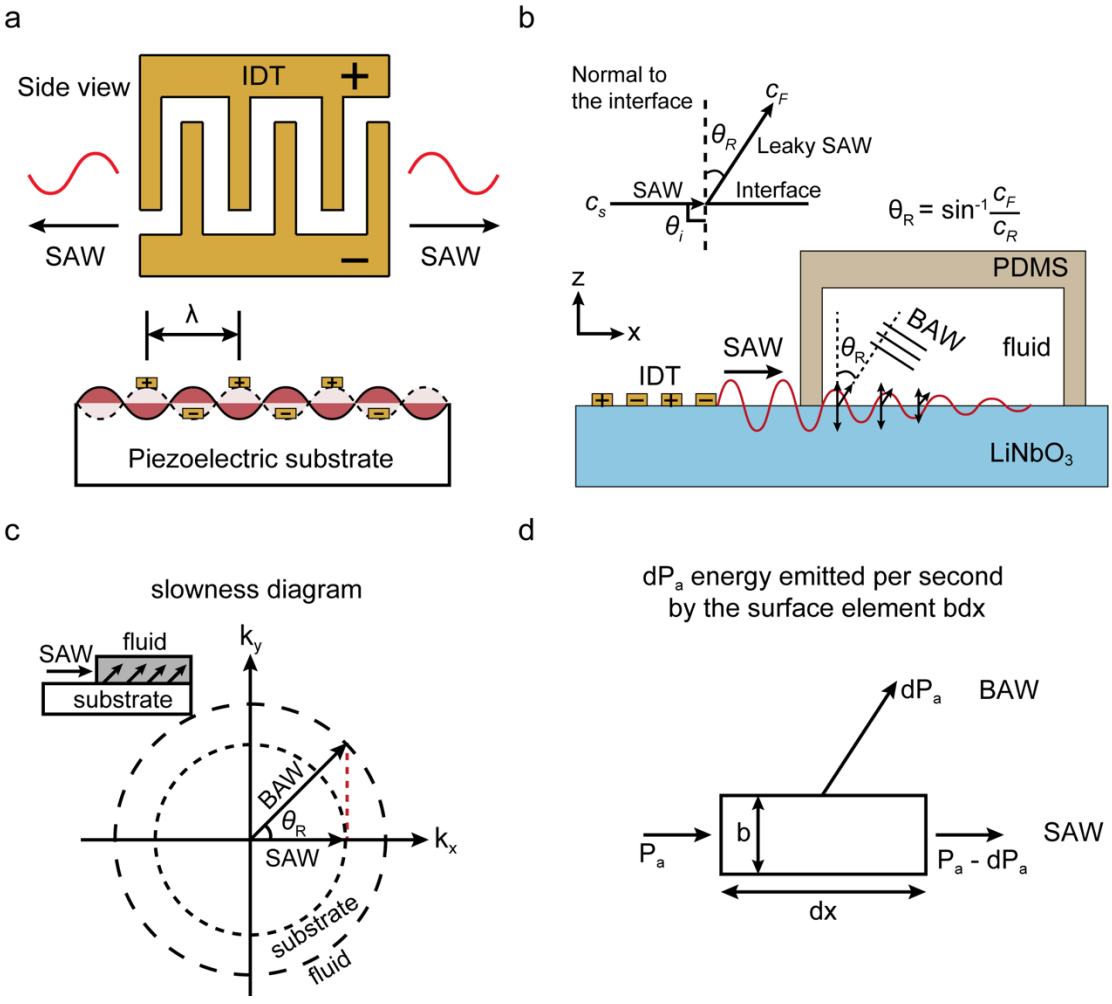

Figure 1-4. Use of piezoelectric substrates. (a) A metallic IDT deposited on the piezoelectric substrate generates SAWs that propagate along the substrate surface in both directions when an RF signal is applied to it. (b) The surface bound SAWs can couple to fluid to form longitudinal, leaky BAW responsible for the radiative acoustic force acting on particles. Leaky SAW propagates in the fluid at the Rayleigh angle (θ_R). (c) Wave number slowness diagram. (d) Energy balance for an infinitesimal surface element *dx* during an infinitesimal time *dt* due to coupling of the Rayleigh type SAW to the fluid.

1.5.2 Fluid Loading Induced Surface Acoustic Wave Radiation

The stress-free boundary between air and piezoelectric substrate leads to the strong energy localization and minimal attenuation of the SAWs traveling along the substrate. However, when the piezoelectric surface is loaded with a fluid, the boundary condition changes lead to leaking of the SAWs into the fluid medium at a Rayleigh angle $\theta_R = \sin^{-1}(C_F/C_R)$ (C_F and C_R are the sound speeds of fluid and solid media, respectively) to the substrate normal (Fig. 1-4b) [50]. This wave refraction phenomenon originates from the phase matching condition between the surface bound Rayleigh wave and the bulk wave in the fluid, which can be explained through the acoustic Snell's law given above [50]. In principle, acoustic wave refraction enables transfer of mechanical energy from angstrom scale oscillations on the piezoelectric surface to pressure acoustic waves, or bulk acoustic waves (BAWs) in fluid. The wavelength of the BAWs propagating from the boundary into the fluid at the Rayleigh angle is given as $\lambda_{BAW} = \lambda \sin\theta_R$ (Fig. 1-4b). The radiation angle θ_R is obtained by conserving the horizontal wave vector component and can be geometrically determined using a wave number slowness curve diagram (Fig. 1-4c) [51]. As demonstrated by Dransfeld et.al, the normal component of SAWs is responsible for launching of the BAWs while the tangential one weakly couples to the fluid by viscosity [52]. As shown in Fig. 1-4d, the launching of BAWs causes an exponential decay of SAWs, which can be directly characterized by the energy attenuation

$$\alpha_L = \frac{1}{P_a}\frac{dP_a}{dx} = \frac{\rho_F C_F}{\rho_R C_R \lambda_R} \tag{1.4}$$

where α_L is the attenuation coefficient, λ_R the acoustic wavelength, ρ_F and ρ_R, C_F and C_R the densities and acoustic velocities of fluid and piezoelectric substrate, respectively. For 128° YX lithium niobate substrate and water medium, α_L is about 1/12 λ_R. Hence, the attenuation length $1/\alpha_L$ over which the amplitude of SAWs decays to 36% of its initial value only depends on the SAW wavelength.

Considering the ultrasonic SAWs at frequencies of 1-100 MHz, this attenuation length $1/\alpha_L$ turns out to be a very small quantity, which is only on the orders of magnitude from tens to hundreds of micrometers. Hence, it is not practical to implement SAW in a macroscopic scale fluidic system (centimeters) as the wave energy already exponentially decays out after propagating only for a short distance [50]. Nevertheless, effective energy transport from SAWs to BAWs becomes attainable in microfluidic regimes where cross-sectional widths are comparable to the SAW attenuation lengths at MHz frequencies. **It is this characteristic acoustic mode conversion that makes SAWs excellent choices for efficient energy transfer into microfluidics (droplets, cavity)** [45, 46, 50].

In addition to the attenuation due to energy coupling between the SAW and the fluid, there are also frictional losses due to transversal movement of substrate. This attenuation factor is given by [53]

$$\alpha_s = \frac{\left(\rho_F \eta \frac{\omega^3}{2}\right)^{\frac{1}{2}}}{4\pi^2 \rho_R C_R^2} \tag{1.5}$$

where η is viscosity of the fluid and and ω is the SAW frequency. For 128° YX lithium niobate substrate and water medium, α_S is three to four orders of magnitude smaller than α_L at ultrasonic frequencies (1-100 MHz), indicating minimal SAWs energy losses. This frictional loss is trivial except for exceedingly high SAW frequency since it scales with one and a half power of the frequency ($\alpha_S \propto \omega^{3/2}$).

1.5.3 Acoustophoresis – Critical Particle Size

In acoustofluidics, suspensions of microparticles are typically subject to two forces of acoustic origin: Stokes drag force due to acoustic streaming and the acoustic radiation force (ARF) due to the scattering and absorption of incident acoustic waves by the particles [54, 55]. These two forces are nearly equal in strength at a critical particle size [55]

$$a_c = \sqrt{\frac{24\mu}{\Phi\omega}} \tag{1.6}$$

where a_c is the critical particle diameter, μ the dynamic viscosity of the fluid, Φ the acoustic contrast factor between the particle and fluid, and ω the angular frequency of the acoustic wave. This theoretical threshold condition enables us identify dominant component or the relative weight of these two acoustic forces. For example, for a polystyrene particle that is immersed in a water medium at room temperature, the parameters Φ and μ are found to be approximately 0.165 and 9×10^{-7} m^2/s. For an

acoustic wave frequency of 10 MHz, the critical particle diameter is approximately 1.4 μm. According to this scenario, when particles have comparable dimensions to the human cells such as red blood cells (~4 μm) or white blood cells (~10 μm), their motion is dominated by the ARF. On the other hand, the behavior of small particles, such as viruses (~100-500 nm) or exosomes (~100-300 nm), is controlled by the hydrodynamic viscous force (acoustic streaming). For any given microfluidic environment and target bioparticles, the crossover from ARF-dominated to streaming-dominated acoustophoresis can be readily tuned by adjusting the frequency (or wavelength) of the acoustic wave.

1.5.4 Acoustic Streaming Based Acoustophoresis

In essence, acoustic streaming flow is a consequence of the viscous attenuation of an acoustic wave in a fluid [56]. In the case of a piezoelectric substrate bound SAW radiating energy into the fluid, the normal component of the radiated energy is absorbed by the fluid at a rate that is proportional to the square of the SAW frequency, causing the amplitude of the acoustic wave to attenuate with propagation distance from the substrate-fluid boundary [56]. This loss of acoustic energy induces continuous pressure and velocity oscillations in the fluid, resulting in a finite time-averaged momentum flux [56, 57]. This flux forms a fluid jet, followed by a vorticity that eventually generates a fluid circulation pattern within the entire fluid compartment. This type of acoustic streaming is called “quartz wind”, later named as Eckart streaming [58]. For the BAW

that propagates away from the surface along its normal axis, its attenuation coefficient in the Eckart streaming flow is given by [59, 60]

$$\alpha_E = \frac{\left(\frac{4}{3}\mu + \mu'\right)\omega^2}{\rho_F C_F^3} \tag{1.7}$$

where μ and μ' are the dynamic and bulk viscosities of the fluid. Clearly, the attenuation length $1/\alpha_E$ inversely scales with the square of ω. Therefore, the strength of the Eckart streaming can be well controlled by adjusting the SAW frequency.

Figure 1-5 compares three different attenuation lengths $1/\alpha_L$, $1/\alpha_E$, $1/\alpha_S$ over a broad SAW frequency range. The ARF [31, 32, 45, 46, 61] and acoustic streaming [34, 54, 59, 62] based bioparticle acoustophoresis are outlined in red and blue, respectively. For ARF (acoustic streaming) based acoustophoresis, the attenuation lengths $1/\alpha_L$ and $1/\alpha_E$ are larger (smaller) than the characteristic channel length scales (indicated by the horizontal dashed line). In addition, the frictional losses are much higher in the acoustic streaming regime than those in the ARF regime. Therefore, Figure 1-5 provides a clear guide on the selection of the appropriate SAW frequencies and channel length scales for specific acoustophoresis applications. At low frequencies (<100 MHz), ARF dominates.

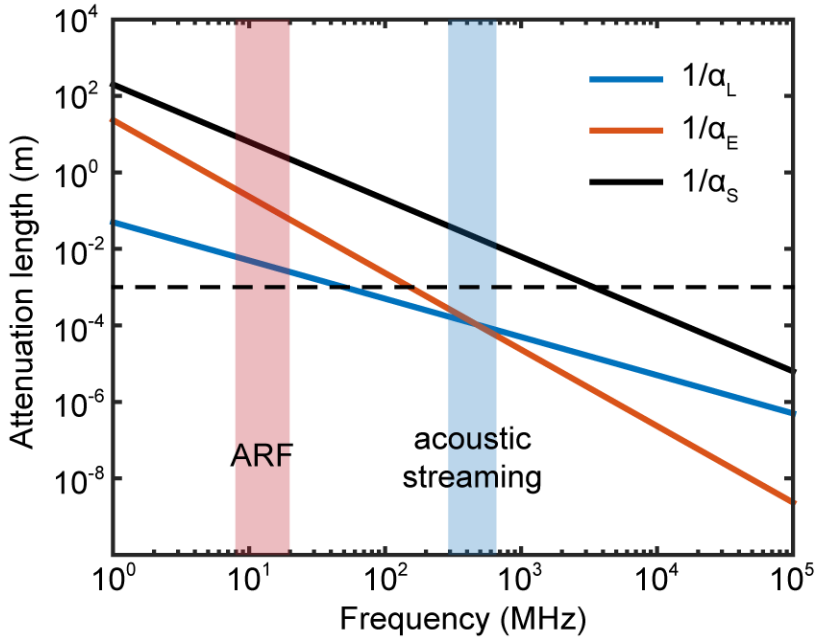

Figure 1-5. Attenuation at the piezoelectric substrate/fluid interface. Blue and red lines represent the attenuation lengths at the fluid/substrate interface and in the fluid, respectively. Black line represents the frictional losses. Dashed line represents the typical length scale for the microfluidic chambers that are used in acoustophoresis.

While the normal component of the BAWs induces the Eckart streaming flow in the bulk of the fluid, its tangential component also induces two types of acoustic streaming flows in the fluid, one is Schlichting streaming in the boundary layer, the other Rayleigh streaming within the bulk of the fluid [63]. The boundary layer driven acoustic streaming results from a steep acoustic velocity gradient that is formed normal to the substrate boundary (Schlichting streaming). This powerful local streaming generates counter rotating streaming vortices within the fluid bulk (Rayleigh streaming). Typically, the vortices emerge in the form of a vortex-anti-vortex pair per

half acoustic wavelength along the direction of acoustic propagation that is parallel to the substrate. These streaming effects are particularly pronounced under the condition that [56, 64]

$$\lambda \gg L \gg \delta_v \tag{1.8}$$

where λ is the acoustic wavelength, L is the characteristic length scale of the fluid compartment, δ_v is the viscous penetration depth that is given by $\delta_v = \sqrt{2\mu/\omega}$. For acoustic waves of 10 MHz operating frequency propagating in a water chamber, δ_v is approximately 1 μm. The Schlichting and Rayleigh streaming will be more prominent for the fluid compartment with length scales (e.g. chamber width) smaller than 150 μm. In a SAW based acousto-fluidic system, the radiated bulk acoustic waves propagate at a large angle 90°-θ_R to the substrate surface ($\theta_R \approx 22°$ for the acoustofluidic system that is comprised of water and lithium niobate), as a result most of the acoustic energy (> 90%) propogates along the perpendicular direction to the substrate surface. Thus the Schlichting streaming plays less of a role compared to the Eckart streaming in the SAW-based microfluidics. In acoustic streaming based bioparticle acoustophoresis, the Eckart acoustic streaming is mainly responsible for the observed fluid circulation and vortices. Using fluorophores tagged bioparticles of small size comparable to the acoustic wavelength provides an effective means to visualize acoustic streaming patterns and characterize fluid dynamics under a fluorescent microscope. The strength of the acoustic streaming originates from the time-averaged acoustic body force by carefully taking into account both attenuation lengths ($1/\alpha_E$ and $1/\alpha_L$) and acoustic reflections off channel boundaries, which is given by [54, 59]

$$F_B = \rho_F \alpha_E A^2 \omega^2 \tag{1.9}$$

where A is the mechanical displacement that includes attenuation terms both along the substrate/fluid interface and in the fluid and reflection coefficients off channel boundaries. This relation indicates that acoustic streaming effect can be enhanced using large SAW frequencies, which allows even smaller particles to be manipulated.

1.5.5 Acoustic Radiation Force (ARF) Based Acoustophoresis

When incident acoustic pressure waves are absorbed or reflected by particles in a fluid medium, an acoustic radiation force (ARF) acting on the particles arises. In principle, ARF is divided into two types, primary and secondary forces. The primary ARF originates from the interaction between particles and acoustic fields. While the secondary ARF (so called Bjerknes forces [65]) is a consequence of the coupling between the acoustic fields scattered by the neighboring particles, leading to either repulsive or attractive particle-particle interactions. The early theoretical studies of the ARF phenomenon dates back to the nineteenth century. In 1934, King presented the first landmark comprehensive theoretical studies of primary ARFs on rigid spheres that are freely suspended in an non-viscous fluid medium with both a traveling plane and standing acoustic waves [66]. He assumed the spheres to be much smaller than the wavelength of the acoustic wave. King discovered that the direction of the ARF shows dependence on the density ratio of the rigid sphere with respect to the fluid medium. This observation was in an excellent agreement with earlier experimental results. Later

in 1955, Yosioka and Kawasima considered the particle compressibility and extended King's theoretical analysis [67]. In 1962, Gor'kov adopted a long wavelength approximation and reformulated the ARF on small compressible spherical spheres in a standing acoustic wave field [43]. These earlier theories were largely restricted to particles that are considerably smaller than acoustic wavelengths, thus little was known about how acoustic energy absorption by relatively large elastic particles would influence the ARF acting on them. A few years later, Hasegawa and Yosioka [68] and Hasegawa [69, 70] developed a theoretical approach that takes into account particle elasticity and generalized the theory for arbitrary size particles. Although this approach is still limited to modeling the particle behavior in inviscid fluid, it is approximately correct for particles that are considerably larger than the viscous penetration depth of the acoustic boundary layer [56, 71]. The viscous penetration depth arising from the time-averaged stress can be approximated using [71]

$$\delta = \sqrt{\frac{2\rho_0\eta}{\omega}} \tag{1.10}$$

where ω is the angular frequency of the acoustic wave. For acoustic waves with ultrasonic frequencies, for example, at 10 MHz, δ is roughly 0.2 μm. Hence, the Hasegawa's theory holds for the calculation of ARFs acting on particles of size larger than 0.2 μm. The subsequent sections provide detailed descriptions of the theories used for analytical calculations of ARFs acting on elastic sphere of arbitrary size in both a plane traveling and standing acoustic waves based on Hasegawa's foundational work [68-70, 72].

1.6 Acoustic Radiation Force

1.6.1 Plane Traveling Acoustic Wave

As shown in Fig. 1-6a, an elastic, isotropic and spherical particle (outlined in green) is immersed in an inviscid compressible fluid. According to the above equation (1.10), the fluid can be assumed to be non-viscous when the viscous penetration depth (thickness of the white area) of the sphere is much smaller than the particle size (the red area). The ARF on the elastic sphere in a plane progressive acoustic wave (or traveling wave) can be analytically calculated according to Hasegawa's work [68, 69]. According to the equation of motion

$$\left(\lambda+2\mu\right)\nabla\left(\nabla\cdot\vec{u}\right)-\mu\left(\nabla\times\vec{u}\right)=\rho\frac{\partial^2\vec{u}}{\partial t^2} \tag{1.11}$$

where λ and μ are Lame's constants, $\vec{u}$ the displacement, t the time, ρ the density of the particle. Assuming the displacement $\vec{u}$ to be composed of two parts: a scalar potential ψ and a vector potential $\vec{A}$, then

$$\vec{u}=-\nabla\psi+\nabla\times\vec{A} \tag{1.12}$$

where ψ and $\vec{A}$ are given by the following forms in spherical coordinate systems (r, θ, φ)

$$\psi=\sum_{n=0}^{\infty}a_n j_n\left(k_1 r\right)P_n\left(\cos\theta\right)e^{i\omega t} \tag{1.13}$$

$$A_\varphi=\sum_{n=0}^{\infty}b_n j_n\left(k_2 r\right)\frac{d}{d\theta}P_n\left(\cos\theta\right)e^{i\omega t} \tag{1.14}$$

where A_φ is the φ component of the vector potential $\vec{A}$, ω the angular frequency of the incident acoustic wave, k_1 and k_2 the wave vectors that can be calculated from the relationships: $k_1 = \omega/c_1$, $k_2 = \omega/c_2$ (c_1 and c_2 are the compressional and shear sound velocities in the solid sphere), j_n the spherical Bessel function of the order n, $P_n(\cos\theta)$ is the Legendre Polynomial. Velocity potentials of the incident and the scattered acoustic waves can be written as

$$\phi_i = M\sum_{n=0}^{\infty}(2n+1)(-i)^n j_n(kr)P_n(\cos\theta)e^{i\omega t} \tag{1.15}$$

$$\phi_s = M\sum_{n=0}^{\infty}c_n(2n+1)(-i)^n h_n^2(kr)P_n(\cos\theta)e^{i\omega t} \tag{1.16}$$

where M is the complex amplitude of the incident velocity and k is the propagation constant, c_n the scattering coefficient of n^{th} partial wave, and h_n^2 the spherical Hankel function of second kind:

$$h_n^2 = j_n - in_n \tag{1.17}$$

where n_n is the spherical Neumann function of order n. The velocity potential outside the sphere, may be written as

$$\phi = \phi_i + \phi_s \tag{1.18}$$

The scattering coefficient c_n is determined after laborious but straight forward calculations from the appropriate boundary conditions at the surface of the sphere, and is shown in the following form

$$c_n = \frac{-F_n j_n(x) - xj_n'(x)}{F_n h_n^2(x) - xh_n^{2'}(x)} \tag{1.19}$$

where $x = ka$, a being the radius of the sphere. For a solid elastic sphere,

$$F_n = \frac{x_2^2 \rho \left(A_n - B_n \right)}{2\rho^* \left(D_n - E_n \right)} \tag{1.20}$$

where

$$A_n = \frac{n j_n(x_1) - x_1 j_{n+1}(x_1)}{\left(n-1 \right) j_n(x_1) - x_1 j_{n+1}(x_1)} \tag{1. 21}$$

$$B_n = \frac{2n\left(n+1 \right) j_n(x_2)}{\left(2n^2 - x^2 - 2 \right) j_n(x_2) + 2x_2 j_{n+1}(x_2)} \tag{1. 22}$$

$$D_n = \frac{\left[\frac{x_2^2}{2} - n\left(n-1 \right) \right] j_n(x_1) - 2x_1 j_{n+1}(x_1)}{\left(n-1 \right) j_n(x_1) - x_1 j_{n+1}(x_1)} \tag{1. 23}$$

$$E_n = \frac{2n\left(n+1 \right)\left[\left(1-n \right) j_n(x_2) + x_2 j_{n+1}(x_2) \right]}{\left(2n^2 - x^2 - 2 \right) j_n(x_2) + 2x_2 j_{n+1}(x_2)} \tag{1. 24}$$

with

$$x_1 = cx / c_1 \tag{1. 25}$$

$$x_2 = cx / c_2 \tag{1. 26}$$

where ρ and ρ^* are the densities of the sphere and the surrounding fluid, c_1 and c_2 being the velocities of compressional and shear waves in the solid sphere. α_n and β_n are the real and imaginary parts of c_n, respectively, and are expressed as

$$\alpha_n = -G_n^2 / \left(G_n^2 + H_n^2 \right) \tag{1. 27}$$

$$\alpha_n = -G_n^2 / \left(G_n^2 + H_n^2 \right) \tag{1. 28}$$

where

$$G_n = \left(F_n - n\right) j_n(x) + x j_{n+1}(x_1) \tag{1. 29}$$

$$H_n = \left(F_n - n\right) n_n(x) + x n_{n+1}(x_1) \tag{1. 30}$$

The acoustic radiation force <*F*> on a boundary moving with small velocity of the first order was calculated by Yosioka and Kawasima [67]

$$\langle F \rangle = -\langle \iint_{S_0} \rho\left(q_n n + q_t t\right) q_n dS \rangle + \langle \iint_{S_0} \frac{1}{2} \rho \vec{q}^2 \vec{n} dS \rangle - \langle \iint_{S_0} \frac{1}{2} \frac{\rho}{c^2} \phi^2 n dS \rangle \tag{1.31}$$

where S_0 is the boundary at its equilibrium position, ϕ the first-order velocity potential, $\vec{q}$ the first-order particle velocity in the surrounding fluid (=-$\nabla\phi$), $q_n n$ and $q_t t$ the normal and the tangential component of the particle velocity, and <> a notation representing the time average over a certain full wave oscillaton period. When the boundary is spherical (radius a) and the acoustic field is axially symmetrical with respect to the direction $\theta = 0$, the radiation force along $\theta = 0$ is given by

$$\langle F \rangle = \langle F_r \rangle + \langle F_\theta \rangle + \langle F_{r\theta} \rangle + \langle F_t \rangle \tag{1. 32}$$

where

$$\langle F_r \rangle = -\pi a^2 \rho \int_0^\pi \left(\frac{\partial \phi}{\partial r} \right)^2_{r=a} \sin\theta \cos\theta d\theta \tag{1. 33}$$

$$\langle F_\theta \rangle = \pi \rho \int_0^\pi \left(\frac{\partial \phi}{\partial r} \right)^2_{r=a} \sin\theta \cos\theta d\theta \tag{1. 34}$$

$$\langle F_{r\theta} \rangle = 2\pi a \rho \int_0^\pi \left(\frac{\partial \phi}{\partial r} \right)_{r=a} \left(\frac{\partial \phi}{\partial \theta} \right)_{r=a} \sin^2\theta d\theta \tag{1. 35}$$

$$\langle F_t \rangle = -\frac{\pi a^2 \rho}{c^2} \int_0^\pi \left(\frac{\partial \phi}{\partial r} \right)^2_{r=a} \sin^2\theta \cos\theta d\theta \tag{1. 36}$$

After laborious but straightforward calculations,

$$\langle F_p \rangle = \pi a^2 \bar{E} Y_p \tag{1. 37}$$

where

$$\bar{E} = \frac{1}{2} \rho k^2 M^2 \tag{1. 38}$$

and Y_p is a dimensionless parameter defined as the acoustic radiation force of the sphere per unit cross section and unit mean energy density

$$Y_p = -\frac{4}{x^2} \sum_{n=0}^{\infty} (n+1) \left[\alpha_n + \alpha_{n+1} + 2\left(\alpha_n \alpha_{n+1} + \beta_n \beta_{n+1}\right) \right] \tag{1. 39}$$

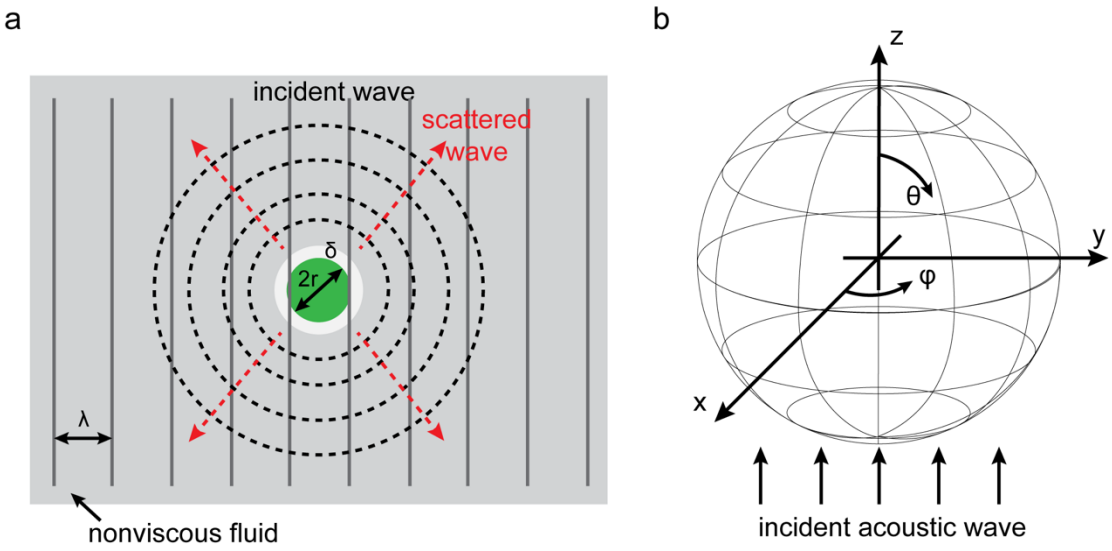

Figure 1-6. (a) A schematic representation of an incident progressive traveling wave scattering off a spherical elastic particle (outlined in green). (b) The velocity potential ϕ is expressed in a system of spherical coordinates (r, θ, φ).

1.6.2 Plane Standing Acoustic Wave

For standing acoustic wave of angular frequency ω is incident upon an elastic sphere in an inviscid fluid medium. In a spherical coordinate system (r, θ, φ), velocity potentials of the incident and the scattered acoustic waves are different than that of the traveling wave case [70]

$$\phi_i = M\sum_{n=0}^{\infty}\left(2n+1\right)\left(-i\right)^n \delta_n j_n(kr)P_n(\cos\theta)e^{i\omega t} \tag{1. 40}$$

$$\phi_i = M\sum_{n=0}^{\infty}\left(2n+1\right)\left(-i\right)^n \delta_n j_n(kr)P_n(\cos\theta)e^{i\omega t} \tag{1. 41}$$

where

$$\delta_n = e^{-ikh} + \left(-1\right)^n e^{ikh} \tag{1. 42}$$

where h is the distance at which the center of the elastic sphere is away from a velocity potential antinode of the plane standing acoustic wave. Using the same equations (1.32-1.36) to calculate the ARF under the standing wave field, after laborious but straight calculations, the time averaged primary ARF on the elastic sphere in a standing wave field is obtained as:

$$\langle F_{st}\rangle = \pi a^2 \bar{E} Y_{st}\sin\left(2kh\right) \tag{1. 43}$$

where Y_{st} is the radiation force function of the sphere for the standing wave

$$Y_{st} = -\frac{8}{x^2}\sum_{n=0}^{\infty}\left(n+1\right)\left(-1\right)^{n+1}\left[\beta_n\left(1+2\alpha_{n+1}\right)-\beta_{n+1}\left(1+2\alpha_n\right)\right] \tag{1. 44}$$

1.6.3 Numerical Examples of ARF for Plane Traveling and Standing Acoustic Waves

The ARF functions given by equations (1.39) and (1.44) are evaluated for solid spheres of different materials with the corresponding physical constants listed in Table 1-1 [70, 73] using a numerical software package MATLAB. Fig. 1-7 presents the Y_p as a function of the dimensionless factor κ ($\kappa=kr$, k is wavenumber, r is the radius of the particle) for the same wavelength plane traveling wave for four different elastic materials: stiff brass and stainless steel as well as soft polystyrene and PMMA. For relative stiff materials (brass and stainless steel), Y_p grows monotonically at small values of $ka \leq 2$ (Fig. 1-7a). Because particle is much stiffer than the background fluid medium, more momentum exchange takes place between the particle and the fluid, resulting in a stronger ARF, i.e. larger ARF function Y_p. The stiffness of a material is typically characterized by its acoustic impedance Z_c

$$Z_c = \rho_c v_c \tag{1.45}$$

where ρ_c and v_c are the density and compressional (longitudinal) sound velocity of the material, respectively.

Material	ρ (kg/m^3)	c_1 (m/s)	c_2 (m/s)	Young's modulus (GPa)	Poisson ratio (ξ)
Brass	8100	3830	2050	88.5	0.3
Stainless steel	7900	5240	2978	176.7	0.26

Polystyrene	1050	2350	1120	3.6	0.35
PMMA	1190	2270	950	3.0	0.39
Water	1000	1500	0	-	-

Table 1-1. Physical constants of elastic materials used in the ARF function calculation

Conversely, when particle becomes softer or more flexible (polystyrene and PMMA), the Y_p presents a repeating pattern of closely spaced sharp minima and maxima (Fig. 1-7b) corresponding to eigenfrequency (resonance) in each vibrational normal modes of the particle [68]. This distinct resonant behavior was not observed in King's neither theoretical calculations nor experimental measurements because he did not take into account the elasticity of the spheres he used [66]. The resonance frequency for the elastic material is essentially a spheroidal vibration mode where radial and tangential displacements occur [68]. As shown by Fig. 1-7b, the resonance frequency varies with the elasticity of particle, as indicated by the black arrows in Fig.4. The location of the resonance frequency is normally proportional to the Young's modulus E and inversely proportional to Poisson ratio v, which can be mathematically estimated as follows [74, 75]

$$\omega_{fundamental} \propto \sqrt{\frac{E}{(1+\upsilon)}} \tag{1. 46}$$

From this relationship, the fundamental frequency ratio of brass to stainless steel is approximately 0.7, while the ratio of polystyrene to PMMA is about 1.11. These estimated values are in excellent agreement with the numerical obtained ones, i.e., 0.69 and 1.12, indicated by the arrows in Fig. 1-7b.

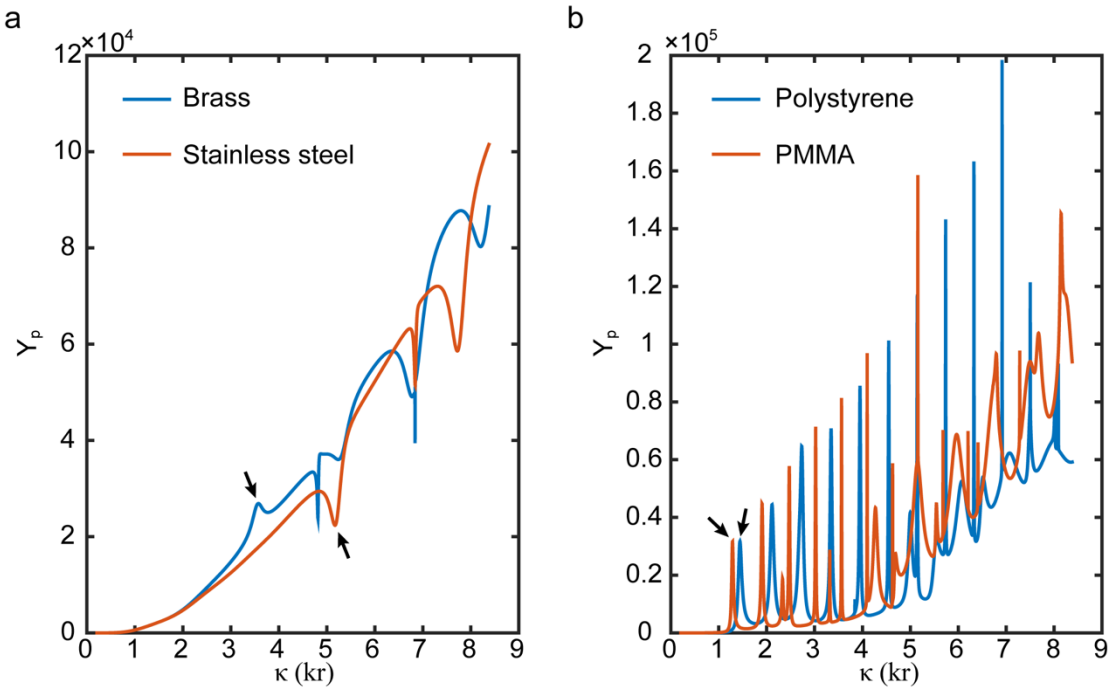

Figure 1-7. ARF functions Y_p for (a) the stiff (brass and stainless steel) (b) flexible (polystyrene and PMMA) particles in a plane traveling acoustic wave.

Unlike a unidirectional propelling ARF in a traveling acoustic wave, the direction of the ARF for a standing acoustic wave acting on the particle is no longer unvaried, but rather dependent on the particle's location with respect to the pressure antinodes or nodes of the standing wave. The ARF for the standing wave is directed from the pressure anti-nodes towards the pressure nodes. For particles that are placed in between a pressure node and anti-node with the pressure node locating on the left side, they experience a leftward ARF, hence the Y_{st} are expected to take negative values ($\kappa<2$ in Fig. 1-8a). As the wavelength of the standing wave decreases, the locations of its pressure nodes and anti-nodes shift correspondingly. When the pressure node shifts to

the right side of the particles, they experience a rightward ARF; the Y_{st} are expected to take positive values (κ>2 in Fig. 1-8a). In contrast, for more compressible and pliant particles, the direction of ARF changes abruptly at particular acoustic wavelengths with sharp peak-dip pairs over the same range of κ, 1-3 (Fig. 1-8b). These wavelengths are associated with the inherent vibrational normal mode of the particle, thus similar peak-dip pairing patterns are observed in both the traveling and standing wave scenarios. Furthermore, the excitation of these normal modes essentially promote the interactions between the particle and the standing wave, leading to more acoustic momentum exchange and thereby stronger ARF. Compared to relatively stiff particles (brass and stainless steel), soft particles (polystyrene or PMMA) experience about three times stronger ARF (Fig. 1-8).

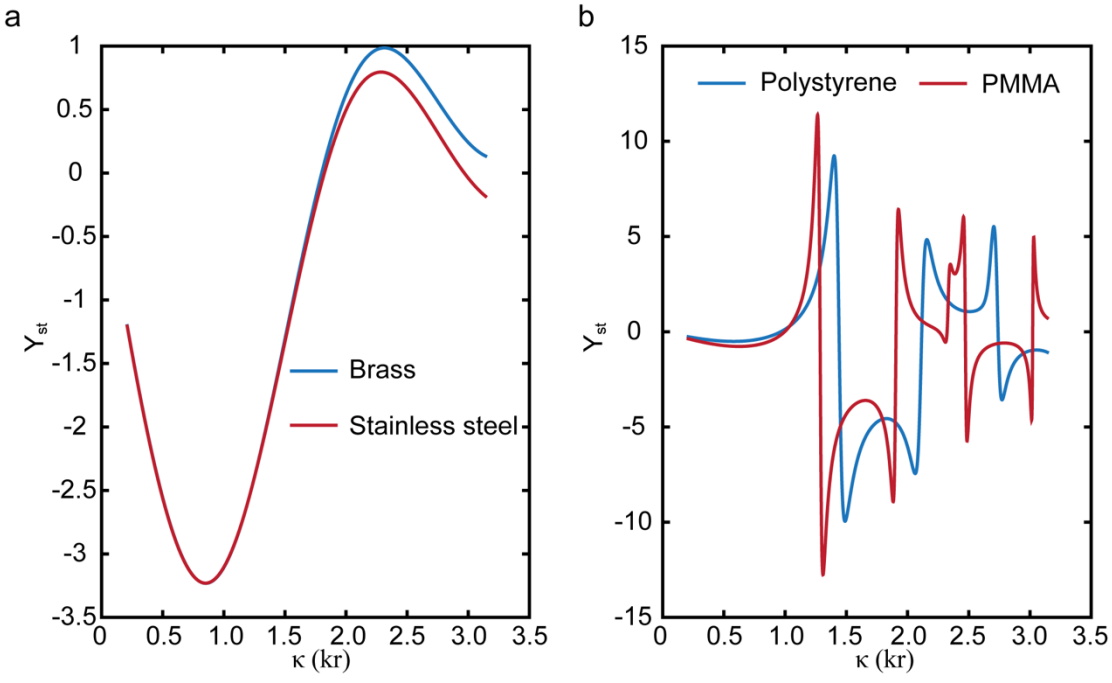

Figure 1-8. ARF functions Y_p for (a) the stiff (brass and stainless steel) (b) flexible (polystyrene and PMMA) particles in a plane standing acoustic wave.

1.6.4 Finite Element Modeling

Finite element methods have the advantage of calculating the acoustic radiation force (ARF) on arbitrarily shaped elastic and fluid particles in both one-dimensional traveling and standing acoustic waves [73, 74]. This modeling approach has been based on the foundational work of King [66] and Yosioka and Kawasima [68] on small particles. However, their theory on ARF is not restricted to small particles. Instead, this numerical approach allows us to analyze the behavior of both compressible and elastic particles of any size in an inviscid fluid. To compute the ARF on an arbitrary shaped particles, a relationship that approximates a time-averaged ARF with first-order quantities needs to be established [76]. To achieve this, a perturbation theory is applied to obtain the second-order non-zero terms from first-order ones. In addition to the stationary part p_0, the acoustic pressure field p is assumed to contain tiny perturbations in the form of first order p_1, and second order p_2 harmonic and time-dependent expansions. These small perturbations expand the density ρ and velocity v fields in the fluid environment as follows [76]

$$p = p_0 + p_1 + p_2 = p_0 + \left(\frac{\partial p}{\partial \rho}\right)^2 \rho_1 + p_2 = p_0 + c_0^2 \rho_1 + p_2 \tag{1. 47}$$

$$\rho = \rho_0 + \rho_1 + \rho_2 \tag{1. 48}$$

$$\boldsymbol{v} = 0 + \boldsymbol{v}_1 + \boldsymbol{v}_2 \tag{1. 49}$$

where c_0 is identified with the adiabatic speed of sound in the fluid; p_1, ρ_1, and $\boldsymbol{v}_1$ the first order fields; p_2, ρ_2, and $\boldsymbol{v}_2$ the second order fields. The first order pressure field is typically on a faster time scale than that of hydrodynamics at megahertz frequencies [77]. Therefore, this approximately five orders of magnitude difference in time scale greatly simplifies the solution for acoustic fields, allowing the hydrodynamic components to be kept fixed in time. By applying these three fields into the governing equations based on conservation of mass and momentum, and hydrodynamic Navier-Stokes relations in the fluid [76]

$$p = p(\rho) \tag{1. 50}$$

$$\partial_t \rho = -\nabla \cdot (\rho \boldsymbol{v}) \tag{1. 51}$$

$$\rho \partial_t \boldsymbol{v} = -\nabla p - \rho(\boldsymbol{v} \cdot \nabla)\boldsymbol{v} + \eta \nabla^2 \boldsymbol{v} + \beta \eta \nabla(\nabla \cdot \boldsymbol{v}) \tag{1. 52}$$

where β and η are the dynamic viscosity ratio and viscosity of the fluid, respectively, the pressure, density, and velocity fields can be obtained

$$p_2 = c_0^2 \rho_2 + \frac{1}{2}\left(\partial_\rho c_0^2\right)\rho_1^2 \tag{1. 53}$$

$$\partial_t \rho_2 = -\nabla \cdot \boldsymbol{v}_2 - \nabla \cdot (\rho_1 \boldsymbol{v}_1) \tag{1. 54}$$

$$\partial_t \rho_2 = -\nabla \cdot \boldsymbol{v}_2 - \nabla \cdot (\rho_1 \boldsymbol{v}_1) \tag{1. 55}$$

where <> denotes a time average product. By assuming a harmonic time dependence on the first order fields, the time average of equations (1.53-1.55) become

$$\rho_0 \nabla \cdot \langle \boldsymbol{v}_2 \rangle = -\nabla \cdot \langle \rho_1 \boldsymbol{v}_1 \rangle \tag{1. 56}$$

$$\eta \nabla^2 \langle \boldsymbol{v}_2 \rangle + \beta \eta \nabla(\nabla \cdot \langle \boldsymbol{v}_2 \rangle) - \nabla \langle p_2 \rangle = \langle \rho_1 \partial_t \boldsymbol{v}_1 \rangle + \rho_0 \langle (\boldsymbol{v}_1 \cdot \nabla)\boldsymbol{v}_1 \rangle \tag{1. 57}$$

where $\langle p_2 \rangle$ and $\langle \boldsymbol{v}_2 \rangle$ represent ARF and acoustic streaming, respectively. Physically, the energy and momentum absorption from acoustic wave lead to bulk fluid flow, while a pulling (pushing) force occurs for the cases where the majority of incident acoustic energy is scattered by the particle that is suspended in solution in the forward (backward) direction. The time-averaged ARF acting on the particle suspended in the fluid medium can be obtained by integrating the normal component of the total acoustic pressure over the surface of the particle [73, 75]

$$\vec{F}_{ARF} = -\langle \iint_{S} p_2 \boldsymbol{n} d\boldsymbol{S} \rangle \tag{1. 58}$$

where $\boldsymbol{S}$ is the external surface the particle. The particle considered here is assumed to be freely moving in the fluid in response to the altering velocity field by the pressure perturbation. Then the above equation becomes

$$\vec{F}_{ARF} = -\langle \iint_{S(t)} p_2 \boldsymbol{n} d\boldsymbol{S} \rangle \tag{1. 59}$$

For the ease of calculation, Yosioka and Kawasima [68] utilized Reynolds' transport theorem and proposed an approximation method by simply adding a correction term in addition to integrating p_2 over equilibrium position of the particle

$$\boldsymbol{F}_{ARF} = -\langle \iint_{S_0} p_2 \boldsymbol{n} d\boldsymbol{S} \rangle - \langle \iint_{S_0} \rho_0 (\boldsymbol{n} \cdot \boldsymbol{v}_1) \boldsymbol{v}_1 d\boldsymbol{S} \rangle \tag{1. 60}$$

where the first term represents the total pressure acting on the particle and the second term is the particle motion in response to the fluid movements. This term can be treated as a momentum flux through a fixed particle surface [73]. It should be noted that

equation (1.60) holds only when the viscous and thermal effects are minimal. The second order flux in the first term of equation (1.60) can be expressed as

$$p_2 = \frac{1}{2\rho_0 c_0^2}\langle p_1\rangle^2 - \frac{\rho_0}{2}\langle v_1\rangle^2 \tag{1. 61}$$

Therefore, the ARF on the particle can be finally expressed as

$$\boldsymbol{F}_{ARF} = -\left(\langle \iint_{S_0}\left[\frac{1}{2\rho_0 c_0^2}\langle p_1\rangle^2 - \frac{\rho_0}{2}\langle v_1\rangle^2\right]\boldsymbol{n}d\boldsymbol{S}\rangle + \langle \iint_{S_0}\rho_0\left(\boldsymbol{n}\cdot\boldsymbol{v}_1\right)\boldsymbol{v}_1 d\boldsymbol{S}\rangle\right) \tag{1. 62}$$

where the squared term p_1^2 and v_1^2 can be decomposed into the first order incident and scattered pressure fields, as expressed below

$$p_1^2 = p_{1i}^2 + 2p_{1i}p_{1s} + p_{1s}^2 \tag{1. 63}$$

$$v_1^2 = v_{1i}^2 + 2v_{1i}v_{1s} + v_{1s}^2 \tag{1. 64}$$

where p_{1i} and p_{1s} represent the incident and scattered first order pressure fields, v_{1i} and v_{1s} the incident and scattered first order velocity fields. Note, the squared terms p_{1s}^2 and v_{1s}^2 can be neglected when the particle size is much smaller than the acoustic wavelength. Thus, only the mixed products are left behind in the equations (1.63) and (1.64), i.e. $p_{1i}p_{1s}$ and $v_{1i}v_{1s}$. Under these circumstances, long wavelength approximation, the ARF can be approximated based on Gor'kov's theory [43]. To generalize the numerical calculation of ARF for any arbitrary particle sizes, the square pressure and velocity terms and their mixed products in equations (1.63) and (1.64) must be included in the equation (1.62).

To construct the finite element model, we used COMSOL Multiphysics®. Table 1-2 lists the acoustic wavelength, elastic constants of particle, fluid density and sound

velocity, position of particle, and incident acoustic pressure amplitude. The particle diameter was parameterized to obtain the ARF as a function of the product of wave number and particle radius. For ease of calculations, a 2D axisymmetric geometric model was used, with a rectangular fluidic domain with height of four acoustic wavelength and width of two acoustic wavelength (Fig. 1-9). This model incorporates the effect of the ARF imposed by a traveling or a standing acoustic wave or a superposition of both. To investigate the effect, the top and bottom boundaries of the 2D box were set to act as the wave sources. In order to minimize the wave reflections from the side boundary, a non-reflection boundary condition is applied. This was done by establishing a radiation or matched acoustic impedance boundary condition to the right end side. Since this model is 2D axisymmetric, the waves used in this model were cylindrical waves. The amplitudes of the leftward and rightward propagating waves were set to be R_1 and R_2, respectively. To generate a pure traveling acoustic wave, one of them was set to be zero while the other 1. By setting both of them to be 1, a pure standing acoustic wave is generated. For amplitudes with any values between 0 and 1, a quasi-standing acoustic wave would be established in the simulation domain. The fluid and particle domains were meshed with free triangular elements with extremely fine size. The meshing was much more refined around the interface between particle and fluid to ensure an accurate calculation of the physical fields originating from the scattered acoustic waves. To make the numerical calculation more accurate, a surface was placed outside the particle for surface integral calculation. This approach is valid due to the conversation of flux, meaning that the force computation using the equation

(1.62) is independent of the integration surface. Therefore, in our numerical model, a hemi-circle that is external to the particle was added for surface integral. The particle was placed one sixth of the acoustic wavelength away from the center O in Fig. 1-9. In the simulation, the particle diameter was scanned from 0.03λ to λ.

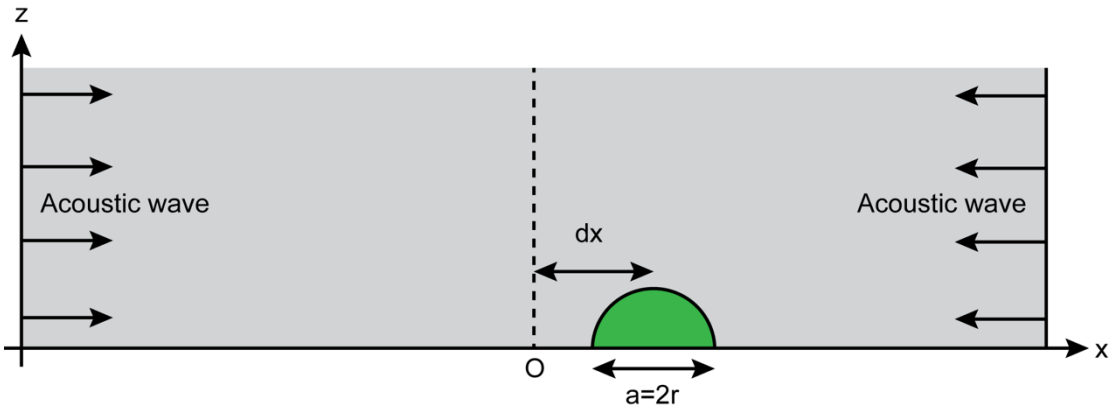

Figure 1-9. Schematic of the 2D axisymmetric finite element model.

Parameters	Symbol	Value	Unit
Fluid domain (Water)			
Domain width	4λ	500	μm
Domain height	4λ	250	μm
Wavelength	λ	125	μm
Density	ρ_f	1000	kg/m^3
Sound speed	c_f	1500	m/s
Frequency	f	12	MHz
Wavenumber	k	5×10^4	m^{-1}

Left wave amplitude	R_1	1	-
Right wave amplitude	R_2	1	-
Pressure amplitude	p_0	10^6	Pa
Solid domain (Particle)			
Particle diameter	a	variable	-
Particle radius	r	variable	-
Elastic material I (Stainless steel/Polystyrene)			
Density	ρ_p	7900/1050	kg/m^3
Acoustic compressional velocity	$c_{compress}$	5240/2350	m/s
Acoustic shear velocity	c_{shear}	2978/1120	m/s
Modulus of elasticity	E_p	176.7/3.6	GPa
Poisson ratio	ξ_p	0.26/0.35	-

Table 1-2. Basic parameters of the finite element model.

Fig. 1-10 shows the calculated ARF acting on an elastic sphere of two different materials, stainless steel and polystyrene due to a traveling wave. Here, a normalized particle size (*kr*) varying from 0 to 3.5 is assumed. The ARFs based on Hasegawa's analytical equations are added into the plot for comparison purposes (blue curves). In this plot, the ARF acting on the sphere is positive for both materials over a very wide range of particle size, suggesting that the ARF acts as a propelling force that pushes the particle away from the acoustic source. Moreover, the overall shape of the ARF curve

for polystyrene is noticeably different from that for stainless steel. A repeating pattern of maxima and minima is observed in the ARF for polystyrene, whereas the ARF for stainless steel increases monotonically. This marked difference originates from the resonance frequencies of an elastic sphere [68].

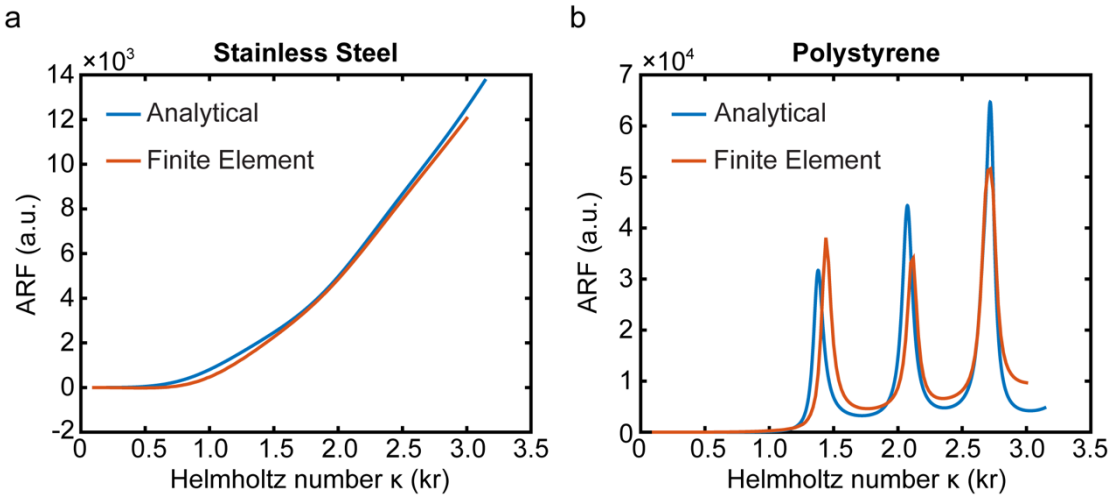

Figure 1-10. ARF acting on (a) stainless steel and (b) polystyrene spheres in a traveling acoustic wave. Blue and red solid lines represent the results obtained using the analytical and finite element methods, respectively.

When a second counter-propagating acoustic wave is incorporated into the simulation domain, a standing acoustic wave is established with its pressure anti-node located right at the center O. Fig. 1-11 shows the calculated ARFs acting on an elastic sphere of two different materials, stainless steel and polystyrene due to a standing wave. Here, a normalized particle size (*kr*) from 0 to 3.5 is assumed. It For stainless steel and polystyrene spheres, the ARF decreases gradually with size and then rapidly increases as the particle size is increased further. The negative force means that the sphere is pushed towards its neighboring pressure anti-node while a positive sign indicates that

the sphere will be moved towards the nearest node. For the polystyrene sphere, a repeating pattern of minima and maxima points are observed, which are associated with the resonance frequencies of the elastic sphere [68]. Furthermore, the finite element simulations (red curve) are in excellent agreement with the Hasegawa's analytical ones (blue curve). The observed discrepancy between them is possibly due to the non-negligible acoustic reflections from the channel wall that distort the local pressure field.

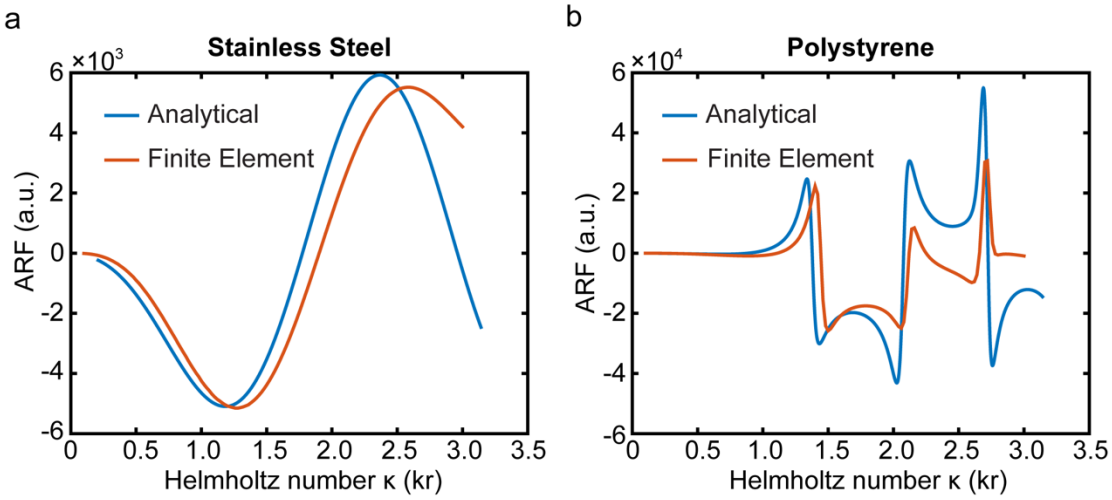

Figure 1-11. ARF acting on (a) stainless steel and (b) polystyrene spheres in a standing acoustic wave. Blue and red solid lines represent the results obtained using the analytical and finite element methods, respectively.

To further investigate the nature of the ARF imposed by a traveling and standing waves (Fig. 1-12a,b), the simulated particle of a fixed size is sequentially translated with reference to the field. Fig. 1-12c shows the variation of the resulting ARF acting on a stainless steel particle imposed by a traveling and standing waves, respectively. Fig. 1-12d shows the variations of the resulting ARF acting on a polystyrene particle imposed

by a traveling and standing waves, respectively. It is observed that the force acting on both the stainless steel and polystyrene particles imposed by the traveling wave remains unvaried for all *x*-positions. This numerical result is consistent with the above theoretical analysis, i.e., the force acting on the particle imposed by a traveling wave is a unidirectional and is independent from the particle's location relative to the field. In comparison, the force acting on both the stainless steel and polystyrene particles imposed by the standing wave has a strong dependence on the particle's position relative to the field. The minima and maxima points indicate the positions of the anti-nodes of the standing wave, while the zero-values of the force indicates the positions of the nodes. This is because both particles have a positive acoustic contrast factor (ACF) Φ, which is defined as

$$\Phi = \frac{5\rho_p - 2\rho_f}{2\rho_p - \rho_f} - \frac{\beta_p}{\beta_f} \tag{1. 65}$$

where ρ_p and ρ_f are the densities of the particle and fluid medium, respectively; β_p and β_f the compressibilities of the particle and fluid medium, respectively. When ACF is positive, in the case of the polystyrene or stainless steel particle, the gradient ARF pushes the particles toward the pressure node. When it becomes negative, in the case of an air bubble in the water, the bubble will be pushed towards the pressure anti-node.

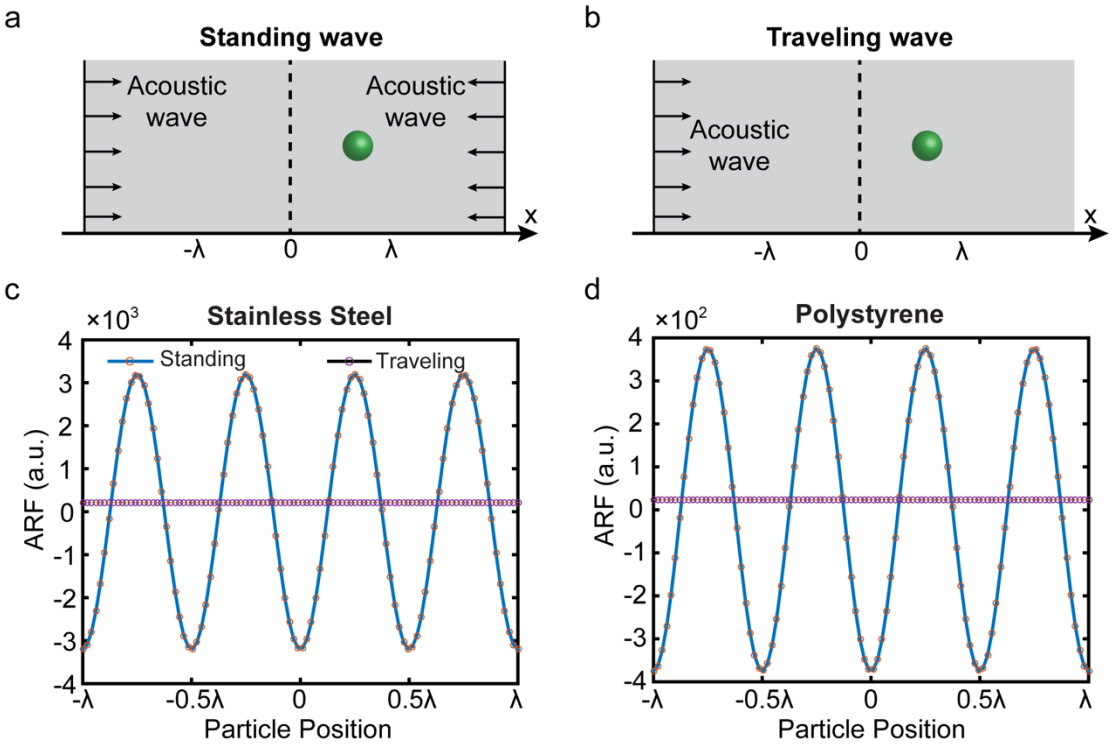

Figure 1-12. Finite element model calculated ARF imposed by (a) a standing wave and (c) a traveling wave in the *x*-direction against *x*-position of the (b) stainless steel (d) polystyrene particle from the center of the fluid domain.

As shown by Fig. 1-10 and 1-11, the scattering and gradient ARFs strongly depend on the particle size. To understand the relative importance of the scattering and gradient forces acting on the same particle, ARFs acting on a polystyrene particle due to a traveling and standing waves are compared (Fig. 1-13a,b). For particle that is much smaller than the acoustic wavelength ($a<<\lambda$), the gradient ARF due to a pure standing acoustic wave is one to two orders of magnitude greater than the scattering ARF due to a pure traveling acoustic wave (Fig. 1-13c). As the particle size increases and becomes comparable to the acoustic wavelength ($a\sim\lambda$), the scattering ARF start to become

several orders of magnitude stronger than the gradient ARF when the elastic resonance of the particle is excited (Fig. 1-13d).

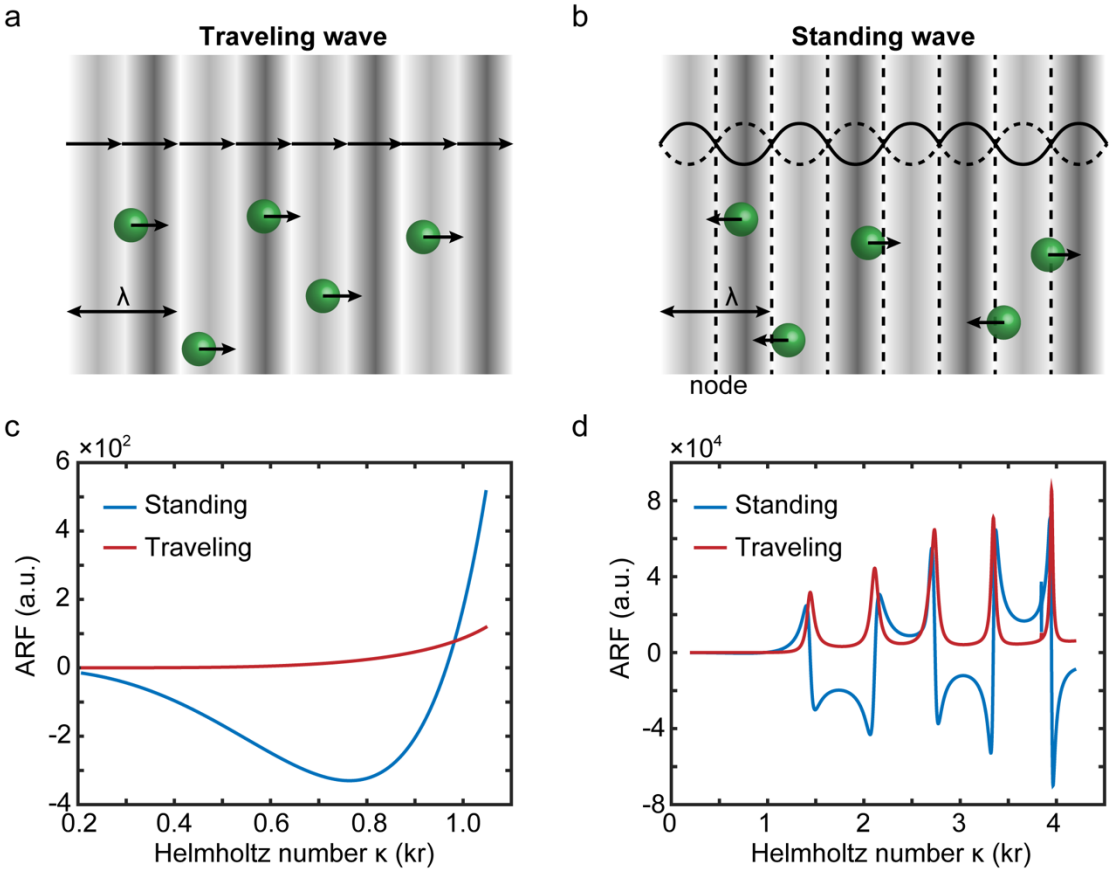

Figure 1-13. Analytically calculated ARF as a function of the size of a polystyrene particles in a (a) traveling and (b) standing acoustic wave fields. Dashed lines represent the pressure nodes; The scattering and gradient ARFs are compared for the (c) low $\kappa<1$ and (d) high $\kappa>1$ Helmholtz numbers.

1.6.5 Plane Quasi-Standing Acoustic Wave

The ARF of an elastic sphere for a plane quasi-standing wave that results from the interference of two counterpropagating plane traveling waves of same wavelength but

of different amplitudes can be analytically evaluated using equations (1.39) and (1.44), which can be expressed below [70],

$$Y_{qs} = \left(1 - \frac{B^2}{A^2}\right) Y_p + \frac{B}{A} Y_{st} \sin 2kh \tag{1. 66}$$

where A and B are the complex amplitudes of the velocity potentials of the two counter-propagating plane traveling waves, respectively. Here, we assume $A>B$. Then the corresponding ARF becomes

$$F_{qs} = F_p \left[\left(1 - \frac{B^2}{A^2}\right) + \frac{B}{A} \frac{Y_{st}}{Y_p} \sin 2kh \right] = \pi a^2 \bar{E} Y_{qs} \tag{1. 67}$$

The magnitude of F_{qs} is a function of the spatial position of the sphere with respect to the antinode of the velocity potential field.

In addition to using two separate acoustic sources to generate counter-propagating plane traveling waves, plane quasi-standing waves can also be produced in a cavity-resonator like system using just a single acoustic source. As schematically shown by Fig. 1-14a, an acoustic cavity filled with medium 1 of acoustic impedance Z_1 is constructed by two acoustic "mirrors", i.e., one is the acoustic source (usually an extremely stiff solid), the other a medium of different acoustic impedance (Z_2). The acoustic source on the left side of the cavity generates a right-propagating plane traveling wave in medium 1 (outlined in dark grey) towards the medium 2 (outlined in light grey). Due to the acoustic impedance mismatch between the two media, partial wave reflection and transmission take place right at this interface. The incident,

reflected and transmitted acoustic waves in the form of oscillating pressure can be represented as

$$p_i = Ae^{j(\omega t - k_1 x)} \tag{1. 68}$$

$$p_r = AR_p e^{j(\omega t + k_1 x)} \tag{1. 69}$$

$$p_t = AT_p e^{j(\omega t - k_2 x)} \tag{1. 70}$$

where A represents the incident wave amplitude, R_p reflection coefficient, T_p transmission coefficient, k_1 the wave vector of incident and reflected pressure waves, k_2 the wave vector of transmitted pressure waves, ω the angular frequency of all waves, t the time. At an equilibrium state, the pressure and velocity across the interface are continuous. Based on the definition of acoustic impedance of an acoustic wave which is the ratio of pressure and velocity, the boundary conditions can be written as [53]

$$p_i - p_r = p_t \tag{1. 71}$$

$$\frac{p_i - p_r}{Z_1} = \frac{p_t}{Z_2} \tag{1. 72}$$

where Z_1 and Z_2 represent acoustic impedances of medium 1 and 2, respectively. Reflection and transmission coefficients can be then obtained by solving the above two equations

$$R_p = \frac{Z_2 - Z_1}{Z_1 + Z_2} \tag{1. 73}$$

$$T_p = \frac{2Z_2}{Z_1 + Z_2} \tag{1. 74}$$

When there is a large acoustic impedance mismatch, acoustic wave is fully reflected. The phase change for the pressure at the interface depends on the acoustic impedance ratio between these two media. In the case of a free boundary, for example, acoustic waves propagate from water to air ($Z_1 >> Z_2$), then $R_p \approx -1$ and $T_p \approx 0$. Hence, a nearly perfect reflection for the incident acoustic wave occurs at the interface with a phase change of π. As shown by Fig. 1-14b, the totally reflected acoustic wave interfere with the counter-propagating incident wave, creating a standing wave pattern with five nodes formed in the acoustic cavity. Due to the phase jump at the interface, there is one antinode located at the center of the cavity. As opposed to a free boundary, when the medium 2 becomes an extremely stiff compared to medium 1 ($Z_1 << Z_2$), then $R_p \approx 1$ and $T_p \approx 2$. In this scenario, there is no phase difference between the incident and the totally reflected acoustic waves. Hence, the node locations of the interfered standing wave is expected to be different than that in the free boundary scenario. As shown by Fig. 1-14c, only three nodes exist, with two of them located at the boundaries of the cavity and one at the center of the cavity. Nodes are essentially shifted by a quarter wavelength with respect to those in the free boundary scenario (Fig. 1-14b).

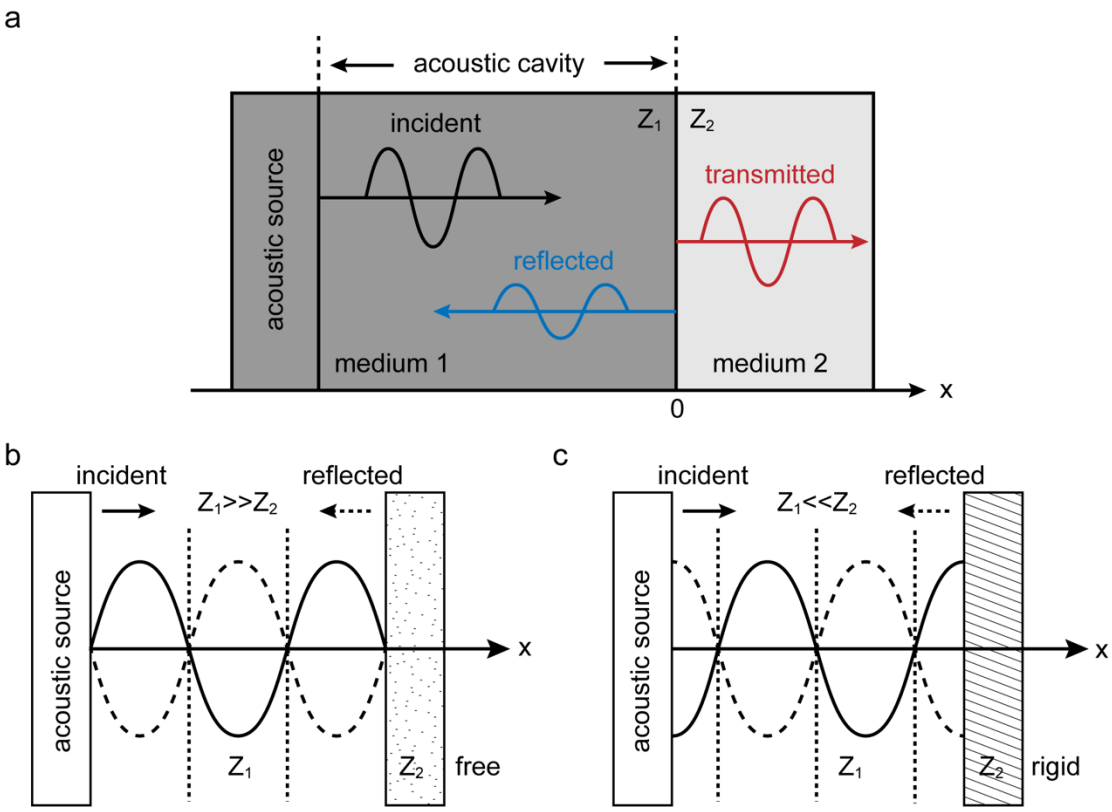

Figure 1-14. Quasi-standing wave generation in an acoustic cavity formed by two acoustic "mirrors" of different acoustic impedances. When the acoustic impedance of the cavity medium (medium 1) is much larger (smaller) than that of the "mirror" (medium 2), the incident acoustic wave experiences a total reflection with a π (zero) phase change. The totally reflected acoustic wave will constructively interfere with the incident wave forming a standing acoustic wave, with (b) five and (c) three nodes distributed within the cavity.

When the acoustic impedance mismatch is not significant, the superposition of the partially reflected and incident traveling acoustic waves will create a quasi-standing acoustic wave field in the cavity. The acoustic field in the cavity can be formulated as

$$p = p_i + p_r = Ae^{j(\omega t - k_1 x)} + AR_p e^{j(\omega t + k_1 x)} \tag{1.75}$$

$$p = Ae^{j\omega t}\left[\left(1 + R_p\right)\cos(k_1 x) + j\left(R_p - 1\right)\sin(k_1 x)\right] \tag{1.76}$$

This quasi-standing wave field will exert a radiation force (ARF) on elastic particles:

$$F_{qs} = F_p\left[\left(1 - R_p^2\right) + R_p F_{st}\right] \tag{1.77}$$

where F_p and F_{st} are the scattering and gradient ARF for traveling and standing waves, respectively, F_{qs} the ARF for quasi-standing waves, R_p the acoustic reflection coefficient defined in equation (1.73).

Fig. 1-15 and Fig. 1-16 compare two different scenarios corresponding to different sign phases gained from reflection at the medium 1-2 interface. The analytical results for the ARF acting on a polystyrene spherical particle over a range of particle diameters (3-24 μm) is presented. The wavelength of the incident traveling acoustic wave used in the calculations is 121 μm. The particle position is at a distance h=1/12λ from the center of the acoustic cavity. To examine the effect of acoustic impedance ratio of medium 1 to medium 2 on the magnitude and direction of the ARF for a certain particle size, a broad range of acoustic impedance ratios is selected. In the first scenario when the acoustic impedance of the medium 1 is larger than that of the medium 2 ($Z_1 > Z_2$), the wave reflection coefficient is always negative based on the equation (1.73), resulting in a π change in the reflected acoustic wave relative to the incident one. As shown in Fig. 1-15b, the net ARF acting on the particle increases from zero to approximately 5 (defined in arbitrary units) with particle diameter when there is no acoustic impedance mismatch between two media (blue solid curve, $R_p = 0$). The positive value of the ARF

indicates that it is in the same direction as the incident traveling acoustic wave. In this scenario, the net ARF is essentially a scattering ARF resulted from a pure traveling acoustic wave. However, in the case of non-zero acoustic impedance mismatch, a portion of the incident traveling acoustic wave is reflected back into the cavity, causing an imbalance that gives rise to a mixed wave field consisting of a standing wave (amplitude proportional to R_p) and traveling wave (amplitude proportional to 1- R_p) component in the cavity. The traveling wave component pushes the particle in the propagation direction of the incident wave. On the other hand, the standing wave component traps the particle at its node that is at a quarter wavelength distance away from the cavity center due to the phase jump due to the wave reflection at the interface separating the two media (Fig. 1-14a). Hence, the standing wave pushes the particle leftward towards the acoustic source. It should be noted that there are two other anti-nodes in addition to the one at the cavity center in this standing wave (Fig. 1-14b). Therefore, the net force acting on the particle is a competition of the scattering ARF originating from the traveling wave with the gradient ARF originating from the standing wave (as shown by the inset in Fig. 1-15a). It should be noted that the linear superposition of the acoustic pressure fields is not equal to superposition of acoustic radiation forces as ARF is a non-linear effect and arises from second order terms [78, 79]. As shown in Fig. 1-13c, for a particle that is much smaller than the acoustic wavelength ($a<<\lambda$), the gradient ARF in a pure standing acoustic wave (or $|R_p|=100\%$) is one to two orders of magnitude greater than the scattering ARF in a pure traveling acoustic wave (or $|R_p|=0$). By adjusting the reflection coefficient R_p, i.e., the measure

of the relative strength of the traveling and standing wave components, the dominant role of the acoustic field can be tuned from the traveling wave to the standing wave, or vice versa. Fig. 1-15b shows the analytically calculated net ARF as a function of the particle size a, for a range of reflection coefficients R_p. For an extremely low reflection (R_p = -10%), the net ARF slowly changes its sign (direction) from a negative value to a positive value as the particle size increases. This indicates the dominant component of the acoustic field transitions from the standing wave to the traveling wave and the crossover particle size value is around 18 μm. However, at larger absolute reflection coefficient values ($|Rp| \geq 3\%$), the sign of the ARF value over the entire range of particle sizes is unvaried, suggesting that the dominant component is always the standing wave. We find an excellent agreement in between the analytical calculations and the FEM simulations, as shown by Fig. 1-15c.

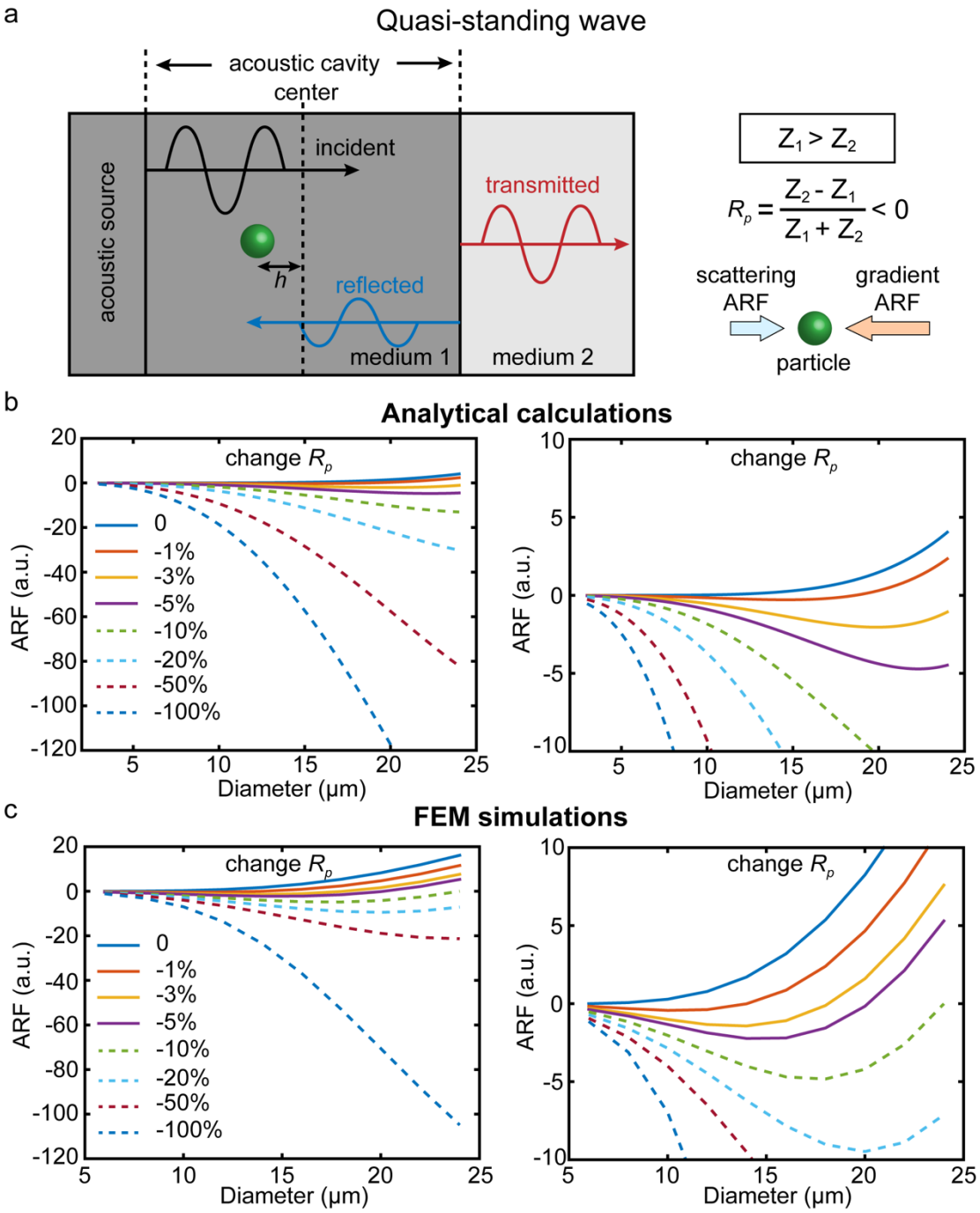

Figure 1-15. The acoustic impedance of the medium 1 is relatively large with respect to the medium 2, $Z_1 > Z_2$. (a) Acoustic radiation force (ARF) on a polystyrene sphere in a quasi-standing wave. The particle position is at distance h from the center of the

acoustic cavity. (b) Analytical results and (c) FEM simulations for the net ARF over a certain wavelength 121 μm as a function of the particle size *a*, for a broad range of reflection coefficients R_p.

In the second scenario, when the acoustic impedance of the medium 1 is smaller than that of the medium 2, i.e., $Z_1 < Z_2$ (Fig. 1-16a), the reflection coefficient is always positive, leading to no phase change due to the wave reflection at the interface between the two media. As demonstrated above, both a standing wave (amplitude proportional to R_p) and traveling wave (amplitude proportional to 1- R_p) component exist within the cavity. The traveling wave component still pushes the particle in the propagation direction of the incident wave. Because there is no phase difference between the incident and reflected acoustic waves, the node (antinode) locations of the created standing wave will be shifted by a quarter of acoustic wavelength λ (Fig. 1-14c). As a result, the standing wave pushes the particle in the propagation direction of the incident wave. Therefore, the net ARF acting on the particle is always positive, i.e., along the incident wave propagation direction. Fig. 1-16b shows the analytically calculated net ARF as a function of the particle size *a*, for a broad range of reflection coefficients R_p. The sign of the ARF is always positive independently from the reflection coefficient values, confirming the scattering and gradient ARFs are always in the same direction in this scenario. On the other hand, the magnitude of the net ARF is significantly large for high acoustic reflection coefficient values (R_p >20%). This is mainly due to the standing wave component, which is the dominant component of the acoustic field. Our analytical calculations are in excellent agreement with our FEM simulations (Fig. 1-

16c), demonstrating the accuracy of the analytical models used for the calculation of the ARF in a quasi-standing wave.

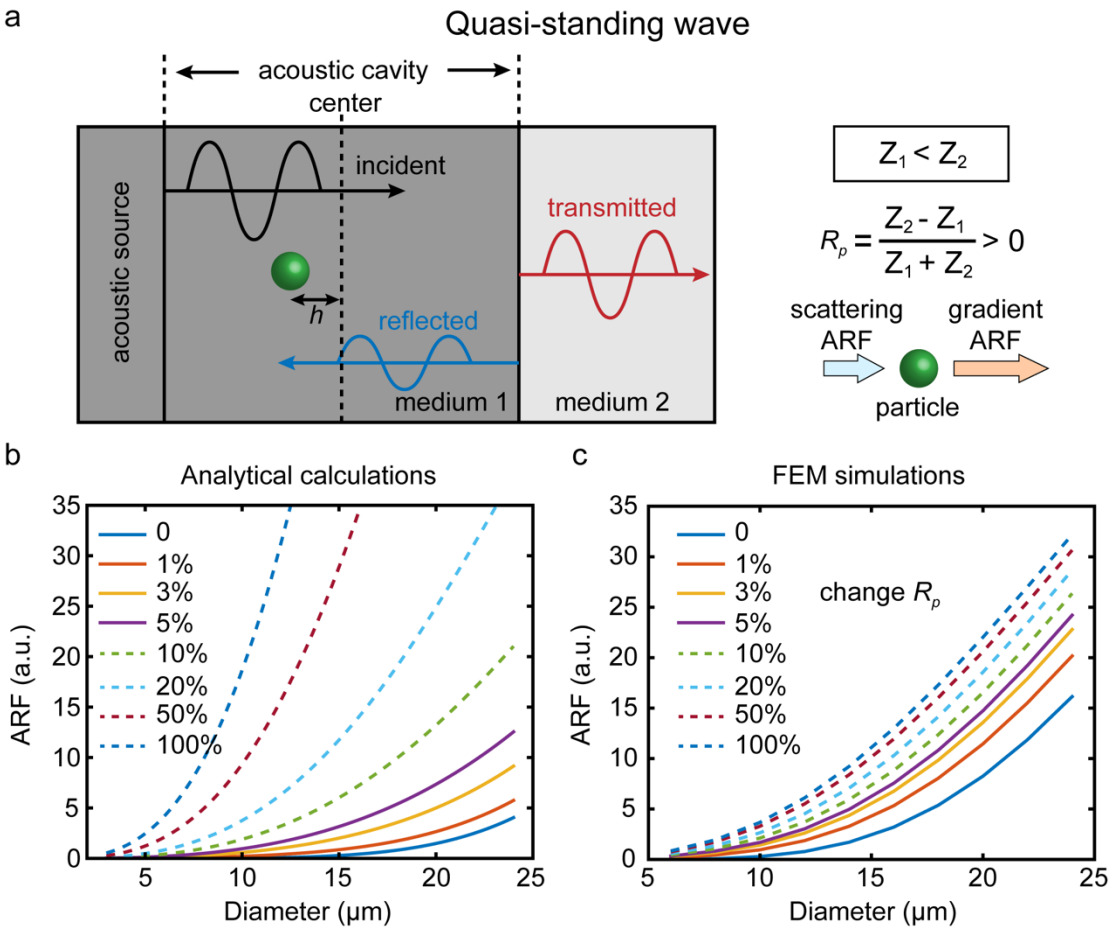

Figure 1-16. The acoustic impedance of the medium 1 is relatively large with respect to the medium 2, $Z_1<Z_2$. (a) Acoustic radiation force (ARF) on a polystyrene sphere in a quasi-standing wave. The particle position is at distance h from the center of the acoustic cavity. (b) Analytical results and (c) FEM simulations for the net ARF over a certain wavelength 121 μm as a function of the particle size a, for a broad range of reflection coefficients R_p.

1.7 Acoustic Drifting Effect

1.7.1 Working Mechanism of Acoustic Drifting Effect (ADE)

An acoustic drifting effect (ADE) chip is designed to achieve efficient immuno-affinity based isolation of micrometer size targets (e.g. rare cells). The ADE is engineered to create a drifting force acting on the particles pushing them towards the channel walls. This is summarized in Fig. 1-17a . Here, the acoustic field gradient creates an acoustic drifting zone (indicated by the region bounded by the red dashed lines), where particles that randomly introduced to the fluidic channel become ordered as they pass through it (Fig. 1-17a). By carefully engineering the spatial distribution of the acoustic field gradient, particles are drifted to the middle of the channel and towards surface of the substrate (Fig. 1-17a). In our ADE chip, a three-dimensional acoustic field is created by interfering two counterpropagating ultrasonic surface acoustic waves (SAWs) that are generated by applying a radio-frequency AC voltage across a pair of interdigitated transducers (IDTs) lithographically patterned on a piezoelectric lithium niobate ($LiNbO_3$) substrate. Due to the tight surface-bound nature of the SAWs, the two counterpropagating SAWs in the form of atomic-scale surface displacements can efficiently "leak" into the fluid that is located in between the IDTs (Fig. 1-17b) [50]. The tiny surface displacements on the order of 0.1-10 nm can strongly actuate the fluid inside the channel inducing compressional acoustic bulk waves (BAWs) with pressures on the order of MPa propagating away from the fluid-substrate interface at the Rayleigh angle $\theta_R = \sin^{-1}(C_F/C_R)$ (C_F and C_R are the sound speeds of fluid and $LiNbO_3$,

respectively) to the normal of the substrate (Fig. 1-17b) [34, 49]. The wavelength of the BAWs can be found using the Rayleigh relation, i.e., $\lambda_{BAW} = \lambda_{SAW}\sin\theta_R$ [50]. In principle, the superposition of the two BAWs propagating in opposite directions produces a pure standing BAW in the horizontal plane of the channel cross-section with a wavelength $\lambda_{BAW,hori} = \lambda_{SAW}\sin\theta_R/\sin\theta_R = \lambda_{SAW}$ and a pure upward propagating traveling BAW in the vertical plane of the channel cross-section with a wavelength $\lambda_{BAW,vert} = \lambda_{SAW}\sin\theta_R/\cos\theta_R = \lambda_{SAW}\tan\theta_R$. The interaction between the energy gradients within the standing BAW field and the wave scattered by the surrounding particles suspended in the microchannel results in a nonlinear acoustic radiation force (ARF) potential (also called Gor'kov potential) field [43]. The low Gor'kov potential field areas operates as an "acoustic well", generating a gradient ARF that attracts the particles towards the well and eventually traps them in this region (Fig. 1-17c).

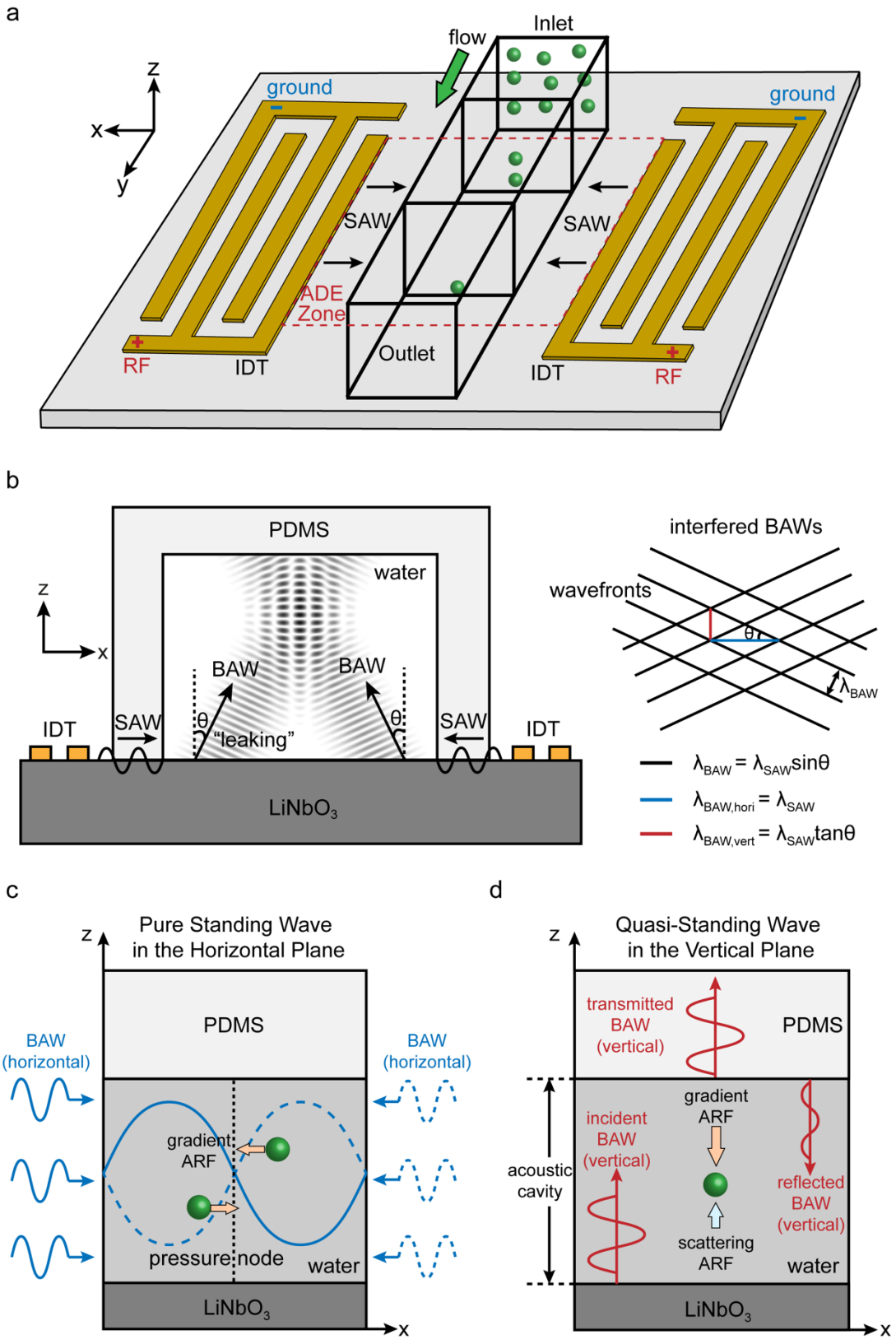
a
Inlet
flow
ground
ground
z
x
y
SAW
SAW
ADE
Zone
RF
IDT
Outlet
IDT
RF
b
PDMS
water
z
x
BAW
BAW
IDT
SAW
θ
"leaking"
θ
SAW
IDT
LiNbO3
interfered BAWs
wavefronts
θ
λBAW
λBAW = λSAWsinθ
λBAW,hori = λSAW
λBAW,vert = λSAWtanθ
c
Pure Standing Wave
in the Horizontal Plane
z
PDMS
BAW
(horizontal)
BAW
(horizontal)
gradient
ARF
pressure node
water
LiNbO3
x
d
Quasi-Standing Wave
in the Vertical Plane
z
transmitted
BAW
(vertical)
PDMS
gradient
ARF
incident
BAW
(vertical)
acoustic
cavity
reflected
BAW
(vertical)
scattering
ARF
water
LiNbO3
x

Figure 1-17. (a) Schematic of the acoustic drifting effect (ADE) chip for acoustic field flow fractionation (FFF). (b) Two counter-propagating SAWs from the excited IDTs couple energy into the fluid and propagate in the form of BAWs. The ADE is generated through an interference of these two counter-propagating BAWs at a Rayleigh angle in the fluid, which establishes a pure standing BAW in the horizontal plane (c), and a quasi-standing BAW in the vertical plane (d).

When there is an acoustic impedance mismatch between the channel ceiling (PDMS) and the fluidic medium, the upward propagating traveling BAW will experience a partial reflection (R). In this case, an acoustic cavity resonator is formed between the bottom substrate and the channel ceiling (Fig. 1-17d). After multiple reflections between the perfectly reflective (piezoelectric substrate) and partially reflective (channel ceiling) "acoustic mirrors", a standing BAW in the vertical plane of the fluid is created. This vertical standing BAW with an amplitude associated with the acoustic reflection coefficient R is superimposed on the non-reflected portion (1-R) of the traveling BAW, yielding a quasi-standing acoustic wave in the vertical plane of the fluid (Fig. 1-17d). Suspended particles in this quasi-standing wave field are subject to two different types of acoustic radiation forces (ARFs): scattering ARF originating from the non-reflected vertical traveling BAW component, gradient ARF imposed by the vertical standing BAW component. When the fluid has a relatively high acoustic impedance with respect to the channel roof, a π-phase change occurs as a result of acoustic wave reflection. This sudden phase jump causes low Gor'kov potential areas to be formed near the "acoustic mirrors", giving rise to a gradient ARF that points

towards them. For particles that are located at a close vicinity of the substrate, he upward scattering ARF and downward gradient ARF are in competition, as illustrated by Fig. 1-17d. As shown in Fig. 1-13c, for a particle that is much smaller than the acoustic wavelength ($a<<\lambda$), the gradient ARF in a pure standing acoustic wave (corresponding to $|R|=100\%$) is about two orders of magnitude greater than the scattering ARF in a pure traveling acoustic wave (or $|R|=0$). By carefully choosing the reflection coefficient R based on the selections of the materials for channel ceiling, the dominant role of the force can be tuned from the scattering ARF to the gradient ARF, or vice versa. In our ADE chip, PDMS material is commonly used to create microfluidic channels. When the channel is filled with water, the amount of the acoustic reflection from the channel ceiling is approximately -3%. Even for low reflection, the gradient ARF created by the interference of counter propagating BAWs dominates over the scattering ARF in a broad range of particle diameters from 0 to 20 μm (Fig. 1-15b-c). Therefore, the net ARF acting on the particles will push them towards the substrate.

1.7.2 Three-Dimensional Acoustic Radiation Force (ARF) Fields

To create a three-dimensional acoustic field orthogonal to an axial fluid flow that enables particle/cell drifting towards pre-determined locations, the ADE mechanism by which the horizontal standing BAW and vertical quasi-standing BAW manipulate cell-like particles and cells within such a microchannel must be understood. A finite element method (FEM) model was developed to investigate the Gor'kov potential field in a

lateral plane (*xz* plane) and to analyze the acoustic radiation force (ARF) acting on suspended particles/cells. This numerical model is based on well-established perturbation theory whereby the second-order solutions to kinematic continuity and Navier-Stokes equations are used to calculate the time-averaged pressure and velocity fields that are associated to ARFs [76]. Our model factors in the effect of the surface vibrations within the fluidic channel, and acoustic transmissions and reflections at the material boundaries. To accurately describe the partial reflection that arises from the acoustic impedance mismatch between fluid and channel (PDMS) boundaries, a lossy-wall boundary condition is used all fluid/PDMS interfaces [36]. The acoustic reflection from the PDMS/air interface is not taken into account due to high viscoelasticity and energy absorption of PDMS that is significantly thicker than the attenuation length at ultrasonic frequencies [36, 79, 80]. It should be noted that the acoustic streaming effect associated with the non-zero second-order pressure $\langle p_2 \rangle$ is not considered in our model for the following reasons: 1) The particles we are interested in manipulating are much larger than the critical threshold size a_c from equation (1.6) that measures the relative importance between ARF and acoustic streaming induced Stokes drag force [55]. At a SAW frequency of 13 MHz, this threshold particle size is approximately 1 μm, which is much smaller than the particle size (7 μm) used in our numerical and experimental studies; 2) our operating frequencies falls in a frequency region where the attenuation lengths $1/\alpha_L$ and $1/\alpha_E$ are much larger than the characteristic channel length scales (Fig. 1-5). A more detailed description of the model setup and relevant theoretical framework is discussed earlier in section 1.6.4.

Fig. 1-18a shows the distribution of the Gor'kov potential along the *xz* plane. This field exhibits a marked spatial dependence in the *x* direction. This feature originates from the interference of the horizontal components of the two counter-propagating BAWs (Fig. 1-17c) that creates a standing pattern composed of alternating high and low potential regions, as shown by the red and blue extremes of the color map in the channel (Fig. 1-18a). In the vertical direction however, the spatial dependence of the Gor'kov field becomes relatively weak. This is associated to emergence of both large-amplitude traveling BAWs and small-amplitude standing BAWs due to the partial reflection at the fluid/PDMS interface (Fig. 1-17d). Suspended particles in this Gor'kov potential field are expected to experience ARFs pointing from high potential region (red color) to the region with lower potential (blue color). To investigate how this ARF potential field influences the trajectories of particles flowing axially along the *y* axis, we carried out a numerical simulation of tracing the real-time locations of the particles that are flowing axially along the channel in the *xz* plane. In our simulation, the particle diameter, channel height and width are 7μm, 80μm and 1200 μm, respectively. 4 V is applied to a pair of IDTs with 25 numbers of fingers and 150 μm finger spacing. The flow velocity is 1 mm/s. For convenience, only the middle region of the channel is examined in our analysis. Fig. 1-18a shows four captured representative time snapshots of the spatial locations of 8 particles (represented by the black dots) that are randomly introduced in the vicinity of the high Gor'kov potential areas in the *xz* plane. Evidently, particles migrate across the axial fluid streamline as they flow along the channel length from $t=t_0$ to $t=t_3$ (Fig. 1-18a-b). The horizontal gradient ARF acting on the particles is

responsible for their drifting motion towards the middle of the channel along the *x* axis. While the net ARF exerted on the particles that originating from the counteracting scattering and gradient ARF along the z axis drifts them vertically towards the substrate where the Gor'kov potential is minimum (Fig. 1-18a-b). At $t=t_3$, the acoustically drifted particles finally arrive on the substrate and are tightly confined in the middle of the channel.

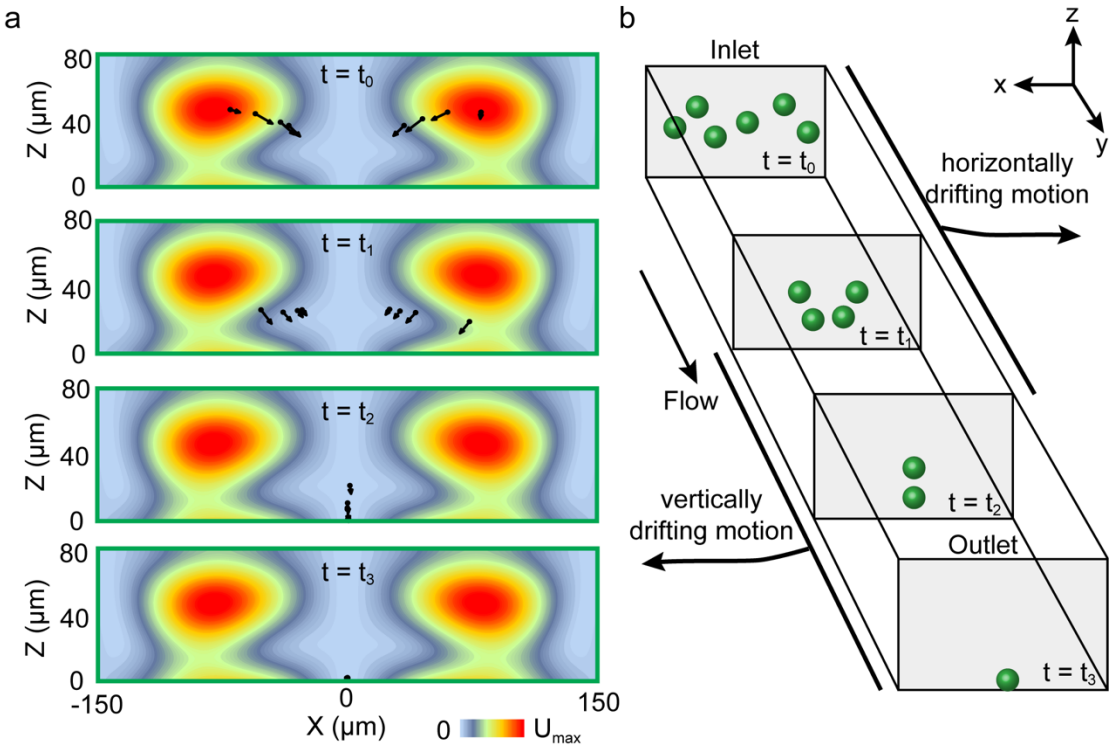

Figure 1-18. ADE enabled acoustic drifting motion of particles across fluid streamlines in rectangular microchannels. (a) Four captured time snapshots obtained from FEM simulations demonstrate the effect of a Gor'kov potential on the spatial locations of the particles that are axially flowing along the channel length. Acoustic drifting movement is enabled by the gradient ARF in the horizontal (*xy*) plane and net ARF (a competition

between a scattering and gradient ARF) in the vertical (*zx*) plane that act on the particles. (b) The entire particle motion under ADE is illustrated with cross sections outlined in grey corresponding to the time snapshots from the numerical simulation.

1.7.3 Device Fabrication and System Setup

The ADE chip assembly was designed to create a pure standing acoustic wave along channel width direction and quasi-standing acoustic wave along the channel height direction inside a microfluidic channel. This chip is consists of a straight and rectangular microfluidic channel and a pair of micron-sized interdigitated electrodes (IDTs) that are precisely and reliably fabricated using standard photolithography techniques. The fabrication process for the IDT chips and microfluidic channels is optimized to realize satisfactory fault tolerances and to minimize device operational issues. The pairs of IDTs spaced at a predetermined distance of 7 acoustic wavelengths with 25 pairs of electrode fingers and 12 mm finger overlap aare fabricated on a double-sided polished transparent 128° YX lithium niobate ($LiNbO_3$) piezoelectric substrate (500 μm) using single step contact photolithography. S1818 positive resist from Microdeposit is used in conjunction with MF-319 developer (MicroChem Corp., Newton, MA) to form a sacrificial layer for electrode patterning. After development, deposition of Ti (5 nm) and Au (120 nm) is performed via electron beam evaporation. To reveal the IDTs structures, the sacrificial layer is removed by sonicating the wafer in acetone and rinsed in DI water. Finally, a pair of IDTs is formed with a period of 300 μm (Fig. 1-19a). After fabrication, the wafer is diced into individual SSAW devices

using a diamond scriber. The microfluidic channel is fabricated using standard soft-lithography techniques [81]. A 80 μm thick SU-8 2050 photoresist (MicroChem) layer is used to create masters for PDMS casting. Features are developed using SU-8 developer from MicroChem. The Sylgard 184 silicon elastomer kit from Dow Corning are mixed at a 10:1 ratio of elastomer base to curing agent and degassed for 45 minutes prior to casting. After heat curing at 65 °C for 2 hours, the PDMS molds are removed from the silicon master (Fig. 1-19b). Individual microfluidic devices are cut from the casting and their fluid reservoirs are created using a biopsy punch of a diameter of 1.5 mm. Completed devices are cleaned with 2-propanol in an ultrasonic bath for 15 minutes. After nitrogen (N_2) blow-drying and dehydration in over, the microfluidic chip is bonded on the IDT chip using UV-ozone treatment to activate the bonding surface, at variable times (10-30 min) depending on the required bond strength (Fig. 1-19c). An optical image of the final ADE device occupying a footprint area that is comparable to a quarter dollar coin is shown in Fig. 1-19d.

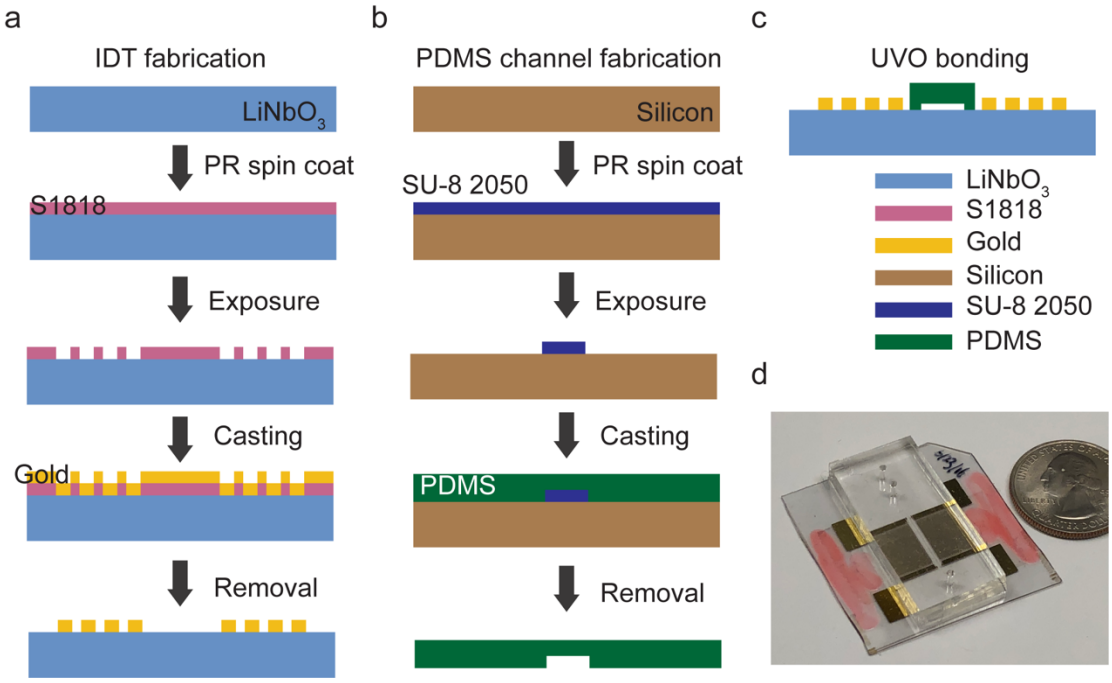

Figure 1-19. (a, b) Schematic of the lithography fabrication process of interdigitated transducers (IDTs) and straight and smooth microfluidic channels. (c) An acoustofluidic device is formed by permanently bonding a microfluidic channel on a piezoelectric substrate that is internally deposited with a pair of IDTs. An ultra-violet ozone cleaning process is employed for activation of the bonding surfaces. (d) Optical image of the fabricated device showing two fluid inlets and one fluid outlet. The device is placed next to a quarter dollar coin for size comparison purposes.

Prior to experimentation, it is important to evaluate the electrical characteristics of the fabricated ADE devices to find the experimental resonance frequencies at which the surface acoustic waves (SAWs) are most efficiently generated by the electrically activated IDTs. To obtain the highest piezoelectric coupling and minimal generation of leaky SAW, the SAW propagation direction is aligned with crystallographic Y axis.

The electrical characterizations of the ADE devices are performed in an electro-acoustic delay-line configuration using a vector network analyzer (Copper Mountain Technologies). The obtained S-parameters, including the backward reflection coefficient (S_{11}) obtained from the input port and forward transmission coefficient (S_{21}) measured at the output port [82, 83] are analyzed. Fig. 1-20a shows the experimental characterization setup, where a custom-made two-layer acrylic manifold is used. Fig. 1-20b shows the measured S_{11} and S_{21} parameters of an ADE device with its microchannel pre-filled with a 1×Phosphate-buffered saline solution (PBS). A resonant frequency of 12.9 MHz and transmission efficiency -7 dB (~45%) is obtained. Experiments are carried out on a motorized stage of a Nikon inverted microscope (Fig. 1-20d-f). Target polystyrene particles are injected through the middle inlet, while a clean PBS solution was injected through the second inlet to generate a sheath flow (Fig. 1-20d-f).

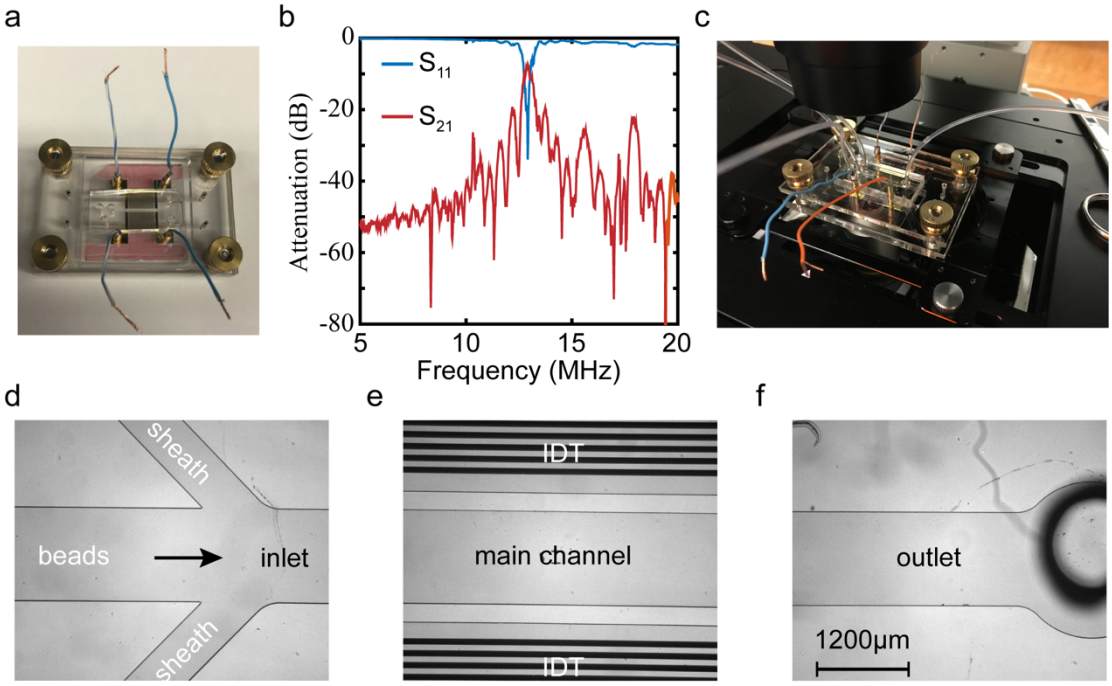

Figure 1-20. (a) A two-layer acrylic manifold housing an ADE chip is used to characterize its electrical response using a network analyzer. (b) The reflection S_{11} and transmission S_{21} spectra of the ADE device within the frequency range from 5 to 20 MHz. (c) The acoustic field flow fractionation experiment was conducted on the stage of an inverted microscope. (d-f) Optical micrographs of the microfluidic channel of the ADE device. Target beads were injected through the middle inlet, while a clean PBS solution was injected through the second inlet to generate a sheath flow in the main channel for the purpose of preventing beads adhering to and aggregating along the side walls of the channel.

1.7.4 ADE Enabled Particle Drifting in the Horizontal Plane

The horizontal gradient ARF acting on the particles is responsible for the drifting motion towards the middle of the channel in the *xy* plane. To validate our model and numerical simulations, we conducted experiments along the width of the channel (*x*-direction). By applying SSAW with a frequency of 13 MHz and an input peak-to-peak voltage of 4 V, the particles that are initially randomly injected at a rate of 4.5 μL/min through the middle inlet are lined up in an ordered manner on the low Gor'kov potential regions, forming 7 equidistantly spaced lines (Fig. 1-21a). With further analysis, the locations of these lines are found to coincide with the locations of the pressure nodes of the standing acoustic wave in the width direction that is created by the interference of two counter-propagating horizontal components of the BAWs (Fig. 1-17c). The flow behavior of the particles inside the microchannel can be analyzed by examining the horizontal ARF and Stokes drag force. Using the long acoustic wavelength approximation ($\lambda >> a$, a is the particle diameter), the horizontal ARF acting on a small particle can be expressed as [32, 43]

$$F_{SSAW} = -\left(\frac{\pi p_0^2 V_p \beta_F}{2\lambda}\right)\phi(\rho,\beta)\sin\left(4\pi x/\lambda\right) \tag{1.78}$$

$$\phi(\rho,\beta) = \frac{5\rho_P - \rho_F}{2\rho_P + \rho_F} - \frac{\beta_P}{\beta_F} \tag{1.79}$$

$$p_0 = \sqrt{\frac{\alpha P_I \rho_s c_s}{A_w}} \tag{1.80}$$

where p_0 is the acoustic pressure, α the power conversion efficiency that is determined by the S_{21} parameter of the IDTs, ρ_s the density of the piezoelectric substrate $LiNbO_3$, c_s the sound speed of the substrate, P_I the input power to the IDTs, A_w the working area of the IDTs (a product of the length of the SSAW region and the distance between IDTs), λ is the acoustic wavelength, V_p the volume of the particle, ρ_p the density of the particle, ρ_F the density of the fluid medium, β_p compressibility of the particle, β_F compressibility of the fluid medium, and x the distance away from the pressure node. Fig. 1-21b plots the ARF acting on the particle with a diameter of 7 μm as a function of the distance from a pressure node (indicated by the arrow). As expected from the equation (1.78), the ARF imposed by the standing BAWs has similar sinusoidal spatial distribution to the horizontal BAW, with a maximum force value of about 30 pN. Within the standing BAW region, particles located on the left (right) side of the pressure node experience a rightward (leftward) pointing gradient ARF. In addition to the gradient ARF, the Stokes drag force is also incorporated,

$$F_{drag} = -6\pi\eta r_P v_r \tag{1.81}$$

where η is the viscosity of the fluid medium, r_p the radius of the particle, v_r the relative velocity of the particle. Because the gradient ARF is perpendicular to the fluid flow, the velocity of the particle can be decomposed into an undisturbed axial flow velocity v_f and a velocity v_r caused by the gradient ARF. The position of the particle in the xy plane can then be analytically described by the following ordinary differential equations (ODEs):

$$\frac{dx}{dt} = v_r \tag{1.82}$$

$$\frac{dy}{dt} = v_f \tag{1.83}$$

By equating the gradient ARF and Stokes drag forces, the relative velocity of particle can be determined as

$$v_r = \frac{2\pi r_p^2 p_0^2 \beta_F}{9\eta\lambda}\phi(\rho,\beta)\sin(2kx) \tag{1.84}$$

Fig. 1-21c plots the drifting trajectory of the particle that is initially located at a quarter wavelength distance from the pressure node in the *xy* plane. The analytically calculated lateral displacement Δy needed for alignment of particles along the node is about 1100 μm, which is in near perfect agreement with the experimental measurements (indicated by the two vertical dashed red lines in Fig. 1-21a), demonstrating the accuracy of our analytical calculations.

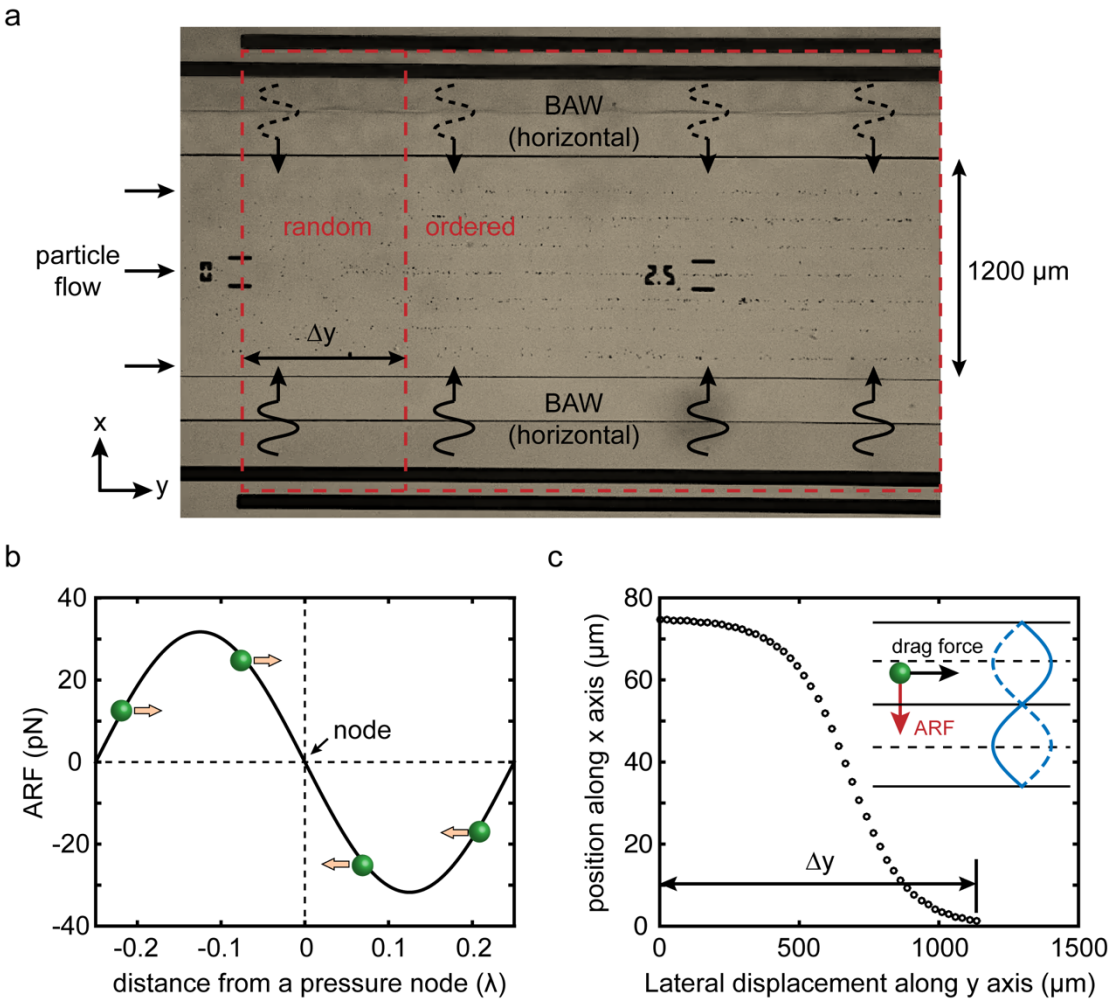

Figure 1-21. ADE enabled horizontally cell-like particle drifting. (a) An image was taken after applying a 4 V peak-to-peak voltage to the IDTs to generate interfering BAWs. A horizontal gradient ARF imposed by the standing BAWs gives rise to the horizontally particle drifting, repositioning them in an ordered manner. (b) Analytically calculated horizontal gradient ARF distribution along a standing BAW wavelength. (c) Lateral displacement of the particles that are subject to an axial Stokes drag force and a normal ARF. Inset shows the directions of the forces acting on the particle that is exposed to a standing acoustic wave field (blue curves).

1.7.5 ADE Enabled Particle Drifting in the Vertical Plane

The quasi-standing acoustic wave emerging from the partial acoustic reflection from the channel ceiling imposes counteracting scattering and gradient ARFs acting on suspended particles in the channel, leading to acoustic drifting effect. The imbalance of these two forces in the *xz* plane produces a non-zero net ARF, pushing the particles towards the substrate where the Gor'kov potential and fluid flow rate are minimal. Therefore, acoustically drifted particles are expected to flow at diminished velocities along the channel (length direction). As illustrated by Fig. 1-22a, green particles encountering the Gor'kov potential field are acoustically drifted across laminar flow streamlines towards the low Gor'kov potential areas that coincide with the pressure nodes of the horizontal standing BAWs at the surface of the substrate. Due to the parabolic flow profile of the fluidic flow in the vertical plane (*xz*), particles decelerate as they get closer to the bottom channel wall. In this scenario, particle's axial velocity is strongly correlated with the rate of change of its physical location along the z axis, hence the input voltage responsible from the ADE. In sheath flow conditions, particles are effectively away from the channel side walls. In addition, the flow profile in the horizontal plane is nearly flat in a high aspect ratio rectangular channel [11]. Hence, particles at the same distance from the bottom channel wall are expected to flow at the same speed irrespective of which pressure node where they are trapped at. To validate our theoretical predictions, we repeated the same experiment summarized in Fig. 1-21 and quantitatively investigated particle's absolute speed under different flow and ADE conditions. Three different applied voltages and three different flow rates are tested

(Fig. 1-22b). Increasing the applied voltage essentially enhances the ADE effect, i.e., the ARF force strength. While increasing the flow rate leads to larger Reynolds and Péclet numbers. As shown by Fig. 1-22b, the low particle Reynolds numbers (10^{-4}) and extremely high Péclet number ($>10^6$) clearly demonstrate that the fluidic flow in our experiment is purely laminar. To justify the independence of the particle's axial speed from its physical location along the *xy* plane, we selected and tracked the speed of a collection of particles of different *x*. Fig. 1-22b summarizes the measured velocities of the selected particles. At zero applied voltage, we observed large variations in particle speeds for the three different flow rates we tested even at the same *x*-location. To verify this variation is a result of the difference in the particle's *z*-location, we fixed the focal plane of the microscope at the bottom channel wall. We observed that the particles exhibiting high (low) flow speeds appear blurry (clear), suggesting they are far away from (close to) the substrate. For same size particles, we observe minimal changes in flow velocities within the pre-defined Gor'kov potential region, demonstrating that the flow is laminar and hydrodynamically fully developed within this area. Furthermore, particles arriving the piezoelectric substrate surface travel within a narrowly spread velocities distribution with the increased applied voltage. This striking feature reveals that the suppression of the variation is a consequence of the existence of a downward ARF that pushes the particles towards the substrate where the flow is slowest; meanwhile increasing the ARF strength allows the particles to reach closer to the substrate faster.

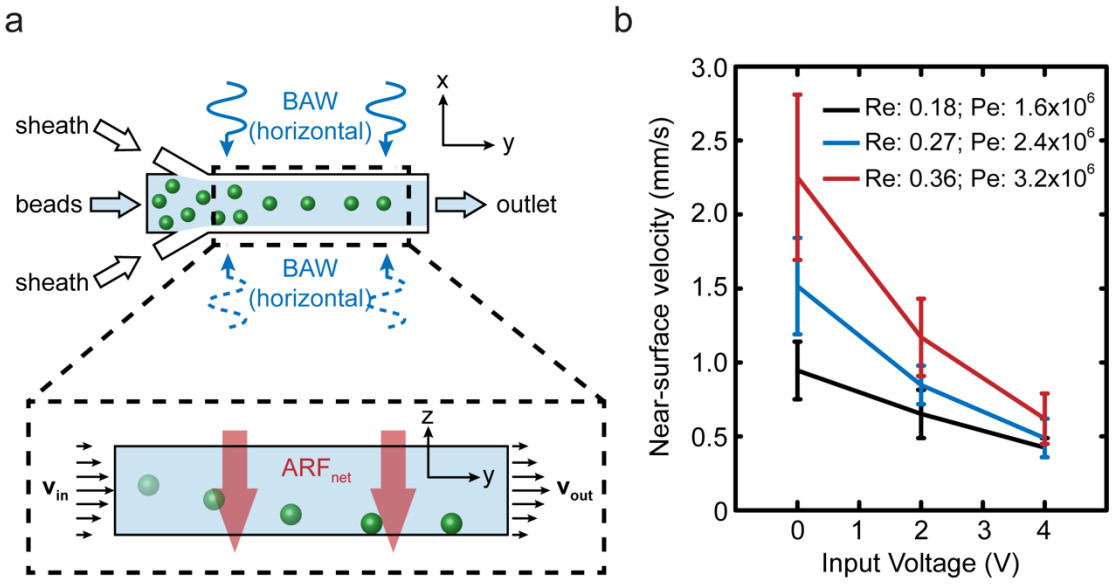

Figure 1-22. ADE enabled vertical alignment of cell-like particles. (a) Schematic of a vertically acoustic drifting process under a downward ARF imposed by a quasi-standing BAW in the *xz* plane. (b) Measured flow speeds of a collection of particles selected from different physical locations in the *xz* plane under different flow (Reynolds and Péclet numbers) and ADE (applied voltages) conditions.

1.7.6 ADE Enabled Surface Capture of Cell-like Particles and Biological Cells

Here, we exploit an affinity-based isolation technique in our ADE chip enabling efficient separation of the acoustically drifted cell-like particles and biological cells using immuno-affinity interactions. To succeed in capturing the target particles on the surface, high affinity avidin/biotin binding mechanism is employed (Fig. 1-23a) [84]. Here, a mixture of low-concentration green fluorescent polystyrene particles of 7 μm diameter (Spherotech) and 100 times more concentrated non-fluorescent polystyrene

particles of nearly same size (Spherotech) is injected through the middle inlet (Fig. 1-23b). PBS buffer is inroduced through the side inlets to establish sheath flow. Under an applied voltage of 4 V, both green and non-fluorescent particles (appear black in Fig. 1-23b-e) acoustically drifted to the minimal Gor'kov potential field region, as revealed by the nodal lines formed by the non-fluorescent particles and their diminished velocities. In less than 2 seconds after entering the ADE region, biotin functionalized green fluorescent (non-fluorescent) particles are captured by the avidins immobilized on the piezoelectric substrate. We utilized a lithographic marker "0" that is deposited on the substrate to precisely adjust the focal plane of the microscope to the substrate surface. The immobilized green fluorescent particles are found to be in nearly perfect focus, suggesting its physical location was right at the substrate. On the other hand, the non-fluorescent particles without a biotin coating continued their motion along the substrate at a diminished speed. Although drifted towards the channel walls, these particles are not captured due to the lack of immuno-affinity interactions. This remarkable feature demonstrates the effectiveness of our ADE chip in overcoming the mass transport limitations and affinity-based selective separation of particles.

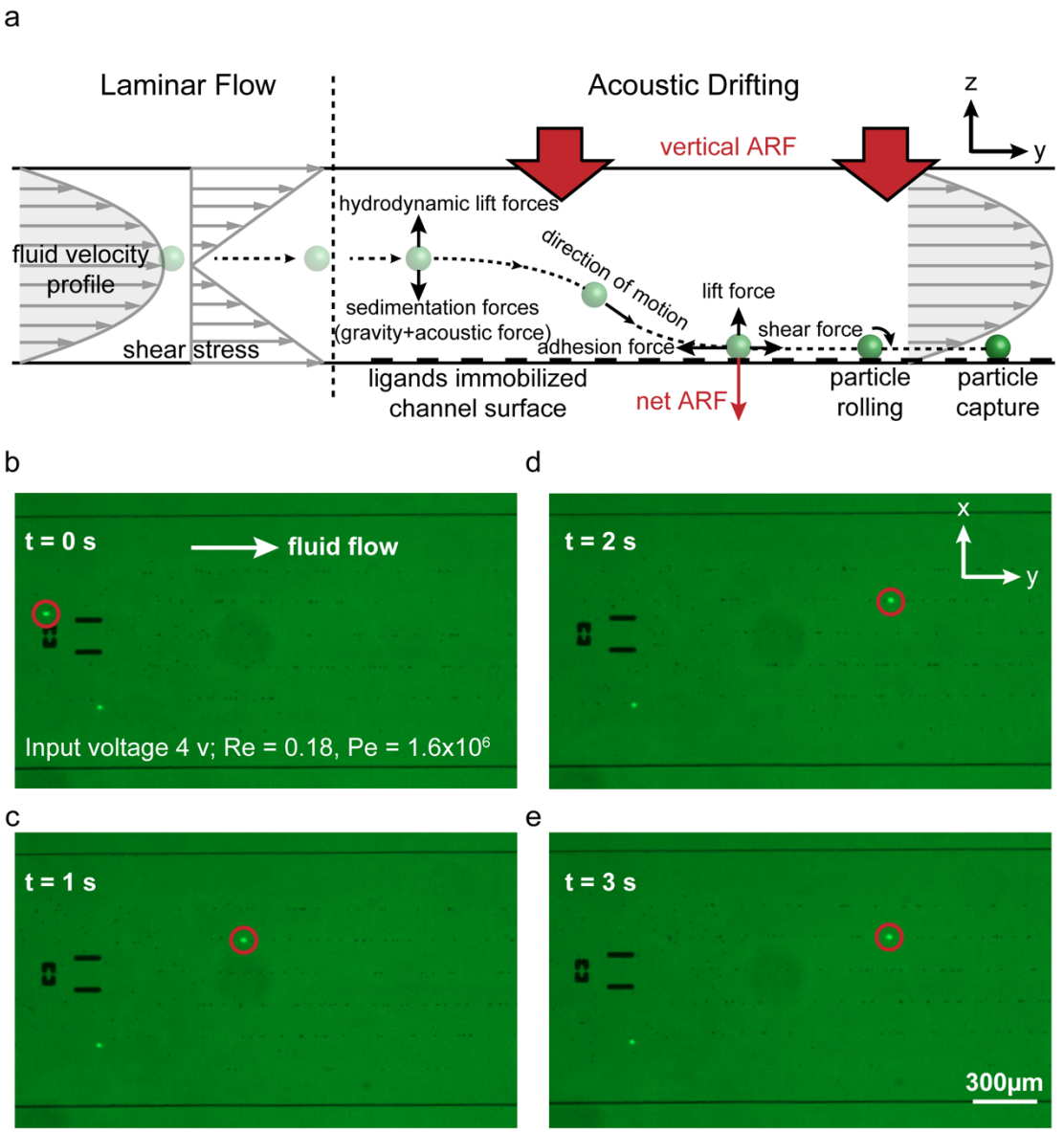

Figure 1-23. Acoustic field flow fractionation for affinity-based cell-like particle separation. (a) Schematic of capturing acoustically drifted cell-like particles on the surface. This surface capture is achieved by forming a strong biomolecular bond between the particle and surface that overcomes local shearing forces. (b-e) Four captured high-speed images showing the trajectories of green fluorescent biotin coated particles and non-functionalized particles (appear in black) under an applied voltage of

4 V. The avidin-biotin adhesive bond formed between the green particle and the avidin functionalized surface results in its arrest and immobilization within 2 seconds of travel time. In contrast, the motions of the non-fluorescent particles were never stopped due to their weak interactions with the surface.

The effectiveness of selective capture of particles/cells on a piezoelectric surfaces is controlled by the competition of specific biomolecular adhesive bonds and local shearing forces near the surface. We examined representative individual flow trajectories for both biotin-coated and pristine cell-like particles near the surface of the piezoelectric substrate functionalized with avidins. The measured velocities of both biotin coated and non-functionalized particles rapidly decreased as the particles are acoustically drifted towards to surface and then maintained a diminished but constant speed. Due to the lack of specific biomolecular bond with the surface, the strong local shearing forces lead to constant velocity drifting of the non-functionalized particles (Fig. 1-24a-b). In contrast, the decreased motion promote the chemical reactions in between the biotin coated particles and the surface, leading to progressively reduced lateral velocities. The competition between the local shearing forces and the adhesive bonds leads to strong fluctuations in the velocity profile of the biotin coated particles. Nevertheless, within few seconds of travel time, the biotin coated particles are arrested on the surface completely (Fig. 1-24c-d). At faster flow rates however, velocity fluctuations become more pronounced and longer travel times are required for particles to be captured (blue and red curves).

As shown by the inset in Fig. 1-24c, the travel time required for particle capture is much shorter for a 4 V applied voltage (red curve) than that for a 2 V (black curve). It should be noted that these instantaneous velocity and displacement trajectories provide valuable information in quantitatively determining the vertical downward net ARF acting upon the particles. By relating the particle's speed with its physical location (Fig. 1-22b) and applying the similar method that has been used in the previous calculation of the particle's lateral displacement (Fig. 1-21c), the amount of the downward ARF exerted on the particle is found to be approximately 5 pN. When the particles are near the surface, they also experience a lift force that originates from the "wall effect", which can be found to be about 1 aN by evaluating $F_L = f_L \rho u_m^2 a^6 / D_H^4$ [12, 16, 85]. Evidently, the applied ARF is more than sufficient to overcome the opposing lifting force, allowing particles to interact the surface efficiently.

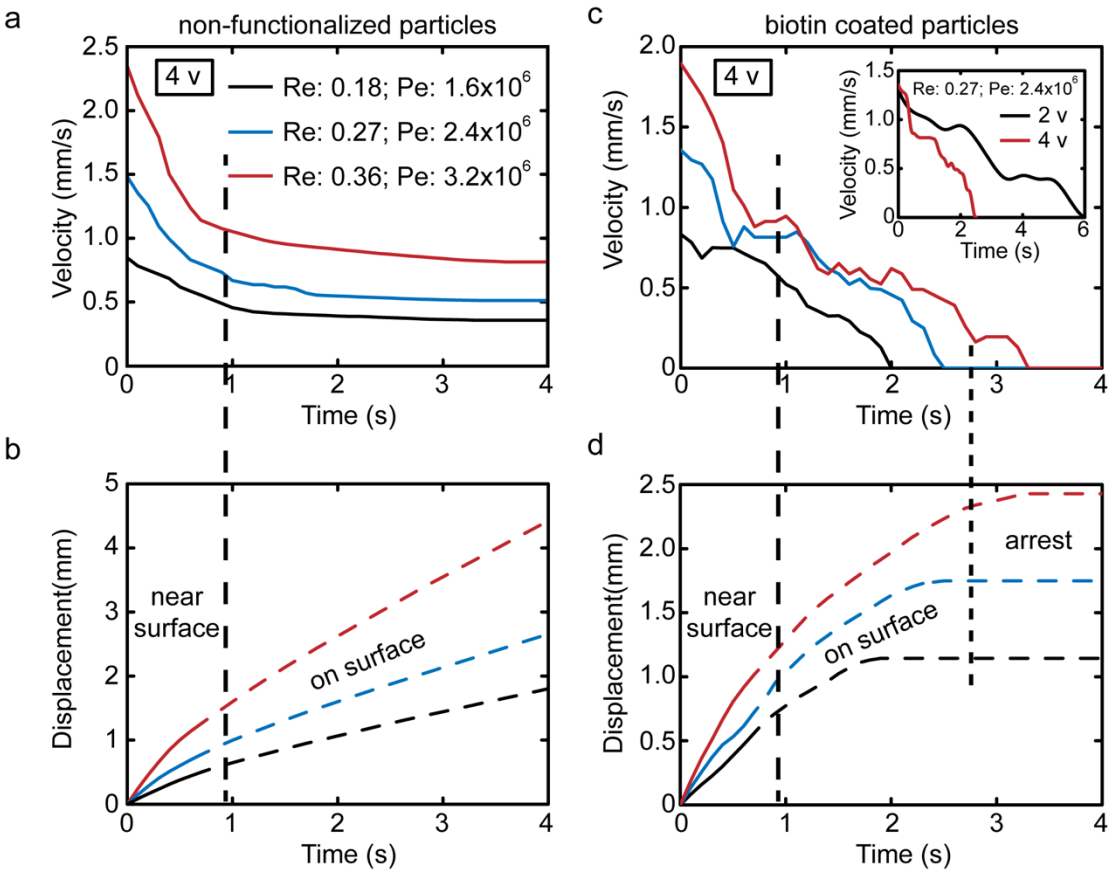

Figure 1-24. Instantaneous velocity and displacement trajectories for (a-b) non-functionalized and (c-d) biotin coated cell-like particles that are acoustically drifted to the substrate that is pre-functionalized with avidins under an application of 4 v voltage. Inset shows the enhanced local shear stress that impedes the interactions between the particles and surface can be overcome by increasing the strength of the ARF acting on the particles.

One critical issue associated with most affinity-based cell-like particle or cell capture platforms is the formation of stagnant layers of particles or cells from non-target background population [86, 87]. These stagnant layers degrade device performance

because they act to reduce the interaction between target cell-like particles or cells and the capture surface. Especially when the background particles/cells are highly abundant, their non-specifically attachments to the capture surface promote fouling and render the surface to become caked, blocked, and eventually useless for selective capture of low-abundance target particles/cells [88]. One effective way to suppress fouling is to lower the weight of the flux of particles/cells being transported to the capture surface relative to the flux of them being translated across the capture surface by local shearing forces [86]. However, this approach comes at a price of low capture efficiencies for target particles/cells as the strong local shear stress could dominate over the adhesive bonds between them and the capture surface. Here, we systematically investigated the effectiveness of our ADE chip in selective capture of scarce biotin coated particles that are mixed with non-functionalized particles with orders of magnitude higher concentrations under different experimental conditions. We control the flux of particle transport and the local shearing force by adjusting the voltage applied to the IDTs and fluid flow rate. Three different voltages and five different flow rates were tested. The capture efficiencies of biotin coated and non-functionalized pristine particles are measured and plotted as a function of input voltage (Fig. 1-25a) and flow rate (Fig. 1-25b), respectively. When no voltage is applied to the IDTs, nearly zero capture efficiency is observed for both biotin coated and non-functionalized particles (Fig. 1-25a), reflecting the fundamental mass transport limitation. With a mixture of biotin coated and non-functionalized particles at a ratio of 1:200, non-specific capture of non-functionalized particles is minimal (~0.1-1%) due to the lack of adhesive bonds and the

capture efficiency slightly increases with increasing voltages (Fig. 1-25a) but rapidly decreases with increasing flow rates due to enhanced local shear stresses (Fig. 1-25b). In comparison, for the biotin coated particles, the capture efficiency is about two orders of magnitude higher at a low applied voltage (2 V) or a fast flow rate (channel *Re*=0.54). As shown by the red bars in Fig. 1-25a, the capture efficiency is boosted from 50% to 95% when the voltage is increased from 2 to 4 V. There is minimal impact of the non-specifically captured non-functionalized particles on the capture efficiency for the target particles. As expected, the capture efficiency of the biotin coated particles is also shear-dependent, as shown by the gradual efficiency decrease from 95% to 55% with increasing flow rates (Fig. 1-25b). In laminar flow, the local shear stress is found to be proportional to the flow rate, as shown by the inset. Therefore, to maximize capture efficiency, the shear stress needs to be well controlled.

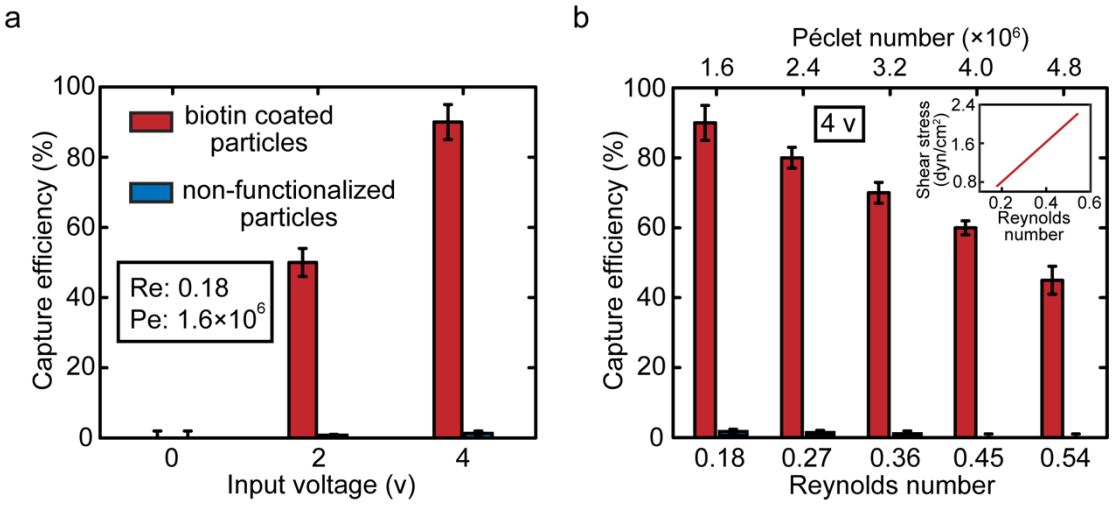

Figure 1-25. Capture efficiencies of biotin coated (in red) and non-functionalized particles (in blue) under different flow rates and voltages applied to the IDTs. (a) At a fixed input flow rate, higher voltage leads to higher capture efficiency for both of the

particles. When the applied voltage is zero, neither of the particles are captured on the surface due to the fundamental mass transport limitation. (b) At a fixed input voltage, the capture efficiency of both particles decreases with increasing flow rates. The inset shows that the local shear stress is proportional to the velocity.

1.7.7 Acoustic Streaming Flow in the ADE Chip

The acoustic streaming in our ADE chip is expected to be minimal because the size of the particles we used is much larger than the critical threshold size that measures relative importance between ARF and acoustic streaming induced Stokes drag force [55]. To verify our predictions, we carried out a fluid mixing experiment by injecting an orange dye solution through the middle inlet at a rate of 4.5 μL/min, and a green dye solution through the second inlet at a rate of 1 μL/min. As shown by Fig. 1-26a, a sheath flow is formed by three fluid layers. When a voltage of 4 V is applied to the IDTs, we observed minimal changes in the sheath flow pattern, suggesting minimal fluidic mixing in the channel. Therefore, the acoustic streaming does not play a role in our ADE chip, confirming the acoustic drifting motion is exclusively resulted from the Gor'kov potential field.

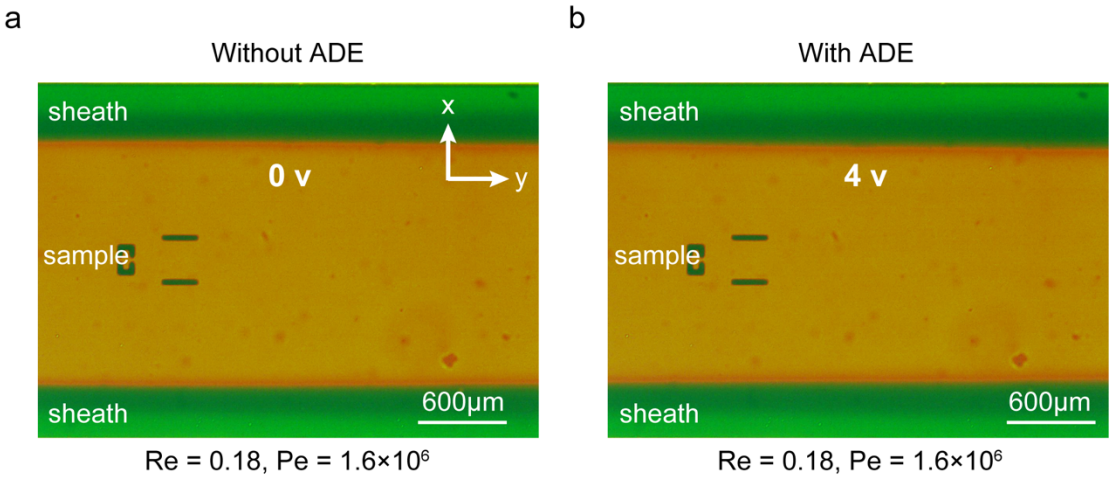

Figure 1-26. Fluidic mixing examination under ADE. Distribution of three fluidic layers is shown (a) before and (b) after applying a voltage of 4 v. Minimal mixing between fluid layers is observed.

1.7.8 ADE Enabled Surface Capture of T Lymphocytes (T Cells)

To explore potential applications of this ADE technology, we carried out selective cell capture experiment using our ADE chip. A mixture of high-concentration (~10^6/ml) white blood cells (WBCs) and low-abundance (~10^4/ml) T lymphocytes obtained from mouse bone marrow were injected at a rate of 20 μL/min through the middle inlet of the ADE chip and a PBS buffer was injected at a rate of 1μL/min through the second inlet to establish small sheath regions near the sidewalls of the channel in order to prevent cells from sticking to the walls. To capture more cells, we used a larger channel width of 2400 μm to increase the cell capture surface area. To enhance cell-surface interactions, we coated the surface with avidins that strongly bind to the biotinylated

antibodies that show high specificities to the molecular biomarkers expressed on the T cell surface. When a three-dimensional Gor'kov potential field was established by applying a voltage of 5 V to the IDTs, both WBC and T cells were acoustically drifted towards the piezoelectric surface (Fig. 1-27a). Due to lack of complementary bonds and strong local shearing forces, the white blood cells were found to translate along the surface with a diminished but unvaried velocity. On the contrary, the local shearing forces are overcome by the strong interactions between the antibodies and the T cell surface molecular biomarkers, giving rise to a rapid rolling and translation across the surface. This rolling motion boosts the reaction times and facilitates the formation of strong adhesive bonds between the T cells and the surface, leading to a selective capture of the cells (Fig. 1-27b). We experimentally demonstrate a separation efficiency of approximately 80% for the T cells at a high flow rate of 1.2 mL/hr, a separation efficiency that is comparable to most advanced rare cell isolation technologies.

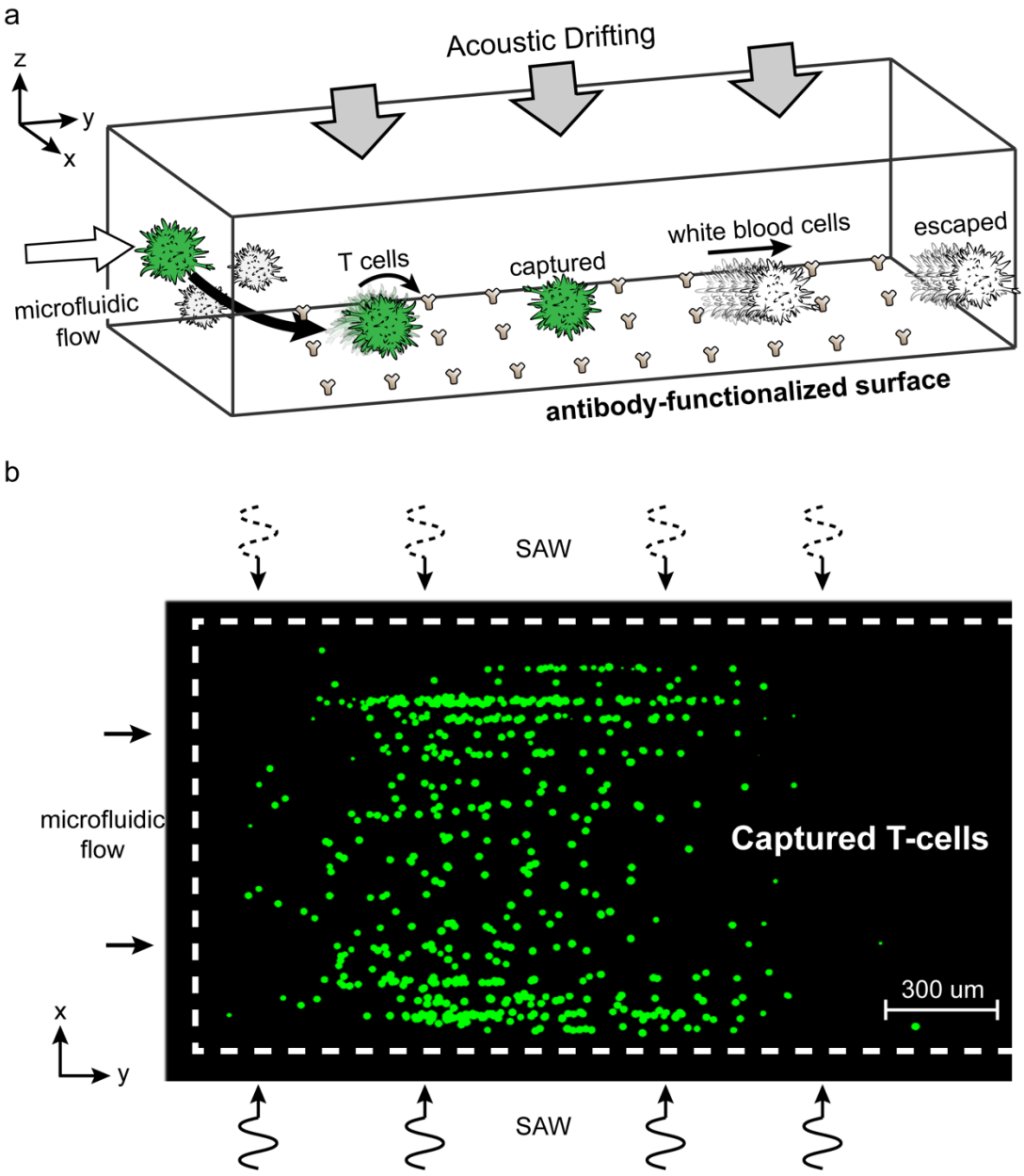

Figure 1-27. (a) Schematic of acoustic drifting effect (ADE) enabled selective capture of T lymphocytes (T cells) on the piezoelectric surface that is pre-functionalized with the antibodies against the T cell surface membrane proteins. Due to lack of complementary bonds and strong local shearing forces, white blood cells translate across the surface and eventually exit from the channel. (b) After applying a voltage of

5 V to the ADE chip for five minutes, nearly 80% of the injected T cells tagged with green fluorophores were captured on the surface of the piezoelectric substrate.

1.8 Summary

In conclusion, in this chapter, we introduce a novel acoustic drifting effect (ADE) based field flow fractionation (FFF) technique that offers precise, controllable, physical contact-free, and multi-dimensional manipulation as well as characterization capabilities for cell-like particles and T lymphocytes. The ADE standing surface acoustic waves (SSAWs) that are generated at safe power (~ 1 W/cm^2) and frequency (~10 MHz) levels similar to those used in ultrasound imaging (e.g. fetal imaging). This active ADE method effectively breaks impractically slow molecular diffusion processes without disrupting the fluid dynamics and achieves high-efficiency all-acoustic convective transport and surface capture of microscale cell-like particles and biological cells in microfluidic channels at extremely low dimensionless Reynolds number (Re~10^{-4}) and high Péclet number (Pe~10^6). Using this method, two major limitations relevant to conventional microfluidics systems with high surface-to-volume ratios are overcome. One is the fundamental mass transport limitation that is associated with the inherent diffusion-limited laminar flow nature. The other is the restricted interaction between macroscopic objects and channel boundaries due to strong local shear stresses and "wall effect". This method uses a straight and smooth microchannel and a pair of micron-sized interdigitated electrodes that are precisely and reliably fabricated in a high-throughput manner with standard photolithography techniques that

are commonly used in fabricating integrated circuits. The ADE platform occupies a footprint area that is comparable to a quarter dollar coin. We demonstrate a nearly 100% capture efficiency of target cell-like particles and 1000-fold less capture efficiency of background non-target particles using an affinity-based selective particle capture approach. We explore potential practical applications of the ADE technology in selective capture and isolation of low-abundance biological cells (T lymphocytes) from high-abundance background cells (white blood cells).

Chapter 2

Radiatively Coupled Plasmonic Nanoantenna Arrays for High-Efficiency Photo-Inactivation of Multidrug-Resistant Bacteria

This chapter presents a novel nanophotonic approach for enhanced inactivation of multidrug-resistant bacterial pathogens using visible light at 405 nm. To achieve this, I introduce precisely engineered aluminum nanoantenna arrays using a space mapping algorithm enabling inverse design of nanostructures with the desired optical response. The nanoantenna arrays are optimized using radiative decay engineering principles to maximize the near-field enhancements and photothermal heating at 405 nm, a wavelength which bacteria is extremely vulnerable. In our experiments with low illumination intensity light (2.5 mW/mm^2), we demonstrate that our aluminum nanoantenna array (ANA) enables rapid eradication (~20 min) of multidrug-resistant *Vibrio Cholerae* biofilms with more than 500-fold inactivation efficiency (~99.995%) with respect to the 405 nm light alone.

2.1 Motivation

Cholera remains a major public health threat worldwide, causing an estimated 4 million infection cases of acute watery diarrhea and over 100,000 deaths each year [89]. Toxigenic *Vibrio cholerae* bacteria is responsible for seasonal explosive outbreaks of

endemic cholera particularly in megacities of the developing world [89-91]. Inadequate sanitation facilities and poor hygiene in these regions not only promote the spread of this disease through various mechanisms such as biofilm formation [89, 92] but also result in the emergence of "superbugs" with exceptionally high antimicrobial resistance via transmission of antibiotic-resistance among microorganisms and the excessive use and abuse of antibiotics [93]. Widespread overuse of antibiotics has led to emergence of multidrug-resistant (MDR) bacteria placing tremendous pressure on public health worldwide. According to the recently released data by Infectious Diseases Society of America (IDSA), the MDR infections are becoming the third leading cause of deaths (~160,000 deaths annually) in the United States [94]. Therefore, it is essential to develop reliable and effective approaches to eradicate the burden of diarrheal disease by efficiently inactivating *Vibrio cholerae* bacteria.

The use of high-intensity narrow-spectrum violet-blue 405-nm light has emerged as a "no-touch" decontamination technology and attracted significant attention [95-98]. 405 nm bactericidal light, producing highly cytotoxic reactive oxygen species (ROS) that result in an intracellular killing effect [97, 99] has been demonstrated to be remarkably effective in photo-inactivation of a variety of medically important bacteria species regardless of their drug-resistance profiles [95-100]. Unlike ultraviolet (UV) light, visible 405-nm light can be safely used in occupied environments [97] without exogenous photosensitizers [100]. However, inactivation efficiencies with 405 nm light is still much lower than UV radiation.

Plasmonic nanoantenna can provide strong light localization and dramatically enhanced near fields via resonantly driven localized surface plasmon resonances (LSPRs) [101-103]. One can exploit plasmonic excitations to realize drastic intensity enhancements at 405 nm wavelength and improve the light-matter interactions for more effective light treatment. Furthermore, the high intensity hot spots formed at the nanoantenna surfaces associated with strong spectral selective near-field light absorption can be harnessed to generate increased deactivation with local heating to induce irreversible damage to bacterial cell membrane. Hence, the efficiency of bacteria inactivation with 405 nm light can be significantly improved with a well-engineered plasmonic devices.

A high degree of optical field localization and enhancement at subwavelength scales through collective oscillations of conduction band electrons supported by plasmonic nanoantennas has propelled significant advancements in a vast array of technologies including single-molecule fluorescence [104], surface-enhanced Raman spectroscopy [105], photovoltaics [106], light-emitting devices [107, 108], and biosensors [109]. However, plasmonic nanoantennas are typically associated with spectrally broad (~ 100nm linewidth) localized surface plasmonic resonances (LSPRs), owing to dynamic depolarization as well as nonradiative and radiative damping. In particular, the latter is primarily responsible for poor quality LSPRs for aluminum nanoantennas at shorter wavelengths, which severely hinders the local field enhancements and thus the light-matter interactions in the nanostructures. One effective approach to overcome this fundamental limitation is to pattern nanoantenna ensembles into one- or two-

dimensional regular arrays. By appropriately arranging the grating order to be evanescent, far-field radiative coupling in the nanoantenna arrays can be efficiently used to suppress the radiative decaying of plasmonic excitations, resulting in a remarkable improvement in the quality of LSPRs and marked enhancement in the intensity of localized optical fields [110, 111].

Despite holding potential for unprecedented technological advances, engineering and controlling of radiative field coupling has remained challenging. This is predominantly due to a lack of computationally efficient and cost-effective algorithms to allow systematic exploration of a full design space of attainable devices according to desired functional characteristics. Especially, when multiple device performance requirements (resonant wavelength, linewidth, etc.) need to be met simultaneously, optimization becomes a strenuous and even formidable task due to expanded design complexity. Traditional strategies for device design are based on a semi-analytical model and physical intuition, followed by fine-tunings of a narrow set of distinct structural parameters (nanoantenna dimension/geometry, array period, etc) using time-consuming and computationally expensive brute-force full-wave numerical electromagnetic modeling. Conceivably, this trial-and-error or iterative parameter search procedure would require demanding computational schemes when the investigation of a multitude of design possibilities is required to unveil the performance limit for a particular device.

Furthermore, widely adapted top-down fabricated devices raise an unavoidable fundamental constraint associated to the refractive index mismatch occurring at the

interface between the substrate and superstrate. This strong index asymmetry considerably undermines the radiative field coupling in the nanoantenna arrays due to altered constructive interference conditions [112]. Although applying an index matching oil around the nanoparticles [113] or burying the particles into the substrate [111] offers marginal improvements in resonance quality factor and near-field enhancement, little is known about whether the claimed optimal structures have really approached or reached their performance limits. Furthermore, it is not always possible to find index matched substrate and superstrate for practical applications.

In this thesis, we propose and demonstrate a space mapping (SM) methodology addressing the high computation-cost and slow design-verification issues inherent in conventional design optimization techniques. Unlike the trial-and-error parametric search strategy, our approach offers a significant reduction of enormous design space to a small set of candidate structures. It minimizes the number of high-fidelity and computationally expensive model evaluations and enables fast and self-consistent convergence to the optimal design parameter sets that meet all pre-defined specifications. To demonstrate the SM approach, we apply this algorithm to inversely design aluminum nanodisk arrays (ANAs) according to the target device specifications, i.e., concurrent maximization of near-field intensities and plasmon lifetimes in the ANAs at 405-nm. Finally, from the outcome of the SM, we fabricated ANAs on a 4-inch fused silica wafer and measured their far-field optical response by dark-field scattering microscopy, yielding excellent agreement with the optimization targets. The approach facilitates (i) occurrence of electric-field enhancement and extinction

spectrum maxima at the target wavelength, (ii) a considerably narrow plasmon resonance lineshape, (iii) significantly enhanced near-fields despite the native oxide layer surrounding Al nanodisks.

2.2 Space Mapping Working Principle

In a general design optimization problem, a model is employed to directly solve the following equation to obtain the optimal solution [114, 115]

$$x_f^{optimal} = \arg\min_x U(R_f(x)) \tag{2.1}$$

where x is the vector of n_{th} design parameters, R is a vector of m_{th} responses of the fine model, U is a suitable objective function, the subscript f indicates the fine model. By satisfying the upper and lower specifications for the objective function U, the optimal solution $x_f^{optimal}$ can be determined. This optimization process is usually performed with a computationally expensive, CPU- and time-intensive fine model, rendering the optimization unrealistic in practice.

However, the SM approach circumvents and replaces this time-expensive optimization process by iteratively updating and optimizing a calibrated computationally less demanding physics-based coarse model [114]. With the SM approach, the design optimization can be considerably accelerated by calibrating the low-fidelity coarse model with the high-fidelity fine model that accurately describes design specifications [114]. The coarse model is typically much less resource hungry but less accurate than the fine model. For instance, it may be a circuit theory with mathematical formulations or an empirical coupled-harmonic-oscillator model, corresponding to a CPU- and time-

intensive finite element solution of Maxwell equations (Fig. 2-1a). In a SM framework, an intelligently mathematical link is usually established between spaces of the parameters of a coarse model and a fine model of the same physical system by matching their responses. This one-to-one mapping is conceptually illustrated by Fig. 2-1a, where the coarse (x_c) and fine (x_f) model parameters are related through

$$x_c = P(x_f) \tag{2.2}$$

such that

$$R_c(x_c) = R_c(P(x_f)) \approx R_f(x_f) \tag{2.3}$$

which exists in a region of interest. Instead of directing solving the equation (2.1) to find the optimal parameter sets with a computationally expensive fine model, a good estimate of the fine model solution can be found by solving the following inverse mapping relation

$$\hat{x}_f \triangleq P^{-1}(x^{optimal}) \tag{2.4}$$

where $x_c^{optimal}$ is the result of the coarse model optimization.

Based on the above general SM approach scheme, we propose a surrogate SM algorithm that is executed as follows: 1) first select a physically based coarse model for the fine model; 2) then select a mapping process to match the two model responses; 3) choose a starting point (initial parameter set) for the fine model based on the coarse model optimization result; 4) subsequently the fine model response is evaluated at these design parameters; 5) If the pre-defined SM criteria are satisfied, the whole optimization procedure will be terminated (e.g. response meets specifications).

Otherwise it proceeds to the next step; 6) a parameter extraction is applied to (re)align the coarse model with the fine model to permit calibration, such that a specific alignment parameter can be found by solving equation (2.3); 7) (re)build a surrogate coarse model based on the information from the previous step; 8) then a (re)optimization process is carried out to enhance the coarse model, obtaining a new prediction of optimal design parameter sets; 9) subsequently go to step 4. The SM optimization steps are summarized by the flow chart, presented in Fig. 2-1b. It should be noted that the parameter extraction step is the key to establishing the one-to-one mapping and refining the surrogates to better approximate the corresponding fine model. Furthermore, to assure rapid convergence to the optimal design, two essential requirements for the coarse model need to be met: 1) extraordinarily low computational complexity and cost, 2) sufficiently faithful to have excellent alignment capability with respect to the high-fidelity computationally expensive fine model.

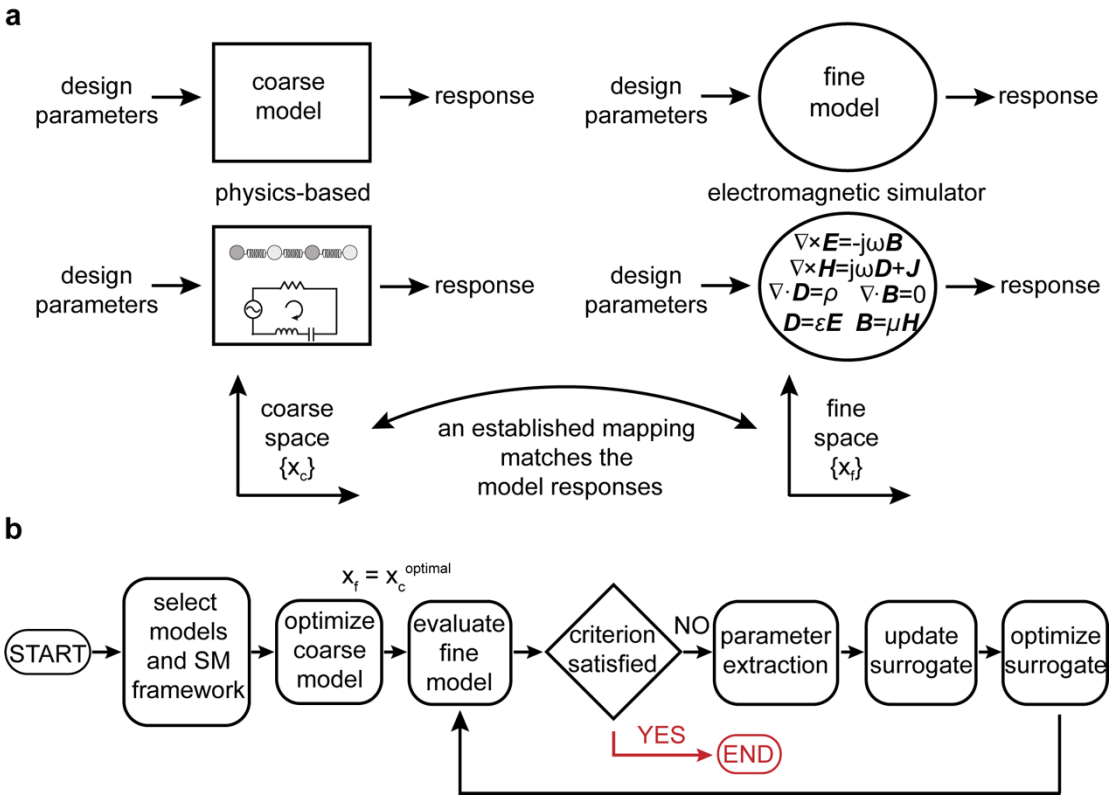

Figure 2-1. Overview of the inverse design process using the space mapping algorithm. (a) A mapping is established to link a companion physics-based coarse model with a computationally expensive fine model. (b) A flowchart showing the implementation of a SM algorithm.

2.3 Aluminum Plasmonic Nanoantenna Array

Herein, we demonstrate the capabilities of our SM algorithm by designing and experimentally demonstrating monolithically integrated aluminum (Al) plasmonic nanoantenna arrays grown on a fused silica substrate in an aqueous environment. The key motivation for optimizing aluminum plasmonic structures is that aluminum is a compelling plasmonic material for high-energy ultraviolet (UV) and near-UV

plasmonics [101, 109, 116]. It has recently taken much attention due to a wide range of potential applications spanning from detection of biomarkers exhibiting strong native absorptions [117] to solar energy harvesting [106, 118] and photocatalysis with hot electrons [119]. Al has some unique properties in this high frequency regime offering light localization beyond light diffraction limit and outperforms both silver and gold in the UV regime. With a high free electron concentration in the conduction band, aluminum exhibits a bulk plasma frequency $\omega_p \approx 15$ eV that is much higher than that of silver and gold ($\omega_p \approx$ 8-9 eV). This allows the real part of the permittivity of aluminum to be a negative value over a broader spectral range allowing surface plasmonics with high-energy photons down to ~200 nm wavelength in the UV regime. Furthermore, being the third most abundant element in the Earth's crust, Al is a low-cost alternative to noble metals with well-established manufacturing capabilities allowing mass production of the metallic Al and processing compatibility to complementary metal-oxide semiconductor (CMOS) technology.

Most recently, Knight et al discussed a wealth of potential applications of Al nanostructures in high-area, low-cost-CMOS-compatible, on-chip plasmonic nanoantennas, waveguides, and interconnects [101]. However, a strong limitation to the advancement of Al plasmonics has been the weaker near-field enhancements (or poor quality-factor of plasmon resonance) relative to noble metals, and it is an issue that has not been addressed in previous studies [120-122]. Al is subjected to the quick formation of a self-terminating and few-nanometer-thick layer of native aluminum oxide (Al_2O_3) upon exposure to ambient conditions [123]. The occurrence of this native

oxide layer causes red-shifting and linewidth broadening of the plasmon resonance of Al nanoparticles with respect to the pure-metal case, degrading near-field enhancements [101]. Beyond single plasmonic nanostructures, approaches based on near-field couplings through hybridization of fundamental plasmonic modes (e.g. dimers, hexamers) provide slightly enhanced local field intensities [124-127]. Nevertheless, these approaches face several scientific and technical challenges: (i) the hybridized modes are typically dark thus cannot easily be excited by external light; (ii) tunability of localized surface plasmon resonance (LSPR) to application specific wavelength is quite limited; (iii) device fabrication is challenging due to demanding critical dimensions (~1-10 nm) of the near-field coupled surfaces; Therefore, near-field coupling based approaches would not improve the weak enhancement factors in practical Al plasmonic devices. Instead, we exploit far-field couplings among ensembles of nanoparticle arrays to suppress the radiative decay channels and enhance the strength of the near-fields [110, 111, 128]. However, far-field couplings among nanoparticle arrays involve several design parameters, which may require time-intensive simulations of hundreds of candidate-designs before narrowing down to the most promising ones.

2.4 Overview of the Space Mapping Algorithm

To overcome this limitation, we apply a space mapping (SM) algorithm combining analytical (low-fidelity) and full-wave electromagnetic (high-fidelity) simulations to allow rapid convergence to the optimal device parameters, meeting the desired spectral

and near-field responses. Our inverse design approach is general and allows one to 'design by specification', whereby one simply specifies desired device performance and the algorithm finds the fittest structure that concurrently satisfies multiple requirements. Furthermore, it also allows us to design structures independently from the type of materials chosen and the complex interfaces the devices are fabricated at.

For proof-of-principle demonstration of the SM algorithm, we apply it particularly for the inverse design of an aluminum nanoantenna arrays (ANAs). In the following sections of the thesis, we describe the implementation of the SM algorithm for the inverse design of this ANA device by following the basic steps in the above flow chart (Fig. 2-1b). In summary, we first define the device performance by defining a set of desired specifications imposed on the far-field optical response of an aluminum nanoantenna array (ANA) device, i.e., (i) extinction spectrum maxima at the target wavelength (405 nm), (ii) extremely narrow resonance linewidth (~15 nm). And then introduce a computationally efficient coarse model to find the optimal design parameters to meet all the required specifications (steps 1 and 2 in Fig. 2-1b). Subsequently, we introduce a computationally-intensive fine model for accurate evaluation of the optimized design parameters obtained from the coarse model (steps 1 and 3 in Fig. 2-1b). Later, we introduce a parameter extraction to align the parameter spaces of the two models by establishing a one-to-one mapping to refine the parameter search (steps 5-7 in Fig. 2-1b). Lastly, we iterate the SM optimization process until the optimal solution satisfying the desired requirements emerges. It should be noted that

the desired specifications (peak wavelength and linewidth) are kept fixed during the entire SM optimization process.

2.5 Space Mapping Algorithm Implementation

2.5.1 Coarse Model

The coarse model employed for the inverse design of ANAs is a coupled dipole approximation (CDA), a general framework for modeling the optical response of an ensemble of nanoparticles arranged in a periodic array. In the CDA method [110-112, 129, 130], we approximate an ensemble of N identical nanoparticles as an ensemble of N identical electric dipoles, whose positions and polarizabilities are denoted $\boldsymbol{r}_i$ and α_i. The induced polarization $\boldsymbol{P}_i$ in each nanoparticle in the presence of an applied plane wave field is $\boldsymbol{P}_i = \alpha_i \boldsymbol{E}_{\mathrm{loc},i}$ (i = 1,2,…,N), where the local field $\boldsymbol{E}_{\mathrm{loc},i}$ is the sum of the incident ($\boldsymbol{E}_{\mathrm{inc},i}$) and retarded fields ($\boldsymbol{E}_{\mathrm{dipole},i}$) of the other N-1 dipoles at the nanoparticle position $\boldsymbol{r}_i$. For a given wavelength λ, this field may be written as

$$\boldsymbol{E}_{loc,i} = \boldsymbol{E}_{inc,i} + \boldsymbol{E}_{dipole,i} = E_0 \exp(i\boldsymbol{k}\cdot\boldsymbol{r}_i) - \sum_{\substack{j=1 \\ j\neq i}}^{N} \exp(i\boldsymbol{k}\cdot\boldsymbol{r}_{ij})\boldsymbol{C}_{ij}\cdot\boldsymbol{P}_j \tag{2.5}$$

where i = 1,2,…,N, E_0 and $k = 2\pi/\lambda$ are the amplitude and wavenumber of the incident plane wave, respectively. The dipole interaction matrix C_{ij} without the phase term may be expressed as

$$\boldsymbol{C}_{ij}\cdot\boldsymbol{P}_j = k^2 \frac{\boldsymbol{r}_{ij}\times(\boldsymbol{r}_{ij}\times\boldsymbol{P}_j)}{r_{ij}^3} + (1 - i\boldsymbol{k}\cdot\boldsymbol{r}_{ij}) \times \frac{\left[r_{ij}^2\boldsymbol{P}_j - 3\boldsymbol{r}_{ij}(\boldsymbol{r}_{ij}\cdot\boldsymbol{P}_j)\right]}{r_{ij}^5} \tag{2.6}$$

where i = 1,2,…,N, j = 1,2,…, N, $j \neq i$, and $\boldsymbol{r}_{ij}$ is a vector from dipole i to dipole j. Notably, the first term in equation (2.6) is associated with radiative dipolar interactions between the nanoparticles, and exhibits a $1/r$ dependence on the distance between the nanoparticles. It is dominant over the second the third terms that have $1/r^2$ and $1/r^3$ dependences when the interparticle spacings are large [130]. To obtain the polarization vectors $\boldsymbol{P}_j$, $3N$ linear equations of the form $\boldsymbol{C}_{ij}\boldsymbol{P}_j = \boldsymbol{E}_i$ should be solved.

For the case when a normally incident plane wave excites an infinite array of identical nanoparticles with polarizability α_s (Fig. 2-2a), the retarded local electric field can be expressed as

$$\boldsymbol{E}_{loc,i} = \boldsymbol{E}_{inc,i} + \boldsymbol{E}_{dipole,i} = E_0 \exp(i\boldsymbol{k}\cdot\boldsymbol{r}_i) - \underbrace{\left(\sum_{\substack{j=1 \\ j\neq i}}^{N} \exp(i\boldsymbol{k}\cdot\boldsymbol{r}_{ij})\boldsymbol{C}_{ij} \right)}_{S} \alpha_s \boldsymbol{E}_{loc,i} \tag{2.7}$$

where S is the retarded dipole sum defined in the parentheses. By assuming the dipolar moment (induced polarization) of each nanoparticle is the same, i.e., $\boldsymbol{P}_j = \boldsymbol{P}_i = \alpha_s \boldsymbol{E}_{\mathrm{loc},i}$ (i = 1,2,…,N, j = 1,2,…, N), an effective polarizability α_{eff} of the constituent nanoparticles can be readily found.

$$\boldsymbol{P}_{eff,i} = \alpha_{eff}\boldsymbol{E}_{inc,i} = \frac{1}{1/\alpha_s - S} E_0 \exp(i\boldsymbol{k}\cdot\boldsymbol{r}_i) \tag{2.8}$$

The extinction and scattering cross-sections then can be calculated using

$$Q_{ext} = \frac{4\pi k}{E_0}\mathrm{Im}(P_{eff}) = \frac{4\pi k}{1/\alpha_s - S} \tag{2.9}$$

$$Q_{sca} = \frac{2k^4}{3|E_0|^2}|P_{eff}|^2 = \frac{2k^4}{3(1/\alpha_s - S)^2} \tag{2.10}$$

When the dimension of the nanoparticles is small relative to the wavelength of incident light, they can be approximated as oblate spheroids in the electrostatic limit, with permittivity calculated from a Lorentz-Drude model [111, 131]. Considering a homogeneous native oxide layer around each Al nanoparticle, the dipolar-polarizability α_d, as a function of frequency of incident light, can be expressed as

$$\alpha_d(\omega) = \frac{\pi d^2 h\left\{\left(\varepsilon_{ox}-\varepsilon_m\right)\left[\varepsilon_{ox}+\left(\varepsilon_{Al}-\varepsilon_{ox}\right)\left(L_i-L_o\right)\right]+f\varepsilon_{ox}\left(\varepsilon_{Al}-\varepsilon_{ox}\right)\right\}}{6\left\{\left[\varepsilon_{ox}+\left(\varepsilon_{Al}-\varepsilon_{ox}\right)\left(L_i-fL_o\right)\right]\left[\varepsilon_m+\left(\varepsilon_{ox}-\varepsilon_m\right)L_o\right]+fL_o\varepsilon_{ox}\left(\varepsilon_{Al}-\varepsilon_{ox}\right)\right\}} \quad (2.11)$$

where ε_m, ε_{Al}, and ε_{ox} are the permittivities of the embedding medium, aluminum, and aluminum oxide, respectively. Here the permittivity of the embedding medium is the averaged value of superstrate and substrate surrounding the Al nanoparticles. Moreover, h is the height of the oxidized nanoparticle. L_i and L_o are the geometric factors of the inner (only aluminum core) and outer (aluminum core plus aluminum oxide shell) spheroid, respectively. This geometric factor is determined by the ratio of the major axis (corresponding to the diameter of the nanoparticle D) and the minor axis (corresponding to the height of the nanoparticle h). The factor f is the fraction of the total nanoparticle volume occupied by the inner spheroid. In order to account for the radiative damping and dynamic depolarization (the retardation across the nanoparticle), a modified long wavelength approximation (MLWA) is used to correct the quasi-static approximation [132, 133].

$$\alpha_s(\omega) = \alpha_d(\omega)\left[1 - i\frac{k^3}{6\pi}\alpha_d(\omega) - \frac{k^2}{2\pi D}\alpha_d(\omega)\right]^{-1} \quad (2.12)$$

We see that the effective polarizability α_{eff} of the nanoparticles is controlled by the dipole sum S, which depends on array parameters (the period, size of a particle, etc.). The modulus of α_{eff} is maximized when the real parts of $1/\alpha_s$ and S are equal in equation (2.8), giving rise to a sharp peak in the extinction and scattering spectra according to equations (2.9) and (2.10). Under this resonance condition, the scattered radiation fields, the diffracted incident light in the plane of the nanoparticle array, arrive in-phase with the incident light field. This in-phase interaction further translates into the in-phase coherent coupling between the scattered fields by each nanoparticle and the incident light induced LSPR of its nearest neighbors, reinforcing the plasmon resonance of individual nanoparticles. Such diffractively coupled LSPRs (or also named collective plasmonic resonances), is to some degree analogous to the condition of LSPR excitation in a typical nanoparticle (which occurs when the real part of the denominator describing the polarization of a nanoparticle vanishes [134]). Essentially, these collective plasmonic resonances are a superposition of the eigenmodes of individual uncoupled nanoparticles that exhibit a standing-wave character delocalized across the entire nanoparticle ensemble [135].

2.5.2 Preliminary Optimization of Design Parameters

Here, we employ the CDA based coarse model for the preliminary optimization of the design of ANAs that yields a far-field extinction peak at the desired wavelength 405 nm and a remarkably narrow resonance linewidth that is less than 15 nm. The structure considered here is consists of a square-lattice periodic array of aluminum nanodisks

fabricated on a fused silica substrate in a water environment, as illustrated by Fig. 2-2a. In the ANA geometry, the height (h) and oxide layer thickness (t_{ox}) of Al nanodisks are fixed to be 30 nm and 3 nm, respectively. And the radius of the nanodisk (r) and lattice periodicity (P) are varied to tailor the diffractive couplings among the nanodisks.

Tuning of the individual nanodisk LSPRs to a specific incident wavelength by altering the disk size (r) leads to a strong enhancement in the collective response. The most pronounced collective plasmonic resonance in the nanodisk array can be expected to occur at a wavelength near the plasmon resonance of an isolated particle [111]. According to previous work [122, 131], a single Al nanodisk with 80 nm diameter yields an extinction peak around 405 nm. Thus, the optimized nanodisk array with an LSPR at 405 nm can be expected to take on r close to this value 80 nm. On the other hand, tuning of the lattice periodicity P adjusts the accumulative phase delays (the second component in equation (2.7)) experienced by the long-range dipolar interactions among the nanodisks. At a critical lattice periodicity P_c, the scattered fields impinging on individual nanodisks all add in phase at a specific wavelength λ_c when $\boldsymbol{kr}_{ij} = 2\pi m$ (m is an integer), countering the radiative damping of individual nanodisk responses and leading to the emergence of a new grating order (i,j). At this transition wavelength λ_c, the radiative diffracted grating orders are transformed into an evanescent character, resulting in the suppression of the inherent radiative damping in nanodisks and a remarkable narrowing of the resonance linewidth. This transition wavelength λ_c is closely associated to the critical lattice periodicity through an empirical mathematical relation

$$P_c \approx \frac{\sqrt{i^2 + j^2}}{n_s} \lambda_c \tag{2.13}$$

where n_s is the refractive index of the fused-silica substrate and (i,j) are the diffraction orders. Here $\lambda_{c,(1,0)}$ is the critical wavelength below (above) which the (1,0) diffraction order that is aligned with the electric field direction of the incident light of the fused silica interface becomes radiative (evanescent) at a given lattice periodicity ($\lambda_{c,(1,0)} = n_s d$). When the critical wavelength $\lambda_{c,(1,0)}$ is the target far-field extinction peak wavelength 405 nm, the transition lattice periodicity d_c is found to be $P_c \approx 276$ nm according equation (2.13).

Based on the above empirical guess for the parameters disk radius r and lattice periodicity P to respectively satisfy the device performance constraint (maximizing the far-field extinction at 405 nm), the inverse design problem can be reduced to a small parameter space (r, P) by choosing relevant ranges for r and P around 80 nm and 276 nm, respectively. Due to the formation of the native oxide layer, we take into account the fabrication constraint (nanoparticle size) in this inverse design problem in order to yield experimentally feasible and geometrically homogeneous structures [122]. Here, we judiciously select a narrow parameter space for ANAs design optimization, i.e, varying the disk radius r from 20 nm to 60 nm and lattice periodicity P from 200 nm to 300 nm both at a step of 1nm, respectively. All possible combinations of these two parameters are used as inputs for the calculation of the extinction spectrum of the ANAs. According to equation (2.9), the extinction spectrum of the diffractively-coupled array can be estimated once the polarizability of individual nanodisks α_{eff} is known, which is

the essence of CDA employed in this work. The modulus of α_{eff} is maximized when the real part of the denominator in equation (2.9) vanishes, giving rise to a sharp peak in extinction spectrum. Hence, one can look for the array structure with the right combinations of r and P which yield an extinction peak at the desired wavelength 405 nm by tracking the spectral behavior of the right-hand side components in equation (2.10). Computation of retarded dipole sum S involves evaluating an infinite summation terminated at $N = 1800$ nanodisks. For the embedding medium, an effective refractive index ($n_{\text{eff}} = 1.40$) is used for calculating the dipolar-polarizability α_{p} using the equation (2.11), by averaging the values of water superstrate (1.33) and the fused silica substrate (1.47).

Fig. 2-2b plots a 2D heat map for the variation of the wavelength at which the real parts of S and $1/\alpha_{\text{s}}$ intersect with respect to all different combinations of r and P values. A black solid curve marked as $\lambda_{\text{zc}} = 405$ nm denotes the particular combinations of parameters where the deviation of the intersection wavelength from 405 nm is zero. This single line can be utilized to narrow down the search for optimal parameters, which we term as the zero-crossing (ZC) curve. As long as the assumed n_{eff} provides a good substitute of a realistic system for which an extinction peak position is calculated through high-fidelity fine model evaluations, the ANAs can be expected to be optimized at a point on or close to this ZC curve. To satisfy the second design specification, i.e., a narrow resonance linewidth no larger than 15 nm, we evaluate the full-width half-maximum of the extinction spectra for all the combinations of r and P parameters on the ZC curve. It is found that this particular combination $r = 34$ nm, $P =$

284 nm yields the minimum linewidth at approximately 11 nm, denoted by a white square in Fig. 2-2b. Fig. 2-2c summarizes the real and imaginary parts of the retarded dipole sum S and inverse of the nanodisk polarizability $1/\alpha_s$ for the particular ANA structure. The real part of the dipole sum Re(S) diverges at the critical wavelength $\lambda_{c,(1,0)} = 395$ nm (diffraction edge), indicated by the vertical dashed line. At this diffraction edge, the imaginary part Im(S) of the lattice sum changes its sign abruptly (blue dashed curve). The grating order is evanescent (radiative) when the Im(S) is negative (radiative), resulting in decreased (increased) radiative damping. Cancellation of the real terms in the denominator in equation (2.9) results in a single and extremely narrow Fano-type extinction resonance, as shown by the vertical dashed line and red curve in Fig. 2-2d. Similarly, partial cancellation of the imaginary terms results in resonance linewidth narrowing of the far-field extinction spectrum due to suppressed radiative damping. As shown by Fig. 2-2d, when the grating order is evanescent, the nanodisk array exhibits optical responses (red curve) dramatically different from those of an isolated nanodisk (blue curve). A key feature of the extinction spectrum of the nanodisk array is the strong asymmetry in the spectral line shape and sharp dip near the diffraction edge. This Fano-type asymmetric spectral response is a result of the interference of the broad nanodisk LSPR and the narrow linewidth at the Rayleigh anomaly resonance ($\lambda_R = n_{eff}P$) [128, 136, 137]. We find that the array exhibits a nearly 10-fold improvement in the resonance linewidth with respect to that of the isolated Al nanodisk. This improvement originates from the partial cancellation of the radiative damping by the diffractive coupling. The optical energy scattered by each nanodisk can

be efficiently collected by its neighbors as plasmons rather than decaying to continuum. Linewidth narrowing is also associated to increased plasmon lifetimes and near-field enhancements [111].

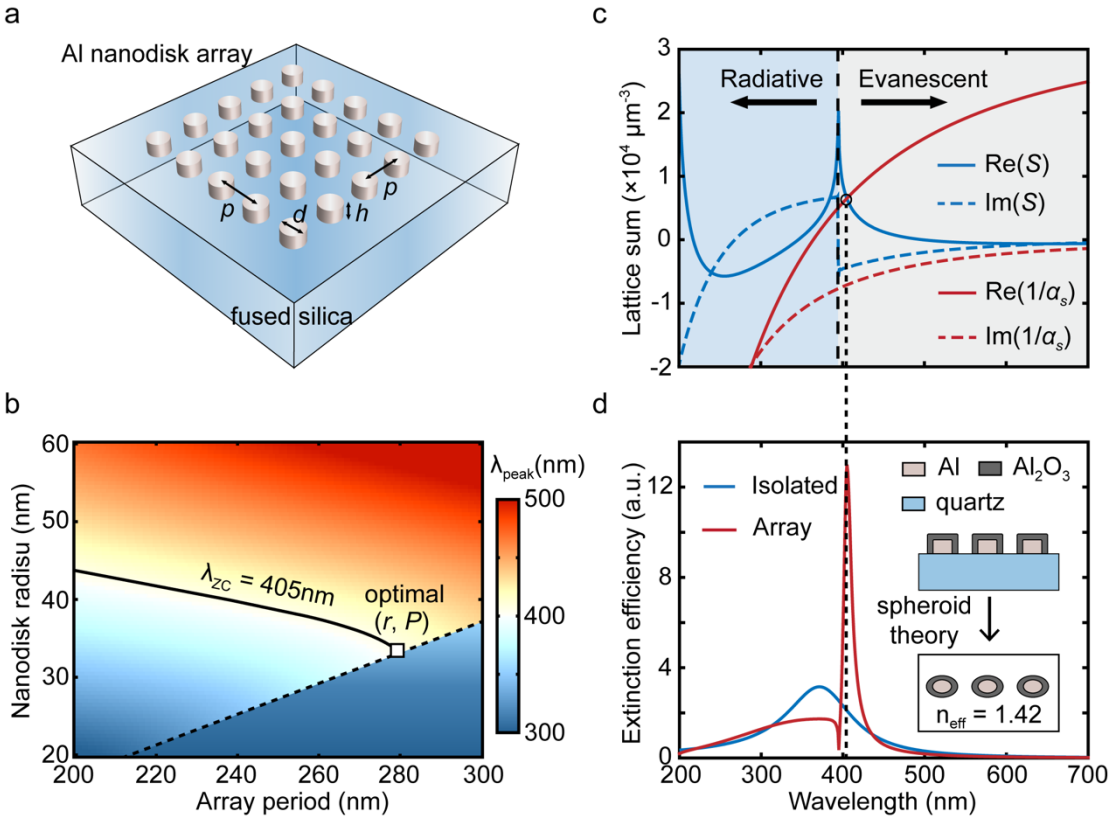

Figure 2-2. Optimized Al nanodisk array with extinction resonance wavelength at 405 nm and 10 nm resonance linewidth using a CDA model. (a) A 3D schematic view of Al nanodisk array. (b) A heat map showing the relative peak extinction cross-section values for a range of nanodisk radii *r* and array periodicities *p*. The solid tilted curved, the zero-crossing curve, denotes the range of design parameters where the deviation of the intersection wavelength from 405 nm is zero. (b) Retarded lattice sum (*S*) and nanodisk polarizability (α_s) as a function of incident light wavelength for the optimized design (indicated by the square in (b)) satisfying the pre-defined specifications. (d) The

extinction spectrum of the optimized design of Al nanodisk array (red solid curve) is compared to that of an isolated Al nanodisk (blue dashed curve).

2.5.3 Fine Model Evaluation

With the optimized coarse model with parameters r = 34 nm, P = 284 nm, we further investigate whether the optimized parameter set is sufficient to meet all the design specifications. Hence, we proceed to the 3rd stage of the SM optimization process by evaluating the fine model response at this particular design parameter set (34 nm, 284 nm), as shown by the flow chart (Fig. 2-3a). The high-fidelity fine model chosen here is a finite-difference frequency-domain (FDTD) based rigorous full-wave electromagnetic simulation, which is conducted using the commercial Lumerical software – FDTD Solutions. FDTD Solutions is the gold-standard for modeling nanophotonic and nanoplasmonic devices and a wealth of different materials [130]. It is a high-performance and powerful electromagnetic solver accurately and reliably capturing the optical properties of wavelength-scale arbitrary metal structures. FDTD Solutions takes into account the "lossy" nature of metals at optical frequencies by directly incorporating experimentally measured wavelength-dependent permittivity of the metals, including the real and imaginary parts, into the simulations without any approximations. Essentially, the fine FDTD model accurately describes the optical performance of the given ANA device as it provides an exact solution of the Maxwell's equations.

We consider ANAs fabricated on a fused-silica substrate with a refractive index of n_s = 1.47 in an aqueous environment with n_w = 1.33. Al nanodisks are covered by an oxide (Al_2O_3) layer with a refractive index of n_o=1.78 on the water side. The complex dielectric response of Al is represented by Palik's data for relative dielectric permittivity [138]. The height of all nanodisks is fixed to h = 30 nm, whereas the oxide layer thickness is adopted as t_{ox} = 3 nm, which is a generally-accepted value [101, 131], in all calculations. Moreover, peripheries of the top faces of Al nanodisks and surrounding oxide layers are filleted with a radius of curvature of 2 nm to realistically represent experimentally-accessible samples.

In our FDTD simulations of the far-field extinction spectra of the ANA device, an adaptive meshing scheme with a minimum grid size of 1 nm is adopted to ensure the convergence of the numerical results. Bloch-Floquet periodic boundary conditions are applied normal to the plane of periodicity for the nanodisk arrays, while the rest of the computational domain is terminated by a pair of perfectly-matched layer (PML) absorbing boundaries. A total-field scattered-field source (TFSF) propagating along the z axis with electric field being polarized along the x axis is employed to excite the plasmonic resonance of Al nanodisks from the water side and measure the scattered field on the fused silica side and absorbed field by the Al nanodisks. Unlike a plane wave source, the TFSF source type effectively separates the computation region into two distinct regions – one contains the total field (i.e. the sum of the incident field and the scattered field), while the second region contains only the scattered field. The width of the optical pulse, i.e. $\Delta t \approx 2$ fs is such that its Fourier transform covers the whole

frequency (wavelength) ranges of interest. To ensure the optical pulse passes through the entire simulation domain completely, a simulation time of $t \approx 1000$ fs is used. Besides, a time step of $dt \approx 2$ ps is adopted in all FDTD simulations to satisfy Courant-Friedrichs-Lewy stability criterion. Far field extinction spectra are obtained by probing the transmittance minimum in the substrate region. Field enhancements are obtained by probing E-field strength at different z-planes crossing the fused silica-nanodisk interface, top of the pure Al nanodisk and the oxide layer.

The extinction response for the CDA optimized structure parameters is calculated using FDTD simulations at a discrete set of wavelengths (350 nm $< \lambda <$ 500 nm). As shown by Fig. 2-3b, we observe that the extinction peak of the nanodisk array structure obtained with the FDTD-based fine model (420 nm, blue curve) is substantially different from the CDA model peak (405 nm, black curve), and does not satisfy the desired specification indicated by the vertical dashed line. In the context of a generic space mapping algorithm, this response difference is translated into a severe "misalignment" between the two models. There should be no misalignment in between these two models once converged. However, the more the functional behaviors of the two models differ from each other, the more the misalignment increases [139]. Therefore, simply optimizing the CDA-based coarse model is not sufficient to obtain a nanodisk array structure that meets the design requirements.

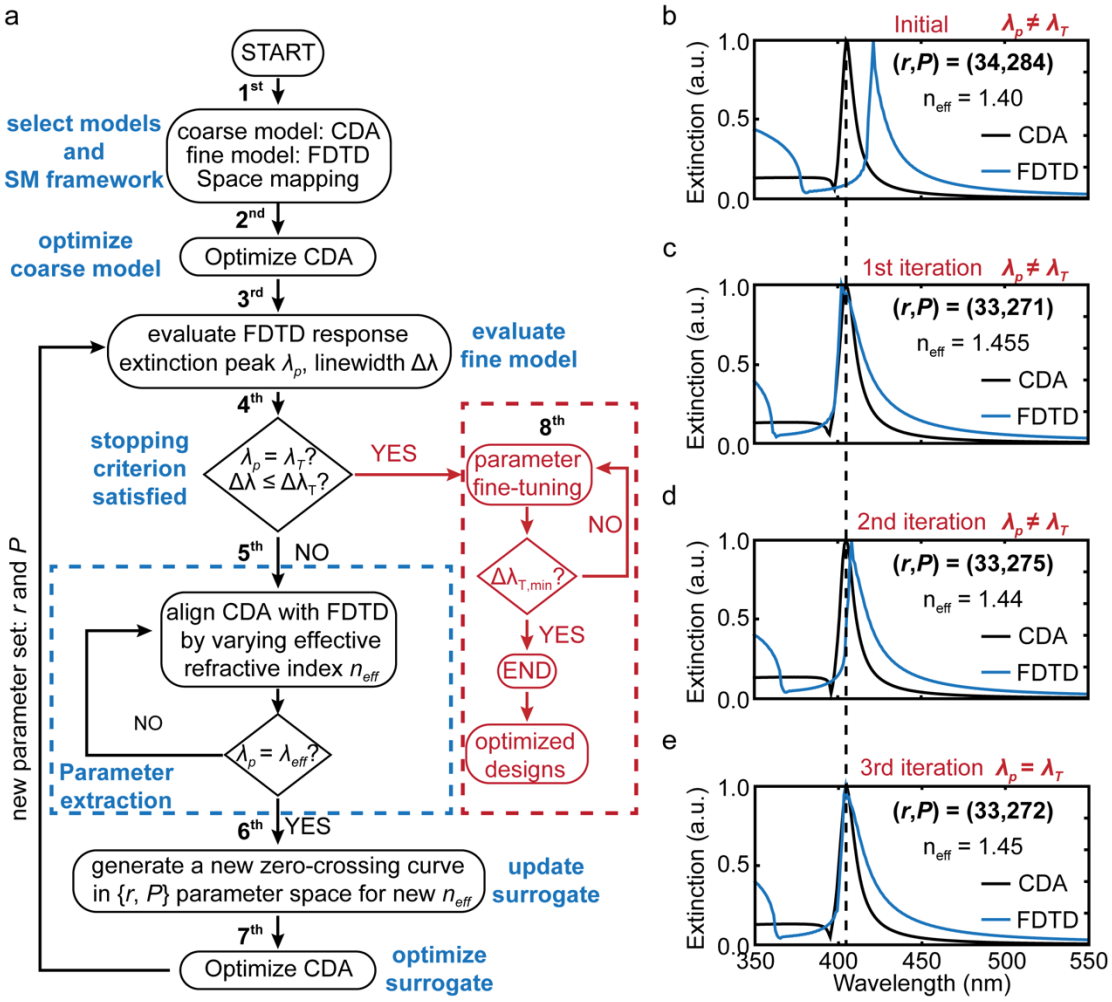

Figure 2-3. Implementation of the space mapping algorithm. (a) Flow chart for the space mapping process. (b) Extinction response of the nanoantenna array structure calculated with CDA (black) and FDTD (blue) for parameters obtained after the n^{th} iteration of the space mapping algorithm. Vertical black dashed line is the specification defined for this structure.

2.5.4 Parameter Extraction and Surrogate Update and Optimization

The misalignment problem can be addressed by employing a parameter extraction (PE) strategy that enables effective realignment of two models with substantially different functional behaviors. Conceptually, this technique is carried out by first establishing a one-to-one mapping between the parameter spaces, and then continuously updating the relatively computationally-efficient coarse model until its response matches with the computationally-expensive fine model for the same set of parameters. The last updated coarse model is then optimized to predict new sets of parameters for the next iteration of the SM algorithm. The process of evaluation, parameter extraction, and reproduction is repeated until all the design specifications are reached. Notably, the uniqueness of the parameter extraction is crucial to the success of SM optimization.

In our proposed SM optimization algorithm, the parameter extraction is executed in the 5^{th} stage right after the 4^{th} stage - design criterion evaluation, as outlined by the blue dashed rectangular box in Fig. 2-3a. We mathematically link the parameter spaces of the CDA and FDTD models through fine-tuning of the effective refractive index n_{eff} of the embedding medium surrounding the nanodisks in the CDA model. It should be noted that the FDTD model is unvaried during the PE process, and its extinction peak for the current set of parameters (r, P) = (34 nm, 284 nm) is used as the benchmark (420 nm, blue curve in Fig. 2-3b) for the coarse model alignment. Our PE procedure uses an objective function that minimizes the error at a particular wavelength (405 nm),

defined as the difference between the extinction responses calculated with the CDA and FDTD based models. The parameter extraction procedure is terminated when the error falls below a certain threshold, i.e., 0.1 nm.

From the initial step of the SM algorithm, we find the last updated n_{eff} to be 1.455 and use it to update the CDA-based coarse model as a surrogate. A new ZC curve with the same r and P ranges defined earlier in Fig. 2-2b is calculated with the surrogate coarse model, subsequently followed by the optimization of the surrogate to satisfy the linewidth specification. The obtained new set of parameters (r, P) = (33 nm, 271 nm) is then evaluated through FDTD-based fine model again as the 1st iteration of the SM optimization. The device response obtained with FDTD after the 1st iteration nearly satisfies the specifications (Fig. 2-3c). The n_{eff} is further fine-tuned to 1.44 and then the 2nd iterative process is proceeded. It is found that the extinction resonance linewidth reaches the design requirement ($\Delta\lambda \leq 15$nm) although the extinction peak wavelength deviates from 405 nm to some extent (Fig. 2-3d). Finally, after the 3rd iteration the extinction response of the device calculated with the FDTD fine model satisfies all the specifications completely, as shown in Fig. 2-3e.

It is evident that the CDA-based coarse model possesses two essential features that are responsible for assuring rapid convergence to the optimal design: (i) it is extremely computationally fast; (ii) it is sufficiently faithful and exhibits excellent alignment capability with respective to the high-fidelity computationally expensive fine model. Thus, the optimized solution satisfying all the design specifications rapidly emerges after only 3 iterations. In other words, full-wave electromagnetic (high-fidelity)

simulations of only 3 candidate structures are required before the iterative process is terminated. It is the one-to-one mapping that enables the rapid convergence to the desired design after a few iterative SM processes. Use of the SM approach offers a substantial reduction of enormous design space to a compact set of candidate structures. This approach minimizes the number of high-fidelity and computationally expensive model evaluations and enables a fast and self-consistent convergence to the optimal design parameter set that meets all pre-defined specifications. As a result, significantly less computation time is required to accurately extract the parameters with respect to any direct optimization method using the fine model alone.

2.5.5 Parameter Fine-Tuning

To examine whether the above optimized structures have already yielded the best possible device performance, i.e., highest quality-factor (or minimal resonance linewidth), we computed and analyzed the extinction spectra of the ANA with all potentially optimal (r, P) design parameters along the last updated ZC curve. This particular procedure is initiated in the 8th stage of the SM optimization when the user-defined design specifications are satisfied (Fig. 2-3a). Fig. 2-4a depicts the ZC curve for n_{eff} = 1.45 obtained in the 3rd iteration loop of the SM algorithm. Without loss of generality, we particularly select a set of 10 representative (r, P) parameters denoted as diamond-shape points (P1, …, P10) along the ZC curve, and three additional points (P11, P12, P13) away from the ZC curve for comparison purposes. We purposely choose the parameter set-P10 right at intersection of ZC curve and radiative/evanescent

coupling boundary (black dashed line). Fig. 2-4c and Fig. 2-4d summarize the computed extinction spectra for the ANAs with these 13 different sets of parameters through CDA calculations and FDTD simulations. The values of these 13 sets of parameters are denoted in the format of (r, P) with units in nm, as shown on the right-hand side of Fig. 2-4c. It is evident that the extinction maxima ($\Delta\lambda_p$) calculated with the CDA model are all equal to 405 nm (indicated by a vertical dashed line) for the first ten parameter sets P1-P10 (Fig. 2-4b). In contrast, a monotonic increase in the extinction maxima obtained with FDTD model is observed for the same parameter sets (Fig. 2-4c). One common feature of the CDA and FDTD results is the monotonic linewidth suppression along the ZC curve from P1 to P10. As shown by Fig. 2-4c and Fig. 2-4d, the sharpest peak is found for the parameter set P10 with linewidths of 8 nm and 10 nm corresponding to the CDA and FDTD computed extinction spectra, respectively. However, for this parameter set P10, the extinction maximum calculated with the FDTD model appears at around 407 nm, a value slightly larger than the desired one λ_T = 405 nm (Fig. 2-4d). Nevertheless, the peak extinction wavelength becomes exactly 405 nm for the neighboring parameter set P9 despite the fact that the corresponding resonance linewidth broadens to 14 nm (Fig. 2-4d). Compared to the structure that is optimized after 3 iterations of the execution of SM algorithm (blue curve in Fig. 2-2e), there is a slight improvement in the resonance linewidth: a narrowing from 15 nm down to 14 nm. Thus, it is necessary to incorporate the parameter fine-tuning procedure into the SM algorithm in order to find the fittest parameter sets that achieve maximum device performance. On the other hand, for the

remaining three parameter sets P11, P12, and P13, the corresponding extinction spectra calculated with CDA and FDTD models show significantly diminished extinction efficiencies (Fig. 2-4c and Fig. 2-4d). Compared to the parameter sets on the ZC curve, the grating orders of the nanodisk arrays with the three parameter set transitions from evanescent (top panel of Fig. 2-4b) to radiative (bottom panel of Fig. 2-4b) in character, causing increased radiative damping and a broadening of the linewidth. Therefore, SM algorithm offers the possibility to tailor the resonance linewidths in addition to the resonance spectral positions.

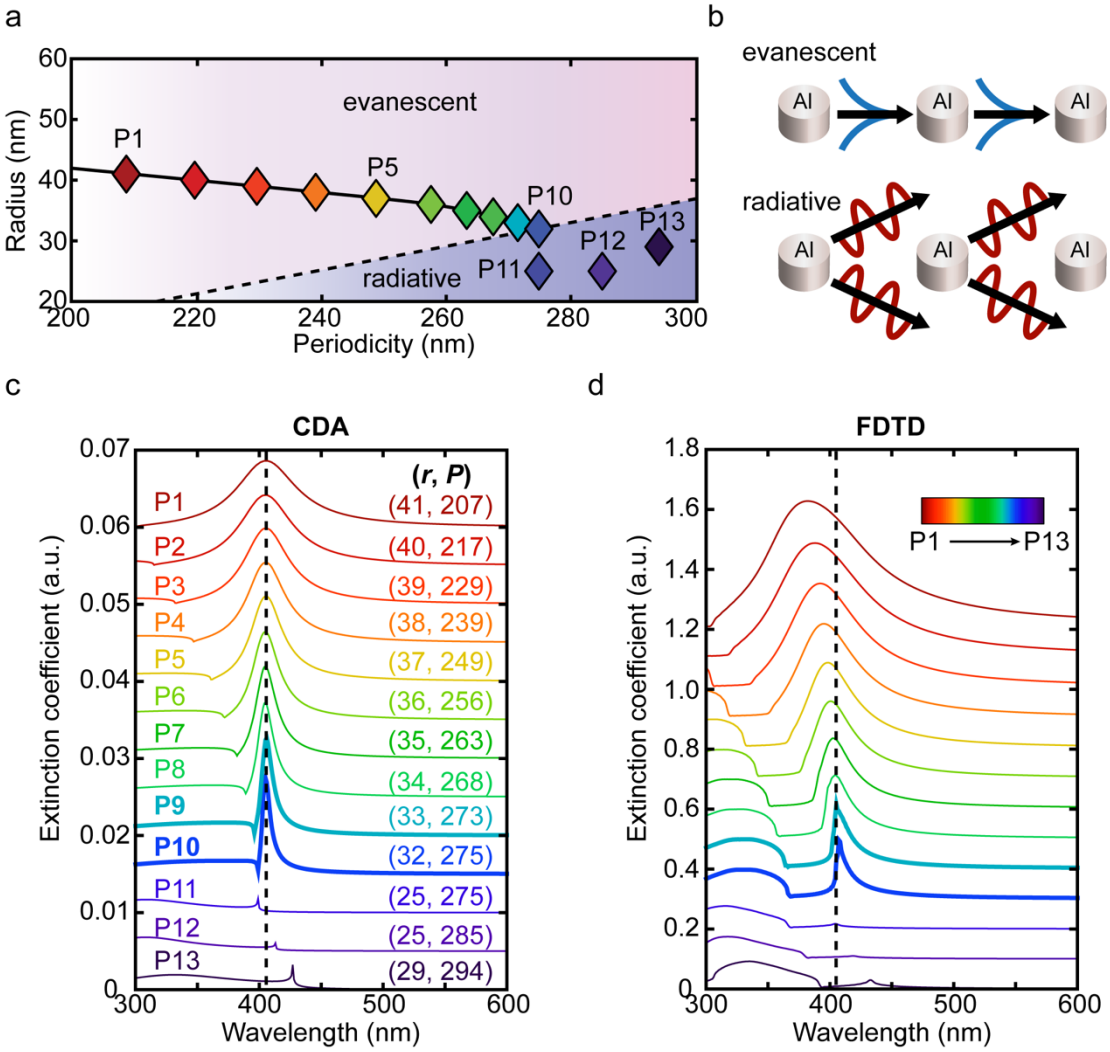

Figure 2-4. Fine tuning of the parameters to examine the remaining design specifications. (a) Selection of discrete points close to the ZC line for 405 nm. The dashed line indicates the wavelength at which the grating order transitions from evanescent to radiative in character. (b) Schematic of the evanescent to radiative characters of the grating order. The extinction spectra corresponding to the selected parameter sets are obtained with (c) CDA and (d) FDTD methods. The vertical dashed line in (c-d) denotes 405 nm.

2.6 Experimental Validation

To demonstrate the accuracy of the SM-based inverse design approach, the fittest parameter set, (r, P) = (33 nm, 273 nm), was selected for experimental fabrication and characterization. Devices with this parameter set were fabricated on 200 mm diameter fused-silica substrates using wafer-scale UV interference lithography and etching of sputter-coated Aluminum films [140]. Periodicity was controlled by varying the angle of incidence of the interfering beams with respect to the surface normal of the substrate, while the nanodisk diameter was controlled via exposure dose and etch processing. The Al nanodisk height was controlled by modifying the sputter deposition time of the Aluminum film, where the thickness was calculated from sheet resistance. The fabricated devices were cleaned in an ultrasonic bath in methanol to remove etch residues. To help optimize fabrication parameters, the optical transmittance of the fabricated structures was monitored at the wafer-scale and compared to nanodisk array modeling in air. A scanning electron microscopy (SEM) image of a fabricated device is shown in Fig. 2-5a, where the SM-optimized design was accurately reproduced by the lithographic process with minimal imperfections. As shown by Fig. 2-5b, the extinction spectrum of the optimized ANA calculated using FDTD (blue curve) shows excellent agreement with the experimental measurement using a standard UV/visible/near infrared (NIR) spectrometer with a spectral bandwidth of 2 nm at normal incidence and polarized light parallel to <10> direction (red curve). The experimentally measured extinction peak wavelength and resonance linewidth are approximately 404 nm and 15 nm, respectively. A slight deviation in the resonance

wavelength is likely due to remaining etch residues that tend to blue shift the plasmon resonance. The observed extinction resonance is associated with the strongly enhanced near-field light intensity in the nanodisk arrays. The inset in Fig. 2-5b presents the electromagnetic (EM) intensity distributions around individual nanodisks over two orthogonal cross-sections (*xy*, *xz*). The EM field energy is found to be highly concentrated around the rims of the air-nanodisk and quartz-nanodisk interfaces. Due to the asymmetric dielectric environment surrounding the nanodisk, the EM field energy concentrates more into the quartz-nanodisk interface that exhibits a relatively high refractive index. This physical phenomenon can be well understood by using an electrical circuit analogy approach. In this approach, we treat the incident light and nanodisk as a current source and flux, respectively, and model the refractive index of the surrounding dielectric environment as an electrical impedance of a two-terminal circuit element that is driven by the current source (Fig. 2-5c). Using this circuit analogy, more (less) flux flow is expected when the electrical impedance is low (high). Thus, the modeled electrical impedance scales as the inverse of the refractive index ($1/n$) of the surrounding dielectric environment. In the case of the nanodisk array being embedded in an asymmetric substrate-superstrate surrounding, the current flows over their modeled circuit counterparts would be asymmetric due to the difference in their electrical impedances (Fig. 2-5c). Therefore, the radiative field flux established around the nanodisk would be asymmetric as well, with higher (lower) field flux in higher (lower) refractive index medium, as confirmed by the FDTD calculations (Fig. 2-5d).

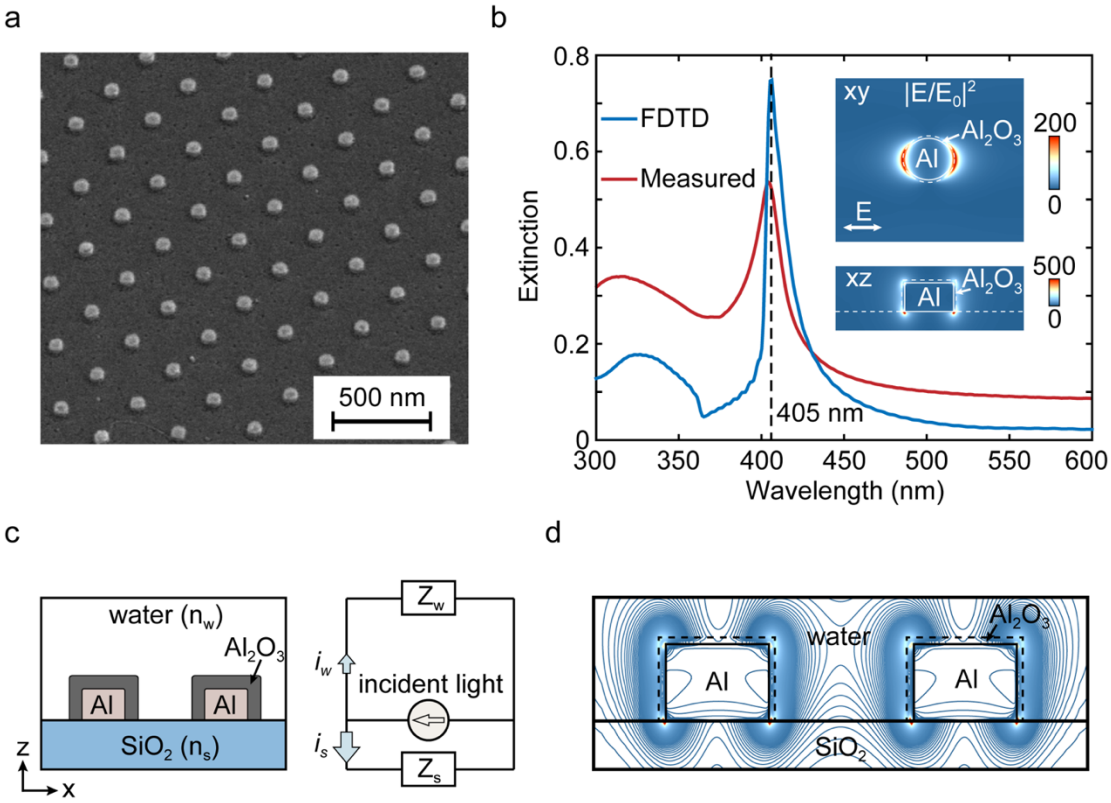

Figure 2-5. (a) A scanning electron microscopy (SEM) micrograph of a final fabricated device at the optimized parameter set. (b) FDTD-modeled extinction spectrum of the optimized Al nanodisk array (solid blue curve) agrees excellently with the experimental measurement (solid red curve). The vertical dashed line represents 405 nm. Inset depicts E-field distribution at 405 nm over two orthogonal cross sections. (c) A circuit model is employed to describe the observed field-enhancement patterns (d) Distribution of E-field lines in the optimized Al nanodisk array.

2.7 Photo-Induced Heating of Aluminum Nanodisk Arrays (ANAs)

2.7.1 Enhanced Heat Generation

The radiative damping in a single nanodisk is responsible for the far-field energy radiation (Fig. 2-6a), which broadens the plasmon resonance, shortens the plasmon lifetime, and limits the near-field enhancement [122, 141]. In addition to the radiative damping, the nonradiative damping through electron-hole pair decay is also present but negligible as the plasmon resonance energy (> 3 eV) is much higher than the interband absorption threshold of aluminum [122]. Collective excitation of the plasmons resonances in the aluminum nanodisk arrays (ANAs) leads to suppressed radiative damping (Fig. 2-6b), which significantly reduces the energy losses due to photon emission. Fig. 2-6c and Fig. 2-6d present the FDTD simulated optical and thermal responses of an individual nanodisk and a single nanodisk in an ANA at 405 nm, respectively. In both scenarios due to the nature of LSPRs, the enhanced electric fields are mainly concentrated at the edges of the nanodisks. ANAs show prominent improvement in near-field enhancement with respect to isolated nanodisks; peak enhancement in near-field intensity is five times stronger. This improvement is associated with the strong diffractive couplings within the array, which allows incident light to be efficiently coupled into much stronger near-field excitations rather than radiatingto the optical far field. Since the optical absorption by the nanodisk is

proportional to the square of the total electric field amplitude, it is expected that more heat is generated by an individual nanodisc in an ANA as opposed to an isolated single nanodisk. This prediction is confirmed using thermal simulations, as shown by rightmost panels of Fig. 2-6c and Fig. 2-6d. The ANAs produce a temperature increase of 79 °C (rightmost panel of Fig. 2-6d), whereas the temperature change relative to the surrounding environment is nearly negligible for an isolated single nanodisk (rightmost panel of Fig. 2-6c). This substantial improvement in heat generation implies that the absorption cross section of an individual nanodisk in a ANA is remarkably larger due to the suppressed radiative damping.

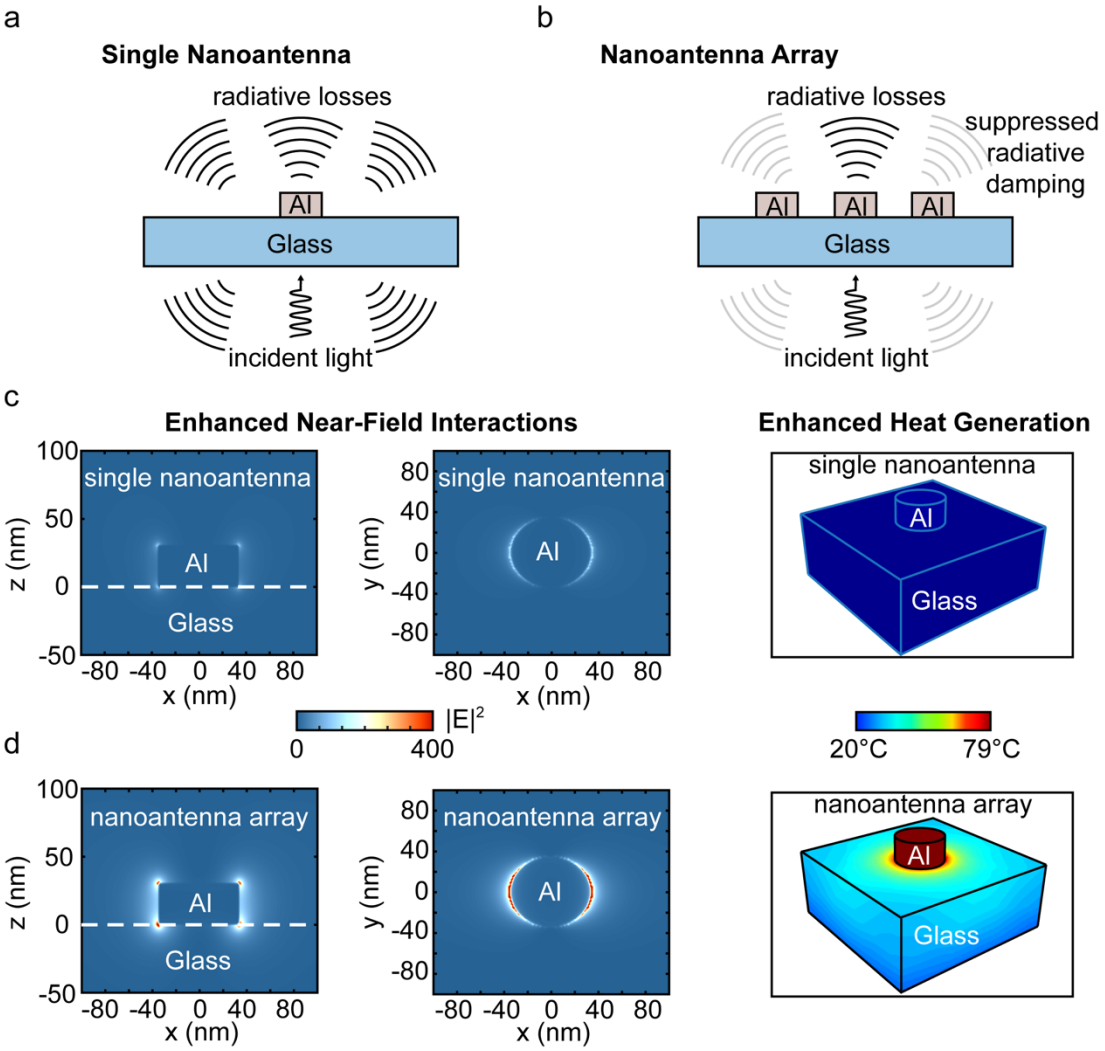

Figure 2-6. Suppression of radiative damping. (a) A single aluminum nanodisk excited by normally incident light experiences radiative damping caused by far-field photon emission (b) The radiative damping is significantly suppressed in ANAs as the near-field coupling among the dipolar fields of the optically excited nanodisks is enhanced. Cross-sections of the intensity distributions in the XY and XZ planes and three-dimensional simulated temperature distributions are shown for (c) an isolated single

nanodisk (radius 33 nm, height 30 nm) and (d) an individual nanodisc in ANA (radius 33 nm, height 30 nm, array period 273 nm), respectively.

2.7.2 Experimental Temperature Distribution Measured on a Monolithically Patterned Aluminum Nanodisk Arrays

The heat generation by an optimized ANAs with 405 nm light illumination was experimentally characterized using a thermal imaging camera (FLIR Systems, Inc) with a high resolution thermal sensor. The ANAs coated glass slide was immersed in an aqueous environment (water) and then mounted on a custom made platform for the temperature measurements. A high-intensity narrow-spectrum (HINS) 405 nm Solis™ LED system (Thorlabs, Inc., Newton, NJ, USA) consisting of an array of 12 individual LEDs in a matrix was placed at a distance of approximately 3 cm underneath the ANA coated glass slide. The ANAs coated glass slide was illuminated at an irradiance of 0.25 W/cm^2 for 60 min and the temperature of the illuminated region was measured every 2 min. This temperature measurement was repeated three times with three freshly fabricated ANA coated glass slides, and the time dependent absolute temperature was plotted in Fig. 2-7. All slides showed similar plasmonic heating behavior with rapid temperature rise during the initial light exposure and then temperature stabilization after 45 min exposure. To verify the heating occurring through the collective plasmon resonance, the same temperature measurement was repeated on a normal microscopic glass slide without any coated ANAs. There was only a slight temperature increase due to absorption in the glass and the temperature quickly stabilizes after 20 min exposure

(blue curve in Fig. 2-7). It should be noted that the infrared thermometer used in the above experiments is not capable of probing the temperature at the surface of the ANAs because the emission of light at infrared wavelength (~8 μm) attenuates exponentially due to water absorption. In addition, the diffraction limit of excitation source makes it extremely difficult or even impossible to probe the temperature at the nanoscale (e.g. sub-micon). These limitations explain the two-fold temperature difference between the FDTD simulation (Fig. 2-6d) and experimental result (red curve in Fig. 2-7). Nevertheless, the measured temperature 46 °C at steady-state is already sufficiently high to achieve at least 3 $\log_{10}$ (>99.9%) of inactivation of *Vibrio cholerae* within 30 min of heat exposure [142].

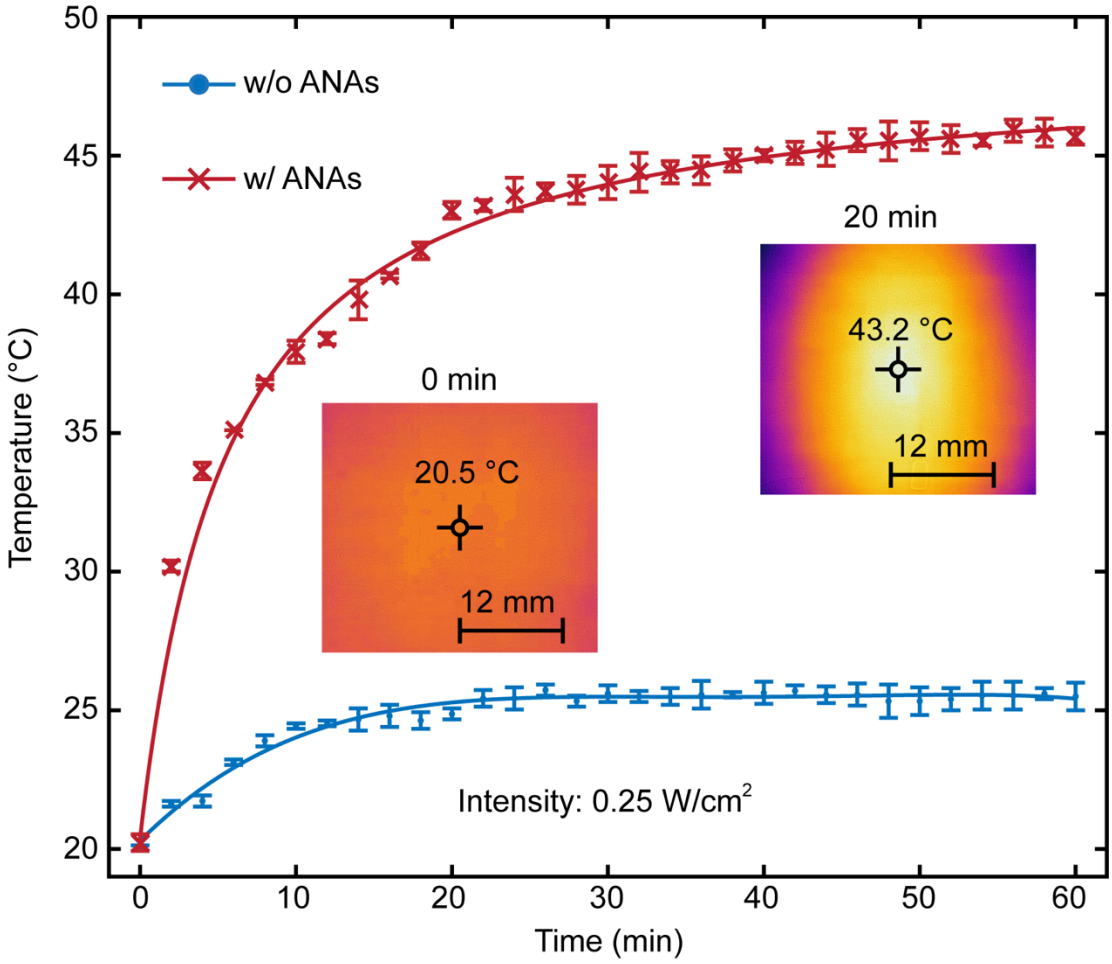

Figure 2-7. Temperature measurements of 405 nm LED illuminated glass slide coated with the ANAs (red curve) of the fittest design parameter set (r, P) = (33 nm, 273 nm) and normal glass slide (blue curve). Error bars are formed by three independent experimental measurements.

Temperature measurements of ANA coated and normal glass slides with irradiances ranging from 0 to 0.25 W/cm^2 for 20 min were performed using the same thermal probing methodology and setup described in Fig. 2-7. The resulting temperature rise as a function of irradiance of incident light is displayed in Fig. 2-8. A linear relationship

between temperature rise and irradiance is both observed on ANAs coated and normal glass slides as the power of heat generation is directly proportional to the irradiance of the incident light [143].

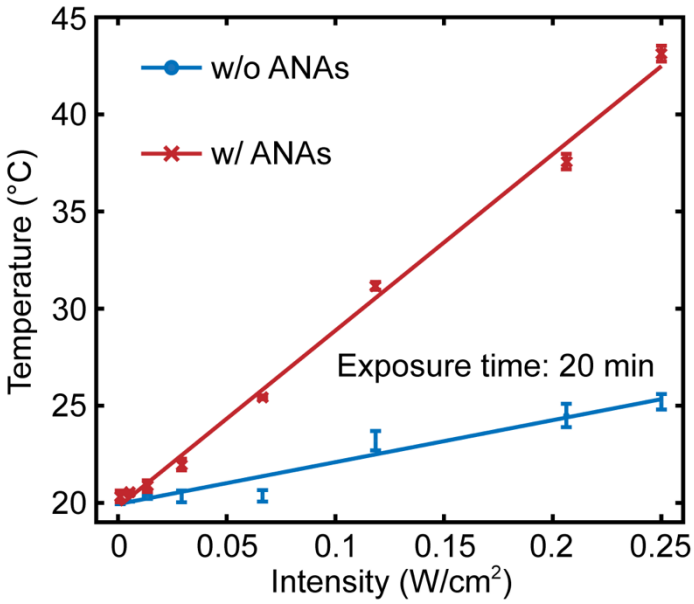

Figure 2-8. Temperature measurements of 405 nm LED illuminated ANAs coated (red line) and normal (blue line) glass slides versus irradiance of incident light. The light exposure time was fixed at 20 min and the temperatures of the slides were probed using an infrared thermometer (FLIR One, FLIR® Systems, Inc). Error bars are formed by three independent experimental measurements.

2.8 405nm Photo-Sterilization of Drug Resistant *Vibrio Cholerae* Biofilm on Aluminum Nanodisk Arrays (ANAs) by Visible 405 nm Light

2.8.1 Bacterial Recovery Test

Our optimized ANAs with unique optical and thermal characteristics provide an opportunity to exploit the near-field intensity enhancement and heat generation at the nanodisk surface to realize highly efficiency inactivation of *Vibrio cholerae*. To analyze the antimicrobial properties of our optimized ANAs, we constructed plexiglass chambers and artificially seeded glass slides with a monolayer biofilm of *Vibrio cholerae* at room temperature in the dark for 1 hour to allow for surface attachment of bacteria. We then added fresh PBS to refill the chamber to a volume of 1 ml to ensure that only surface attached bacteria are present in the chambers before 405 nm light exposure. To quantify the number of surface attached bacteria, we performed bacterial cell recovery tests. To non-invasively collect most of the adhered *Vibrio cholerae* bacteria from the surface after a 1-hour attachment, we investigated the effect of different experimental conditions on the bacterial recovery efficiency. First, pipetting time for recovery was investigated. An overnight culture (GFP-tagged strains) was diluted 1/100 into 2% LB and 1 mL of this bacterial suspension was pipetted into the chamber for a 1-hour incubation at room temperature in dark. Subsequently, the supernatant bacterial solution was aspirated, and the chamber was gently washed with

PBS twice. Following the gentle wash, the chamber was refilled with 1 mL of PBS followed by aggressive pipetting to detach all the cells from the surface. To determine the optimal pipette time to achieve the best cell detachment efficiency, three pipetting times 30, 60 and 90 seconds were tested, and the number of detached cells was compared. Cross-sectional patterns were used to evenly agitate the surface of the slide. The recovered bacterial solution was then serially diluted in PBS and track plated on LB agar plates in triplicate. The supernatant bacterial solution and the solution of the second gentle wash were also serially diluted and track plated. Enumeration of the surviving bacterial cells was accomplished by manually counting viable colonies on the plate. The results from the table 2-1 show that 90- seconds of PBS pipetting detached more cells than those of 30- or 60- seconds pipetting. Although there are around $6.0x10^5$ CFU's in the second wash, there is a 2 orders of magnitude difference in CFU's compared to the results of PBS pipetting. Therefore, the PBS gentle wash before aggressive pipetting has minimal impact on quantifying surface attached cells. The recovered slides were inspected by using fluorescence microscopy to track the remaining GFP-tagged bacterial cells on the surface after the aggressive pipetting. As shown in Fig. 2-9, the number of the remaining bacteria cells drastically decreases following 30-seconds pipetting. On the contrary, negligible difference was observed for the number of the remaining bacteria cells in between 60- and 90-seconds pipetting. These observations suggest that 90-seconds pipetting is the most viable pipetting time for the best bacterial cell recovery efficiency and we used this protocol in our bacterial light exposure experiments.

	Supernatant	Second gentle wash	30 s pipetting	60 s pipetting	90 s pipetting
CFU/mL	$1.0\text{-}2.0\times10^{7}$	6.0×10^{5}	1.0×10^{7}	1.3×10^{7}	1.65×10^{7}

Table 2-1. Bacterial recovery results

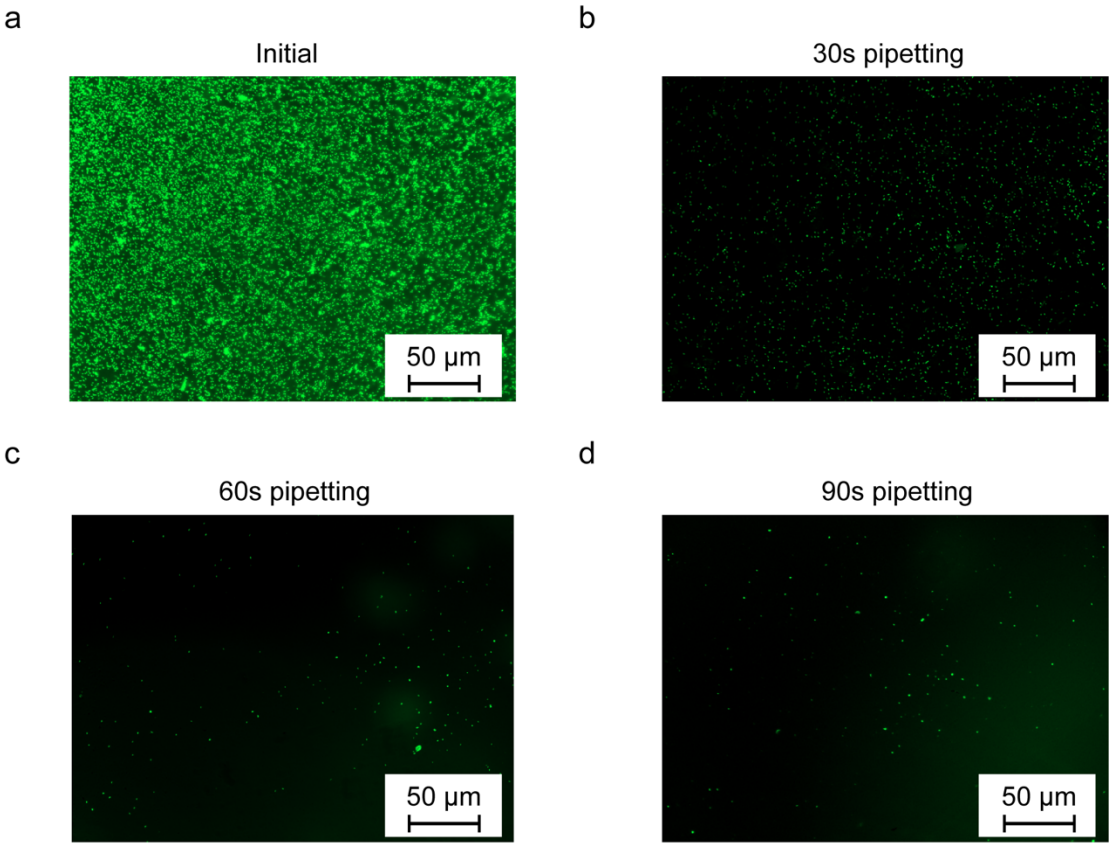

Figure 2-9. Microscopy data of remaining *Vibrio cholerae* cells on the surfaces of glass slides before (a) and after 30- (b), 60- (c), and 90- seconds (d) aggressive pipetting. GFP tagged strain of *Vibrio cholerae* was used to determine the optimal pipetting time to harvest most of the cells from the glass slide with minimal impact on the cell viability.

In addition, different detergent solutions were examined for bacterial recovery. PBS and its mixture with Tween-20 at various dilutions (also called PBST) were tested. 0.001%, 0.005% and 0.01% (v/v) PBST were prepared in 1 mL PBS before they were used for 90-seconds aggressive pipetting. The 2% LB diluted culture was mixed with either PBS or PBST in order to test whether Tween-20 affects viability of *Vibrio cholerae*. The results in the Table 2-2 suggest that Tween-20 aids removing cells from the surface as increasing Tween-20 concentration improves the cell recovery. However, we found that Tween-20 adversely impacts cell viability of *Vibrio cholerae* (Table 2-3). Based on these experimental tests, we conclude that 90 seconds of pipetting with PBS is the most viable approach for efficient recovery of *Vibrio cholerae*.

	Source	Initial	PBS	0.01% PBST	0.005% PBST	0.001% PBST
CFU/mL	3.9×10^{9}	1.47×10^{7}	1.13×10^{7}	1.13×10^{7}	1.08×10^{7}	9.6×10^{6}

Table 2-2. Results of different concentrations of PBST

	2% LB without 0.01% Tween 20	2% LB with 0.01% Tween 20
CFU/mL	2.23×10^{7}	1.6×10^{7}

Table 2-3. Results of Tween-20 viability test.

2.8.2 Inactivation of *Vibrio Cholerae* Biofilms on Aluminum Nanodisk Array Surfaces by 405 nm Light

We tested exposure times of 0, 5, 10, and 20 min at an irradiance of 0.25 W/cm^2 on both ANAs coated and non-coated glass slides (Fig. 2-10a). Following light exposure, we removed all surface associated cells with 90 s of vigorous pipetting and recovered them for subsequent serial dilutions in phosphate-buffered saline (PBS) and track plating on nutrient Luria-Bertani (LB) agar plates. After overnight incubation at 30°C, single colonies were enumerated the following day and the $\log_{10}$ reduction (CFU/ml) was determined. On normal glass slides, exposure of surface attached *Vibrio cholerae* to doses of 75, 150, 300 J/cm^2 resulted in 0.54$\log_{10}$, 0.92 $\log_{10}$, and 1.8 $\log_{10}$ reductions, respectively. 0.56$\log_{10}$, 2.1$\log_{10}$, 4.5$\log_{10}$ reductions were observed for our optimized ANAs slide (Fig. 2-10b). As heat generation on the normal glass slide is negligible, its antimicrobial efficacy is solely dependent on the 405 nm light induced ROS that cause oxidative cellular damage and bacterial cell death. However, in the presence of the ANAs, more than 500-fold improvement is observed in bacterial inactivation efficiency. The enhanced near-field intensities and extended plasmon lifetimes not only increase light dose absorbed by the bacteria but also leads to the production of increased localized heat as discussed above, which potentiates the killing efficiency of 405 nm light,

To gain further insight into the combinatorial effects of ANAs on bacterial inactivation, we examined the morphological changes of bacteria exposed to a 405 nm LED with a

300 J/cm^2 light dose with scanning electron microscopy (SEM). Compared to the non-irradiated cells that show short rod morphology with a small bend in the middle (Fig. 2-10c), the irradiated cells appeared wrinkled and ruptured and exhibited evident cellular structural collapse that lead to loss of cell viability and metabolic activity (Fig. 2-10d). This bacterial membrane damage confirms the membrane-dependent bacterial inactivation mechanisms. To validate the SEM observations of cellular membrane damage, the membrane permeability was evaluated using live/dead staining. The intact and damaged cell membranes can be directly distinguished as the red fluorescent nucleic acid stains with relatively high molecular weight (propidium iodide, 668 Da) can only penetrate the damaged cells, while green fluorescent ones can enter both intact and damaged cells. As shown in Fig. 2-10e and Fig. 2-10f, a significant reduction in live cell population is observed with 405 nm light exposure.

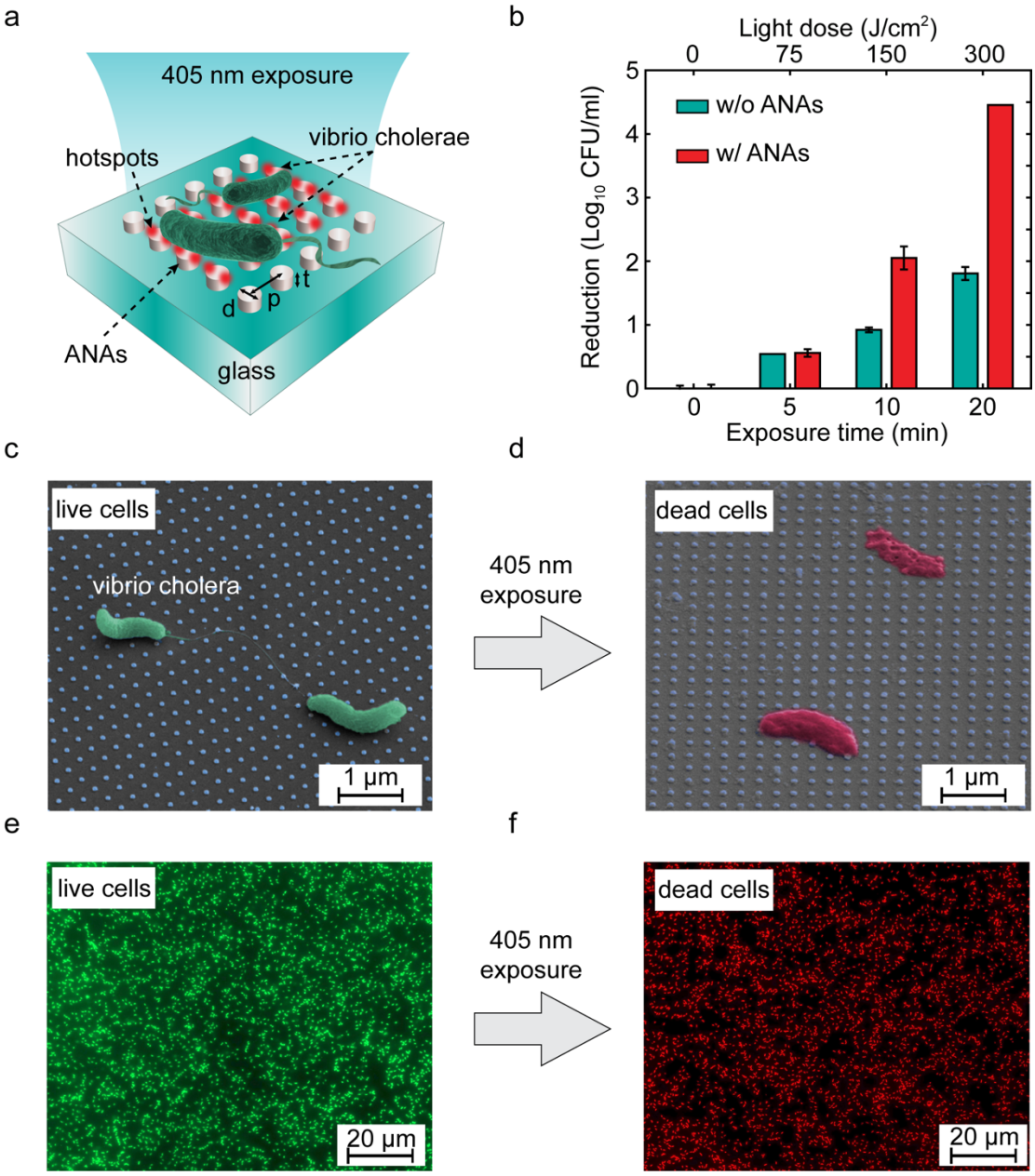

Figure 2-10. Inactivation of Vibrio cholerae under high-intensity 405 nm LED illumination. (a) The 405 nm LED is normally incident on ANAs coated glass slides that are already artificially seeded with Vibrio cholerae monolayers of biofilms in an aqueous environment. (b) Antimicrobial effect of Vibrio cholerae on normal (blue bars) and ANAs coated (red bars) glass slides during illumination with 405 nm LED at an

irradiance of 0.25 W/cm2. SEM images of non-illuminated (c) and illuminated (d) Vibrio cholerae cells seeded on the ANA coated glass substrate by 405 nm LED at a total dose of 300 J/cm2. Epifluorescent micrographs of Live/Dead Baclight stained Vibrio cholerae cells that are seeded on the ANAs coated glass slide before (e) and after (f) 405 nm LED illumination at a total dose of 300 J/cm2. Error bars represent three independent experimental measurements.

2.8.3 Experimental Methods

Bacterial Strains and Growth Conditions. O1 El Tor A1552 *Vibrio cholerae* (wild type) were grown aerobically in Luria-Bertani (LB) broth (1% tryptone, 0.5% yeast extract, 1% NaCl, pH 7.5) at 30°C. LB agar contained granulated agar (Difco) at 1.5% (wt/vol). Defined artificial seawater was used in place of PSB during the live/dead imaging [144].

Bacterial Surface Attachment. Overnight *Vibrio cholerae* liquid culture, inoculated from five single colonies, were diluted 1/100 in 2% LB (0.02% tryptone, 0.01% yeast extract, 1% NaCl, pH 7.5) and 1 mL of the diluted sample was pipetted into the preassembled glass slide chambers. These chambers contained either an untreated glass slide or an ANA coated slide. *Vibrio cholerae* then attached to the surface for one hour in the dark. We selected one hour for attachment as this has proven to be an adequate time for an irreversible surface attachment [145]. We used 2% LB to minimize cell growth as was previously done [146, 147]. Following attachment, the bacterial liquid was removed, and the chamber was washed with either PBS (bacterial recovery) or DASW (live/dead imaging). The chamber was refilled with the appropriate buffer and

exposed to blue light for different duration times. Controls were kept in the dark for the longest duration of light exposure.

Bacterial Recovery. After light exposure the PBS buffer in the chamber was pipetted aggressively to detach all cells from the surface. Cross-sectional patterns were used to evenly agitate the surface of the slide. The recovered bacterial liquid was then serially diluted in PBS and track plated on LB agar plates in triplicate. The 1/100 diluted cell culture and the bacterial liquid pre-light exposure were also serially diluted and track plated. Colonies were counted the following day.

Live/Dead Imaging. Using the BacLight Live/Dead kit, a mixture of equal parts component A and component B were mixed thoroughly, and 3 μL was added per 1 mL of DASW to make a diluted dye solution. After light exposure the DASW buffer in the chamber was discarded. The slide was removed from the chamber and 350 μL of the dye solution was gently pipetted onto the slide and incubated at room temperature in the dark for 30 minutes. The dye droplet was manipulated to cover the attached bacterial region of the slide. Following this, the dye solution was removed and the slide was submerged five times in DASW. One drop of mounting oil was placed on the slide, and then covered by a coverslip. Images were taken on UCSC Microscopy Facility's ZEISS Axioimager using the GFP fluorescent channel for the SYTO9 dye and the mCherry fluorescent channel for the propidium iodide.

SEM Imaging. Bacterial morphology on the surface of Al nanoantenna array was investigated before and after 20 min exposure using SEM imaging. Fixation of the samples was performed by immersion in 3% glutaraldehyde buffered with 0.1 M (1X)

PBS (pH=7.4) for 1 hour at room temperature. Samples were then washed twice in DI waster for 10 s followed by air dry. Subsequently, serial dehydration was employed by immersing samples in graded ethanol solutions (25%, 50%, 75%, 90%, 100%, and 100%) over 10 min at each step. Critical point drying of samples was carried out for 1 hour in Balzers Union 342/11 120B. Dried samples were then mounted on the specimen stubs with carbon adhesive and coated with ~20 nm Au thin film using sputtering system (Technics Hummer VI). Finally, samples were imaged by scanning electron microscope in a FEI Quanta 3D FEG Dualbeam operating at 5 kV and 6.7 pA.

2.9 Summary

In summary, we have introduced and implemented a unique space mapping algorithm enabling inverse design of a aluminum plasmonic nanoantenna array that satisfies a set of desired specifications, i.e., an extinction resonance wavelength of 405 nm and linewidth smaller than or equal to 15 nm. We have demonstrated that the use of the space mapping algorithm circumvents the systematical exploration in a huge parameter space, instead enables us to rapidly and accurately retrieve the fittest parameter sets from the desired optical response spectrum with a minimum number of high-fidelity and computationally expensive model evaluations. The optimized aluminum plasmonic nanoantenna array is found after only three iterations using the space mapping algorithm. Subsequently, these structures are fabricated on a 8-inch fused silica wafer using a wafer-scale ultraviolet interference lithography technique. The measured extinction spectrum of the optimized device shows excellent agreement with the

predictions of our computationally efficient inverse design approach. Due to its remarkable adaptability, our approach holds potential for a wide range of physical and optical parameters of the structure materials and geometrical configurations and the efficient inverse design of plasmonic nanoantenna arrays for a variety of applications, such as photovoltaics, biosensing, optoelectronics. Our optimized aluminum plasmonic nanoantenna array based on radiative decay engineering principles maximize the near-field enhancements and photothermal heating at 405 nm, a wavelength which bacteria is extremely vulnerable. In our experiments with low illumination intensities (2.5 mW/mm^2), we demonstrate that our optimized aluminum plasmonic nanoantenna array enables rapid eradication (~20 min) of multidrug-resistant Vibrio Cholerae biofilms with more than 500-fold inactivation efficiency (~99.995%) with respect to the 405 nm light alone.

Chapter 3

Plasmofluidic Microlenses for Label-Free Optical Sorting of Exosomes

This chapter presents a subwavelength thick (< 200 nm) Optofluidic PlasmonIC (OPtIC) microlens that effortlessly achieves objective-free focusing and self-alignment of opposing optical scattering and fluidic drag forces for selective separation of exosome size bioparticles. Our optofluidic microlens provides a self-collimating mechanism for particle trajectories with a spatial dispersion that is inherently minimized by the optical gradient and radial fluidic drag forces working together to align the particles along the optical axis. We demonstrate that this facile platform facilitates complete separation of small size bioparticles (i.e., exosomes) from a heterogenous mixture through negative depletion and provides a robust selective separation capability for same size nanoparticles based on their differences in chemical composition. Unlike existing optical chromatography techniques that require complicated instrumentation (lasers, objectives and precise alignment stages), our OPtIC microlenses with a foot-print of 4 μm × 4 μm open up the possibility of multiplexed and high-throughput sorting of nanoparticles on a chip using low-cost broadband light sources.

3.1 Motivation

Optical chromatography is a powerful fractionation technique that has recently gained significant attention for label-free separation and analysis of microscopic bioparticles (cells, bacteria, etc.) [148-151] . This technique relies on a mildly focused Gaussian laser beam along a microfluidic channel to create opposing optical scattering and fluidic drag forces [152, 153]. One can harness the varying strength and balance of these forces on bioparticle size, composition and morphology for selective sorting. Initially demonstrated for size-based elution of polystyrene beads, optical chromatography has been successfully applied to fractionation of blood components such as human erithrocytes, monocytes, granulocytes, and lymphocytes [149, 152]. This technique particularly excels in distinguishing bioparticles with subtle differences [151-154]. Its highly precise separation capability has been recently demonstrated for micron size bioparticles with diameters that differ by less than 70 nm [155]. Most remarkably, separation of two closely related genetic relatives, Bacillus anthracis and Bacillus thuringiensis [151], and cells with single gene modifications [150] has been achieved using small differences in their chemical makeup (refractive index). In essence, optical chromatography offers unique capabilities as a modern separation technique, especially when combined with multi-stage sequential fractionation and microfluidic network-based purification approaches [156, 157]. However, several critical limitations must be overcome for its wide adaptation: (1) To create strong optical scattering forces along the microfluidic channels, high cost laser sources are needed [149]. (2) Laser beam must be precisely aligned along the fluidic channel with

a well-controlled beam waist profile, requiring a complicated optical alignment procedure that employs multiple multi-axis positioners [152]. (3) Scaling of existing optical chromatography techniques for multiplexed and high throughput operation is not practical, since each channel requires separate alignment sensitive and high-cost laser sources and objectives [157].

In this report, we introduce **O**ptofluidic **P**lasmon**IC (OPtIC)** microlenses to overcome the shortcoming of existing optical chromatography techniques by eliminating the need for sophisticated instrumentation and precise alignment requirements. Our sub-wavelength thick (~ 200nm thick) OPtIC microlenses offer objective-free focusing and self-alignment of optical and fluidic drag forces and present a facile platform for selective separation of exosome size bioparticles. By allowing direct coupling of collimated broadband light to realize strong optical scattering forces at a focal point, extremely small footprint (4 μm × 4 μm) OPtIC microlenses open the door for drastically multiplexed optical chromatography and high-throughput sample processing capability. In addition to parallel operation, laterally integrated OPtIC microlenses on a planar chip permit serial microfluidic schemes [156, 157] to be readily implemented for multi-stage sequential separation and purification using broadband light sources and conventional planar microfluidic approaches. In the following, we show that our optofluidic sorting scheme based on OPtIC microlenses enables selective separation of exosome size bioparticles (< 200 nm in diameter). Furthermore, we demonstrate that our platform offers readily tunable, highly reliable and selective separation of nano-bioparticles by adjusting the light intensity (i.e. radiation pressure)

and/or the fluid flow rate (i.e. opposing drag force) based on size and minor difference in chemical makeup (refractive index).

3.2 Optofluidic-Plasmonic (OPtIC) Microlenses

As shown in recent studies, periodic and quasi-periodic arrays of plasmonic nanoapertures can be used as micro-convex lenses focusing incident plane waves to dimensions comparable to optical wavelengths [158-160]. In addition to significantly-small fingerprints, this focusing capability can be exploited to realize large optical scattering forces using collimated broadband light sources [161, 162]. In particular, finite size nanole array (NHA) structures provide a broadband focusing capability that is mainly controlled by the overall size of the array and tolerant of substructural variations [160]. The distinct nature of light focusing mechanism in NHA microlenses opens the door for nanofluidic integration through alterations in array design without degrading their focusing characteristics. A suspended plasmofluidic (OPtIC) microlens based on this principle is shown in Fig. 3-1. Here, an 9×9 array of nanoholes with a diameter of d=150 nm and a periodicity of a_0 = 380 nm is considered (Fig. 3-1a). NHA patch with a foot print of 4 μm × 4 μm is defined through a 120 nm thick gold film, 10 nm thick accompanying titanium (Ti) adhesion layer and a suspended silicon nitride (Si_3N_4) membrane (thickness of 100 nm) for microfluidic access from each side of it [163]. The periodic nanohole lattice allows enhanced light transmission through extraordinary light transmission effect (EOT) [164-167]. The center nanohole is

enlarged to facilitate nanofluidic flow. In Fig. 3-1a, the enlarged center hole diameter is d_c=500 nm. The overall device is a hybrid nanoplasmonic and nanofluidic system in which fluidic flow through the enlarged center aperture is achieved by pumping a solution from an inlet port on the top side and extracting it through an outlet port on the bottom side [168, 169]. The inlet and outlet ports are located away from the plasmofluidic microlense to provide a clear path for the optical beam [168]. Following Hagen-Poiseille's law $Q=\Delta p/R_H$ [$m^3\ s^{-1}$], the pressure-driven flow through a circular opening of length h can be understood using hydraulic resistance R_H, which is inversely proportional to the fourth power of the opening radius [170]: $R_H \approx 8\mu h / \pi r_H^4$ [$Pa\ s^3\ m^{-1}$], where μ=8.9×10^{-4} Pa·s is the dynamic viscosity of water and $h= t_{Au} +t_{Ti}+t_{SiN}$=205 nm is the cylindrical conduit thickness. For an enlarged circular center aperture of d_c=500 nm, the hydraulic resistance is more than two orders of magnitude smaller than that of the smaller nanoholes (d=150 nm) around it. The least fluidic resistance path through the enlarged center aperture (d_c=500 nm) leads to focusing of the convective fluidic flow along optical axis (OA), as demonstrated in our finite-element (FEM) microfluidic calculations (Fig. 3-1b). Here, the flow through the centrally located enlarged aperture serves two purposes: (1) it brings nanoparticles to the focal point of the OPtIC microlense, and (2) it forces nanoparticles to follow a trajectory that goes through the OA, as illustrated in Fig. 3-1c. One can achieve optofluidic alignment by introducing a collimated light beam that is perpendicularly incident from the bottom of the OPtIC microlens (Fig. 3-1c). The beam focused by the OPtIC microlens, hence optical scattering force ($\mathbf{F_s}$), is spontaneously aligned against the fluidic drag force ($\mathbf{F_g}$)

along the OA. Electromagnetic heating of the plasmofluidic microlense establishes a temperature gradient and heat induced convection current. The resulting thermo-plasmonic drag force ($\mathbf{F_{tp}}$) contributes to the optical scattering processes in balancing the fludic drag. As illustrated in Fig. 3-1c., in addition to providing a scattering force ($\mathbf{F_s}$) along the OA, light focused through the OPtIC microlens introduces an optical gradient force ($\mathbf{F_g}$) that radially pushes particles towards the OA. Combined with the radial drag forces ($\mathbf{F_{d,r}}$), at the focal point region, optical gradient force provides a robust mechanism for precise alignment of particles along the OA, as illustrated in Fig. 3-1c. For sufficiently large optical pressures that overcome the fluidic drag force ($\mathbf{F_s > F_d}$), particles are propelled against the fluidic flow along the OA. Hence, larger and higher refractive index particles (Fig. 3-1c, green color) experiencing larger optical scattering forces are kept at a distance away from the planar surface, whereas the smaller diameter and lower refractive index particles (Fig. 3-1c, yellow colored) are allowed to pass through the enlarged center aperture, resulting in complete separation of small size bioparticles (i.e., exosomes) from a mixture of larger size particles through negative depletion. Here, the OPtIC microlens serves as a far-field screen that prevents clogging of the center nanofluidic channel by keeping larger bioparticles away from the nanoaperture surface and high flow rate regions close to the center aperture.

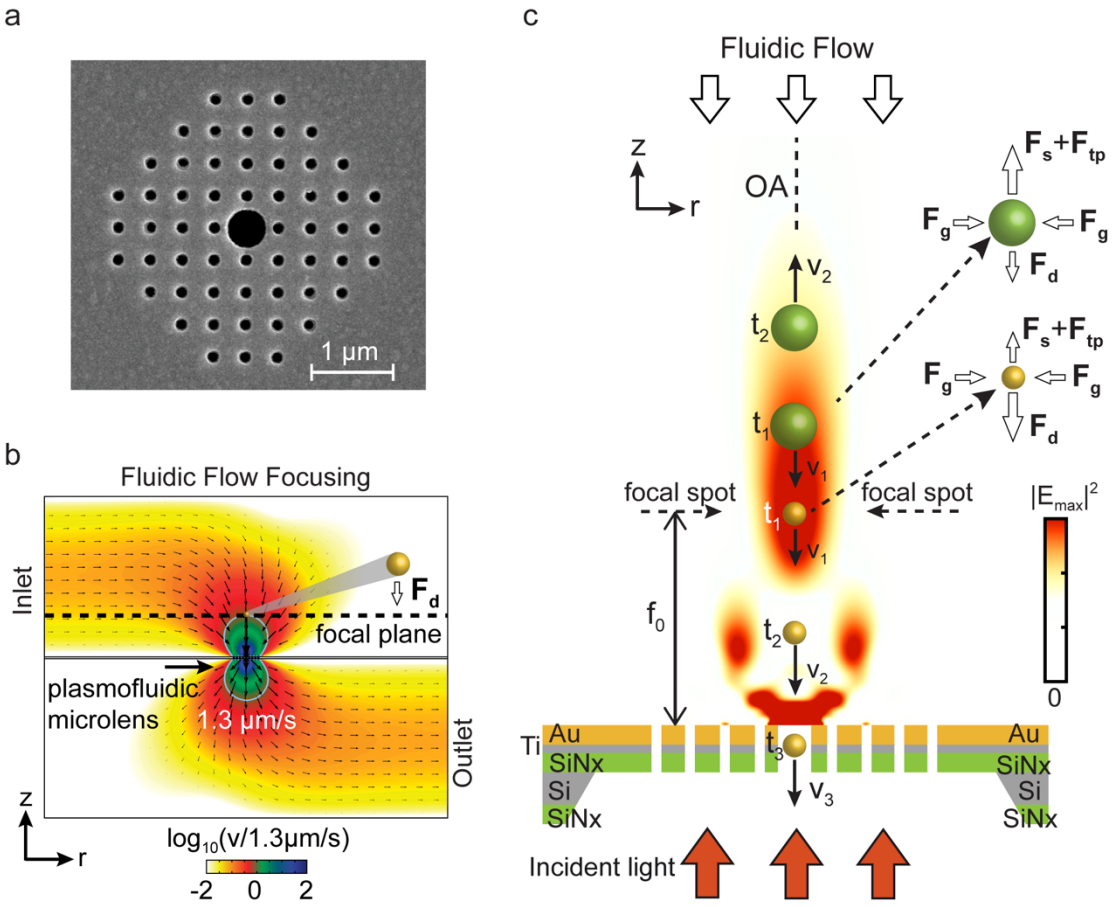

Figure 3-1. (a) A 4 μm × 4 μm OPtIC microlens consisting of a patch array of small circular nanoholes and an enlarged center aperture for nanofluidic integration. (b) Fluidic flow profile through the OPtIC microlens with a fluidic flow rate of 1.3 μm/s at the focal point. (c) Separation of two different size particle is illustrated at the focal point region. Fluidic drag ($\mathbf{F_d}$), optical scattering ($\mathbf{F_s}$) and thermo-plasmonic convection ($\mathbf{F_{tp}}$) forces are inherently aligned against each other along the optical axis by the OPtIC microlens.

3.3 Light Focusing with Plasmofluidic Microlens

A critically important device parameter is the nanofluidic channel (center aperture) diameter, which controls the size exclusion range in addition to the focusing behavior of the optic microlens [160]. The enlarged center aperture d_c must be incorporated without deteriorating the focusing characteristics and the desired size selectivity. In Fig. 3-2a, intensity profiles of OPtIC microlenses with varying center aperture diameters are shown for an incident light beam at λ=633 nm. The intensity profiles of a NHA without a center aperture (d_c = 0), a uniform NHA (d_c = 150 nm) and a NHA with an enlarged center aperture (d_c = 500 nm) reveals that the enlarged center aperture has negligible effect on the focusing behavior. Even for significantly larger center aperture dimensions (d_c = 800 nm), OPtIC microlens manages to focus light to a tight spot, albeit with a lower efficiency (degraded focusing characteristics). The checkerboard-like intensity profile close to the microlens surface (Fig. 3-3) is due to the diffractive self-imaging of smaller size nanoholes around the center aperture, an effect known as plasmonic Talbot effect [160, 171]. The enhanced light intensity regions around the larger diameter center openings (d_c = 500 nm and 800 nm) is associated to the diffractive transmission of light through the enlarged aperture. As shown in Fig. 3-2b, for large enough openings ($d_c \geq$ 500 nm), the light intensities in these diffractive transmission regions are comparable to or higher than those at the focal point. However, in contrast to the focal point, fluidic drag forces ($\mathbf{F_d} \propto$ v) are much stronger than the optical scattering forces ($\mathbf{F_d >> F_s}$) in these diffractive transmission regions. Our analysis shows nearly three orders of magnitude enhanced fluidic flow velocities close

to the center aperture as the fluidic velocity increases rapidly as the fluidic flow squeeze through the narrow center aperture with 500 nm diameter (Fig. 3-1b). Hence, small size and lower refractive index particles that are filtered through the focal point region can follow the fluidic flow lines to the other side of the OPtIC microlens without hinderance in the diffractive transmission regions close to center aperture. Therefore, in the following, we optimized our OPtIC microlens design for the focal point where comparable strength optical scattering, thermo-plasmonic convection and fluidic drag forces can be readily created for selective sorting purposes.

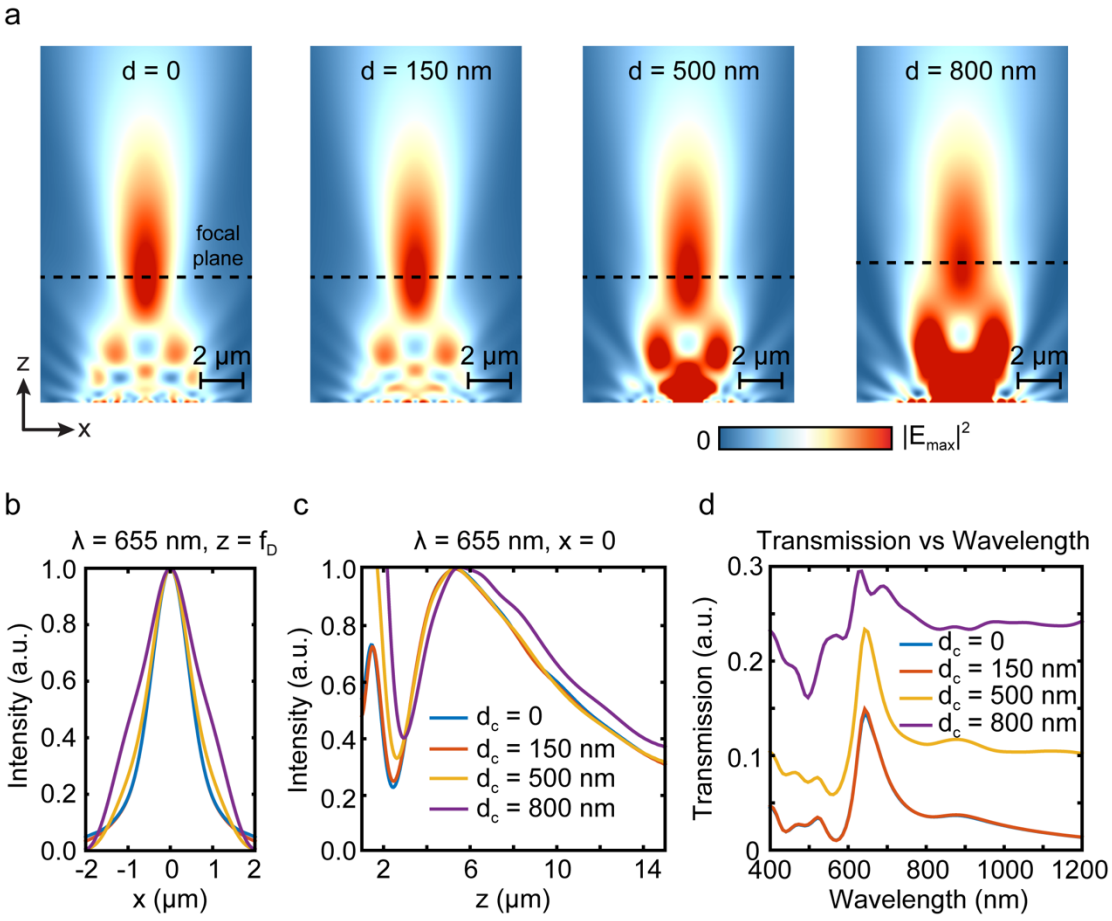

Figure 3-2. (a) Focused beam profiles are shown for OPtIC microlenses with varying center aperture diameter at λ = 655 nm. (b) Field profiles along the focal plane are compared. (c) Focal length and depth of focus of OPtIC microlenses are obtained using intensity profile along the optical axis. (d) Transmission spectra is shown. Extraordinary light transmission effect leads to a transmission peak at 650 nm.

Enlarged center aperture minimally affects the focal distance f_D, as shown in Fig. 3-2b. The focal distance f_D is 5.32 μm for d_c = 0, 150 nm, and 500 nm, whereas it only slightly increases to 5.56 μm for d_c = 800 nm. Similarly, a wider focal spot size at $z = f_D$ is observed for microlenses with larger center apertures (Fig. 3-2c). For microlenses with d_c = 0 and 150 nm, spot sizes are almost identical with a full-width at half maximum (FWHM) spread of w =1.12 μm. For $d_c \geq$ 500 nm, w increases with increasing center aperture opening; for d_c= 500 nm and 800 nm, we find that the spot sizes are w = 1.24 μm and 1.80 μm, respectively. Focusing characteristics of OPtIC microlenses are mainly controlled by the smaller diameter nanohole array created around the center enlarged aperture. Transmission spectra obtained using a field monitor is shown in Fig. 3-2d. EOT effect occurs at wavelengths that satisfy the Bragg condition: $\vec{G} = i\vec{G}_x + j\vec{G}_y$, where (i, j) are the integer values for the corresponding grating order [164, 166]. In Fig. 3-2d, the grating coupled (1,0) resonance transmission peak is observed at 650 nm (FWHM ~ 55 nm), confirming that light focusing is a result of interference of in-phase photons emerging from the periodic small size nanohole array [160]. For center apertures with diameters up to d_c = 500 nm (Fig, 3-2d, yellow curve), transmission

spectra show minimal deviation from a uniform NHA microlens without a center aperture ($d_c = 0$) [160], albeit with some broadband background transmission. On the other hand, for significantly larger center openings ($d_c = 800$ nm), non-resonant light transmission through the center aperture increases, leading to an increased background signal and broadening of the resonant transmission peak (Fig. 3-2d, violet curve). Based on the focusing behavior, attainable fluidic flow velocities at the focal point, and transmission spectra discussed above, we determined that an OPtIC microlens consisting of 9×9 array of nanoholes (diameter of d=150 nm and a periodicity of a_0 = 380 nm) with a center aperture of $d_c = 500$ nm is ideal for sorting of small size particles, such as exosomes. This microlens design is used in the rest of this paper.

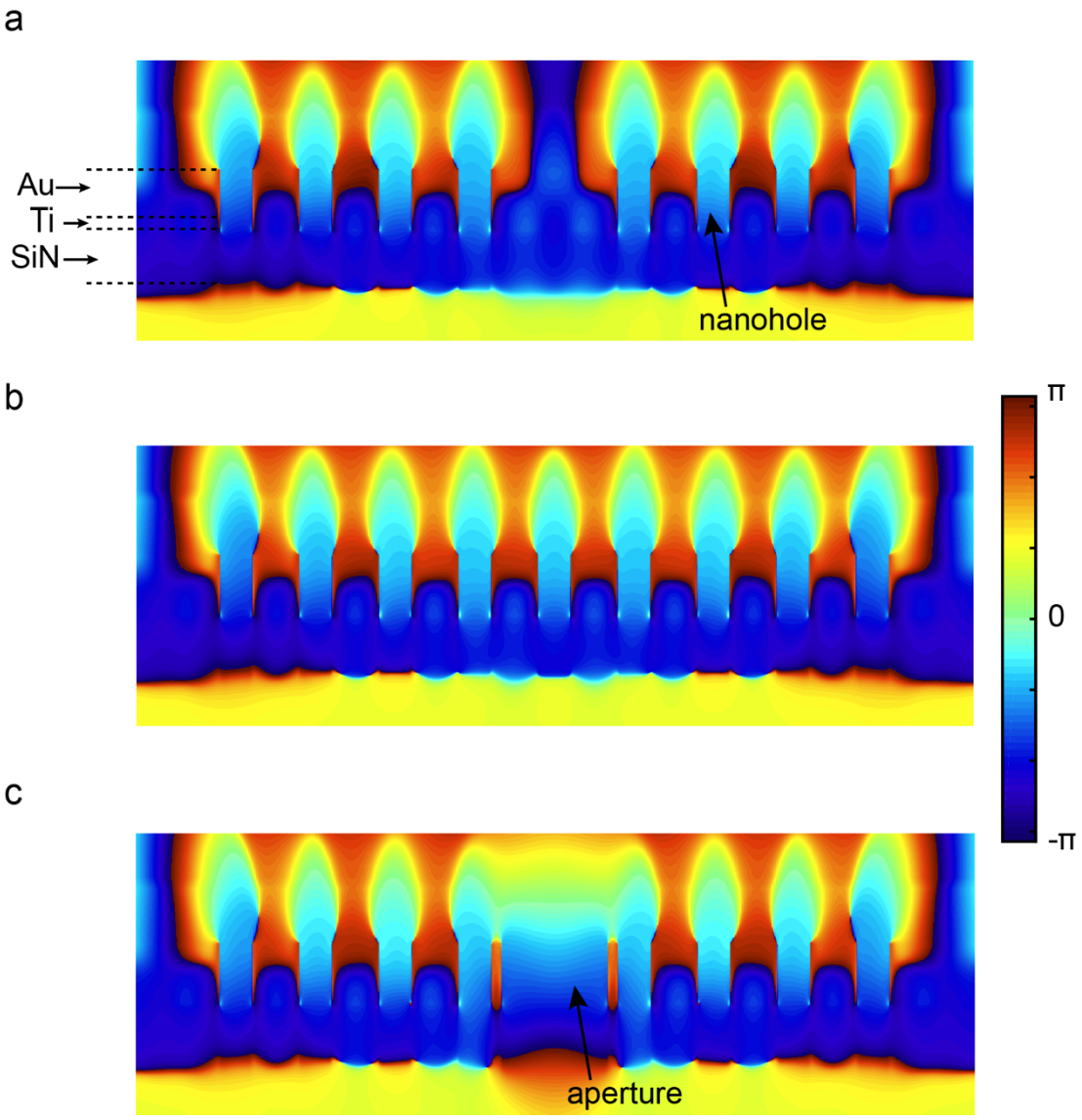

Figure 3-3. FDTD calculations of near-field phase map of electromagnetic waves emerging from the nanohole array (a) in the absence of the center nanohole (d_c =150 nm), (b) in the presence of the center nanohole (d_c =150 nm), (c) in the presence of the center enlarged aperture (d_c =500 nm). Each nanohole transmits electromagnetic field with nearly equal amplitude and phase, resulting in in-phase interference of the electromagnetic waves. The absence of the center nanohole or diffractive transmission

of light through the enlarged center aperture does not alter this checkerboard-like interference pattern.

High-intensity light sources, such as light emitting diodes (LEDs), are preferable to lasers for label-free size-based sorting applications. In this respect, NHA microlenses providing a focusing capability with minimal chromatic aberration are advantageous [160]. We analyzed the effect of center nanofluidic channel on the broadband focusing characteristics of our plasmofluidic microlens for a wavelength range spanning from 600 nm to 780 nm. Fig. 3-4a shows that f_D decreases monotonically with increasing wavelength [160]. However, a particularly small focal length variation $\Delta z \approx 200$ nm is observed for the wavelength range 620 *nm* $< \lambda <$ 680 *nm* corresponding to the (1,0) resonant transmission (EOT) peak. Outside the EOT spectral window, a significantly longer focal length is found at the transmission minimum λ =600 nm (Fig. 3-4a) that is associated to Wood's anomaly [167, 172]. We calculated focal spot size (w) along the focal plane denoted by the horizontal dashed lines in Fig. 3-4a. Within the (1,0) resonant transmission peak, only a slight difference is observed for the focal spot size. As shown in Fig. 3-4b, w is 1.08 μm, 1.12 μm, 1.24 μm and 1.28 μm at λ = 620 nm, 633 nm, 655 nm and 680 nm, respectively. Similarly, light intensity profile along the OA presents minimal variations within the 620 *nm* $< \lambda <$ 680 nm wavelength range (Fig. 3-4c). Hence, our analysis confirms that the (1,0) resonance transmission (EOT) peak provides a focusing behavior that is unaltered over a sufficiently-broad range of wavelengths.

The focal length of a finite-size opening that has identical dimensions to our plasmofluidic microlens can be calculated using the Rayleigh-Sommerfeld (R-S) formula [160, 173, 174]:

$$\frac{\mathrm{d}I}{\mathrm{d}z} = -2I_0 \frac{\pi\rho^2}{\lambda z^2} \sin\left(\frac{\pi\rho^2 n}{\lambda z}\right) = 0 \tag{3.1}$$

where z is the distance above the lens, I and I_0 are intensity and its peak values, respectively, whereas ρ is the radius of the opening and n is the refractive index of the surrounding medium. Our analysis shows that focal length f_D of our plasmofluidic microlens (Fig. 3-4d, black curve) is in good agreement with the values obtained from R-S formula (Fig. 3-4d, grey dots) for the wavelength range 620 nm < λ < 680 nm. Depth of focus (DoF) of our plasmofluidic microlens (shaded area bounded by the dashed lines) is shown in Fig. 3-4d. Even though the periodicity of nanohole array is broken with the incorporation of a nanofluidic channel (d_c = 500 nm) at the center, our analysis confirms that our plasmofludic microlens provides a well-defined focusing behavior with minimal chromatic aberration for the wavelength range of 620 nm < λ < 680 nm.

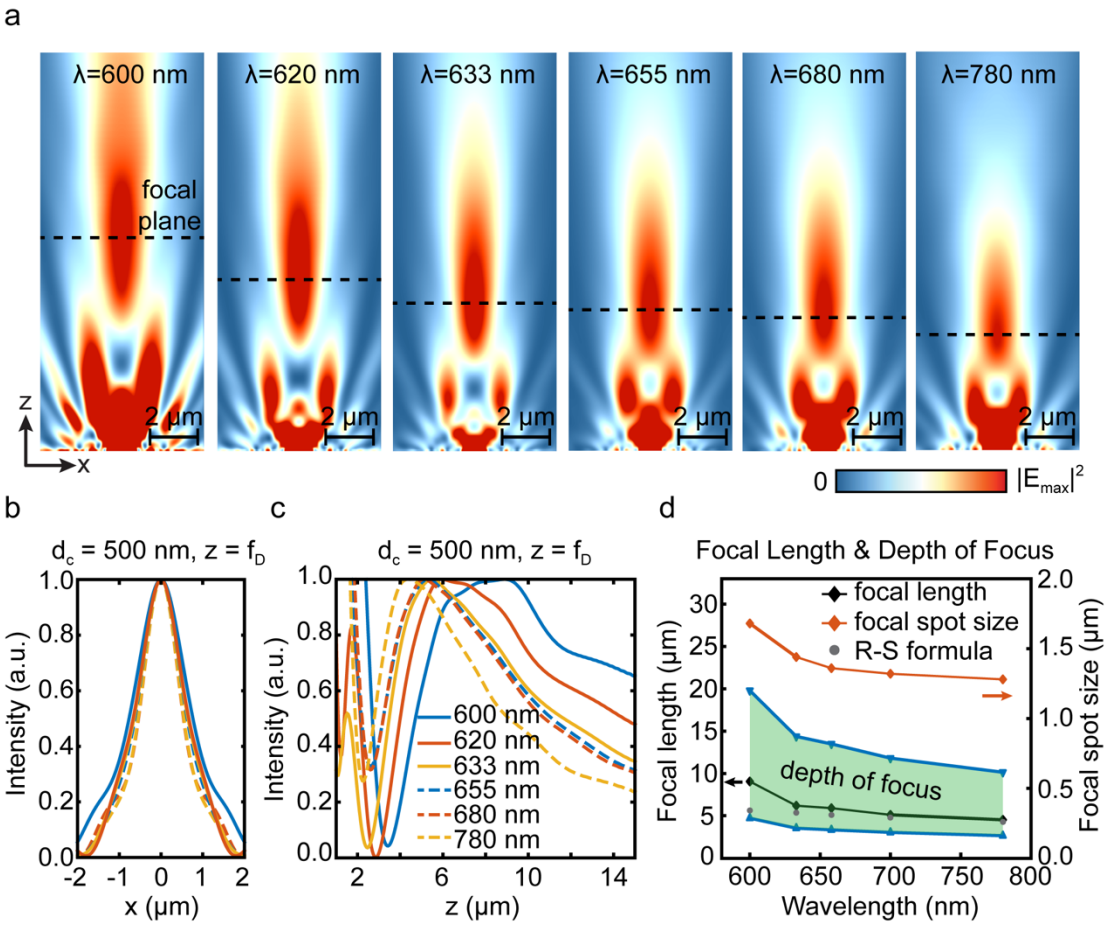

Figure 3-4. (a) Beam profile is shown for OPtIC microlens with 500 nm center aperture as function of incident light wavelength. (b) Field profiles along the focal plane are compared. (c) Focal length and depth of focus of OPtIC microlenses are obtained using the intensity profile along the optical axis. (d) Focal length, depth of focus and focal spot size are shown as a function of wavelength. Strong agreement with the values obtained from Rayleigh-Sommerfeld formula (grey dots) is observed.

3.4 Optical Scattering, Thermo-Plasmonic and Fluidic Drag Forces

Optical scattering forces acting on a bioparticle can be decomposed to two orthogonal components: a radial gradient force ($\mathbf{F_g}$) directed towards the beam axis and optical scattering force ($\mathbf{F_s}$) in the direction of beam propagation against the fluidic flow. These forces can be expressed as [161]

$$F_{s,g} = \frac{2n_m P}{c} Q_{s,g} \tag{3.2}$$

where P is the power of the incident light, n_m is the refractive index of the medium, c is the speed of light, and $Q_{s,g}$ is a dimensionless parameter defined for the scattering (s) and gradient (g) forces. $Q_{s,g}$ represents the efficiency of optical pressure transfer as a result of the light reflection/refraction at material interfaces. For simple beam profiles and symmetric geometries (i.e., a mildly focused Gaussian beam acting on a spherical particle), it is possible to calculate $Q_{s,g}$ analytically. For more complex beam profiles and small size particles with a diameter $a < 1$ μm, instead of the ray-optics model, optical forces must be calculated using Maxwell stress tensor (MST) [175, 176]:

$$T_{ij} = \varepsilon E_i E_j^* + \mu H_i H_j^* - \frac{1}{2}\delta_{ij}\left(\varepsilon |\mathbf{E}|^2 + \mu |\mathbf{H}|^2\right) \tag{3.3}$$

where **E** and **H** are the electric and magnetic field vectors, ε and μ are the electric permittivity and magnetic permeability of the medium, and δ_{ij} is the Kronecker delta. Combined with FDTD simulations, MST allows us to obtain scattering and gradient

forces acting on a particle for an arbitrarily shaped electromagnetic (EM) field distribution. Assuming a bounding box, small enough to contain only the particle of interest, the net optical force on the particle can be calculated as [176]

$$F = \oint_S \sum_j \frac{1}{2} \mathrm{Re}\left(T_{ij} \hat{n}_j\right) \tag{3.4}$$

where S is the surface of the bounding box and $\hat{n}_j$ is a unit vector along one of the principal axes.

For light intensities used here, electromagnetic heating of the OPtIC microlens can lead to large enough local temperature gradients inducing a buoyancy-driven convective flow away from OPtiC microlens surface [177, 178]. A comprehensive discussion of heat induced fluid dynamics can be found in elsewhere [179, 180]. Here, contribution of thermo-plasmonic effects is incorporated using finite element method (FEM). We first solve the electromagnetic wave equation for the electric field $\boldsymbol{E}$ around the OPtIC microlens with a 500 nm-diameter center aperture [181],

$$\nabla \times \left(\nabla \times \boldsymbol{E}\right) - k_0^2 \varepsilon(\boldsymbol{r}) \boldsymbol{E} = 0 \tag{3.5}$$

where $k_0 = 2\pi/\lambda$ is the free-space wave number, $\varepsilon(\boldsymbol{r})$ the position-dependent complex dielectric permittivity at the incident light wavelength. The calculated electric field distribution is used to obtain the heat source density $q(\mathbf{r}) = 0.5\mathrm{Re}[\mathbf{J} \cdot \mathbf{E}^*]$, where $\mathbf{J}$ is the induced current density in the microlens [181] and the total heat power $Q = \int q(\mathbf{r}) dv$. We then used coupled steady-state heat transfer and incompressible Navier-Stokes relations to calculate the temperature and thermo-plasmonic velocity field distributions

$$\nabla \cdot \left[\rho c_p T(\boldsymbol{r}) \boldsymbol{u}(\boldsymbol{r}) - \kappa \nabla T(\boldsymbol{r}) \right] = Q(\boldsymbol{r}) \tag{3.6}$$

$$\rho_0 \left[u(\boldsymbol{r}) \cdot \nabla \right] \boldsymbol{u}(\boldsymbol{r}) + \nabla p(\boldsymbol{r}) - \eta \nabla^2 \boldsymbol{u}(\boldsymbol{r}) = \boldsymbol{F} \tag{3.7}$$

where $\boldsymbol{\nabla} \cdot \boldsymbol{u} = 0$, $T(\boldsymbol{r})$, $\boldsymbol{u}(\boldsymbol{r})$, and $p(\boldsymbol{r})$ are the spatial temperature, fluid velocity, and pressure distributions, respectively. The material parameters for thermal conductivity κ, density ρ, specific heat capacity c_p, and kinematic viscosity η are taken from [180]. The steady-state temperature distribution on OPtIC microlens surface under 20 mW illumination at 633 nm is shown in Fig. 3-5a. Perpendicularly incident light transmitting diffractively through the center aperture is weakly coupled to the plasmonic excitations and dissipated within the metal film. Hence, a relatively low temperature difference from the ambient is observed within the center aperture region. Significantly higher local temperatures above the ambient are established outside the center aperture region due to non-radiative decaying of SPPs excited on gold surface. Due to limited thermal conductivity, the generated heat dissipates slowly into the solution medium, establishing a convective current away from the OPtIC microlens surface (Fig. 3-5b). We incorporated the contribution of this heat-induced convective flow in particle motion using Boussinesq approximation [178, 180, 182]

$$\boldsymbol{F}_{\text{tp}} = g \rho_0 \beta(T) \left[T(\boldsymbol{r}) - T_0 \right] \hat{z} \tag{3.8}$$

where $\boldsymbol{F}_{\text{tp}}$ is the imposed volume force, g, ρ_0, and β are the gravitational constant, water density, and thermal expansion coefficient of water, respectively.

The fluidic drag forces $\mathbf{F_d}$ acting on nanoparticles are added using Stoke's relation

$$\mathbf{F_d} = -6\pi\eta R\mathbf{v} \tag{3.9}$$

where η is the viscosity of the liquid medium, $\boldsymbol{v}$ is the velocity of the particle relative to the liquid medium and R is the particle radius. Contribution of radial fluidic drag forces ($\mathbf{F_{d,r}}$) in focusing particles along the OA is separately discussed in our analysis below.

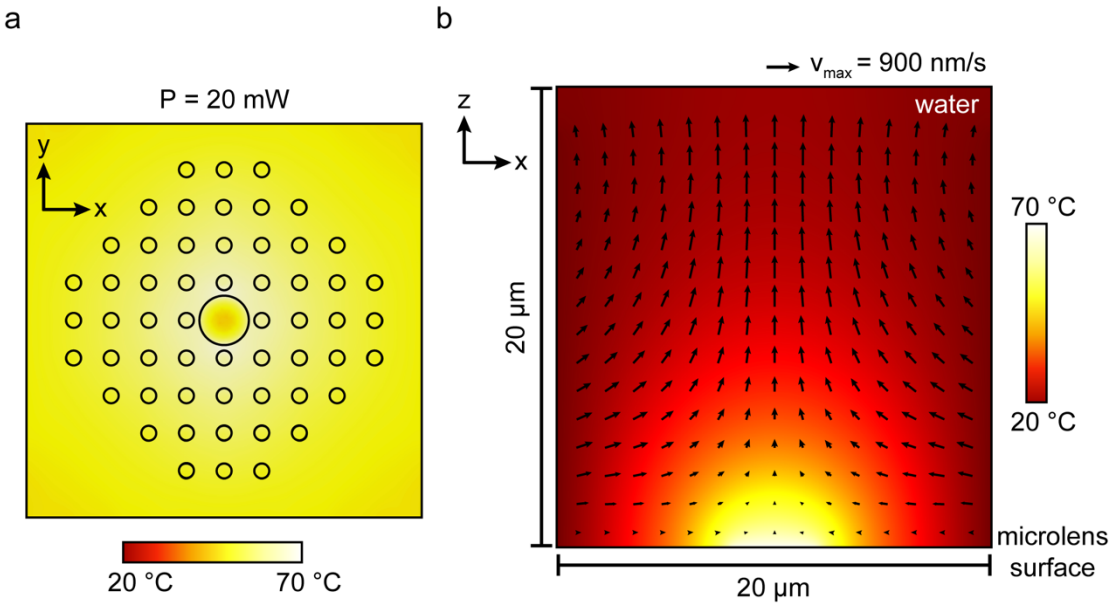

Figure 3-5. Finite element method (FEM) calculations of electromagnetic heating of the plasmofluidic microlense induced temperature gradient and heat induced liquid convection flow. (a) Top view of the temperature distribution on the surface of a OPtIC microlens a 500 nm center aperture under 20 mW 633 nm light illumination. (b) Thermo-plasmonics fluid convection pattern overlaid overlaid on the temperature distribution. The black reference arrow (v_{max}) indicates the maximum velocity of 900 nm/s, the velocity at f_D = 5.32 µm along the optical axis (OA) is approximately 360 nm/s.

3.5 Label-Free Sorting of Exosome Size Bioparticles

The robust size selective separation capability of our OPtIC platform is realized by harnessing the varying strength of optical scattering ($\mathbf{F_s}$), thermo-plasmonic convection ($\mathbf{F_{tp}}$), fluidic drag ($\mathbf{F_d}$) and gravitational ($\boldsymbol{W}$) forces based on size, refractive index and mass density of the bioparticles. The net forces ($\mathbf{F_{net}} = \mathbf{F_s} + \mathbf{F_{tp}} + \mathbf{F_d} + \boldsymbol{W}$) acting on submicron particles (a= 100 nm – 1 μm) at different locations along the OA (z = 0 – 6 μm) are shown in Fig. 3-6a,b. Here, a refractive index of 1.55 and a mass density of 1.05 g/cm^3 are assumed for the interrogated bioparticles. In Fig 3-6a,b, the blue (red) region corresponds to physical conditions (particle sizes and spatial locations along the OA) leading to a net force towards (away from) the center aperture. For particles with a small diameter (a_{th} < 200 nm), when 20 mW incident light (λ = 633 nm) and a fluidic flow velocity of 1.3 μm/s is used, optical scattering and thermo-plasmonic convention forces are weaker than the fluidic drag and gravitational forces ($\mathbf{F_d} + \boldsymbol{W} > \mathbf{F_s} + \mathbf{F_{tp}}$) at all locations along the OA (Fig. 3-6a, the vertical line on left). Hence, small diameter particles (a_{th} < 200 nm) can readily follow the fluidic flow lines along the focal point and the high-intensity regions close to the center aperture. These particles (a_{th} < 200 nm) make their way through the center aperture to the other side of the suspended OPtIC microlens and get separated from the mixture in the top channel (negative depletion). Under the same operating conditions, larger diameter particles (a > 200 nm) experience stronger optical scattering and thermo-plasmonic convection forces that can push them against the fluidic flow lines ($\mathbf{F_d} + \boldsymbol{W} < \mathbf{F_s} + \mathbf{F_{tp}}$). These larger bioparticles

(a_{th} > 200 nm) are retained in the top channel (Fig. 3-6a). Threshold bioparticle diameter a_{th} used for the size based fractionation can be readily tuned to a desired value by changing the light intensity and the fluidic flow velocity. In Fig. 3-6b, we show that the increased fluidic flow (velocity = 3.0 μm/s) shifts the threshold diameter (a_{th}) for size based sorting to 350 nm. By fine-tuning the relative contributions of the optical scattering, thermo-plasmonic convection and fluidic drag forces, microvesicles (up to 500 nm in diameter) can be selectively separated from larger bioparticles.

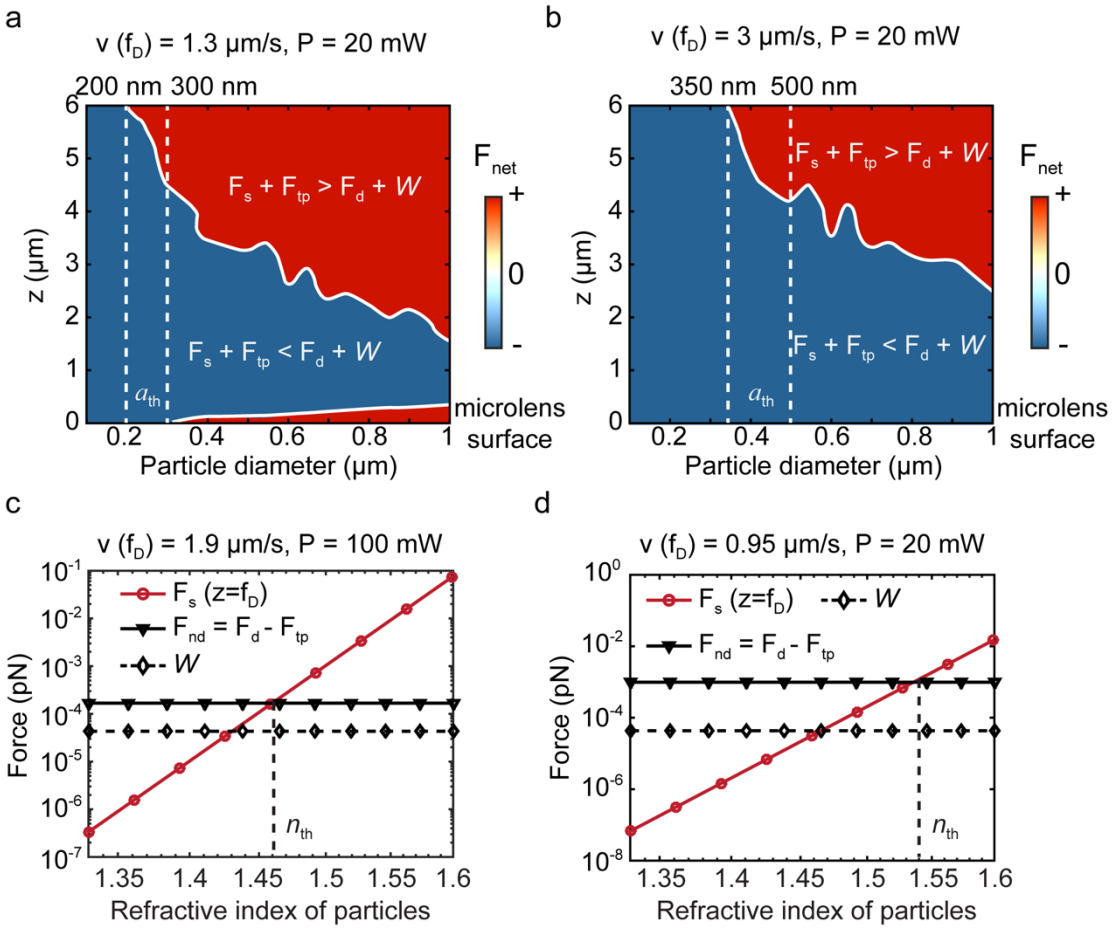

Figure 3-6. The net force ($\mathbf{F_{net} = F_s + F_{tp} + F_d + W}$) acting on submicron particles (a= 100 nm – 1 m) along the optical axis (z = 0 – 6 m) for flow conditions corresponding

to (a) 1.3 μm/s and (b) 3 μm/s flow rates at the focal point. We assumed that 20 mW incident light (λ = 633 nm) and a fluidic flow velocity of 1.3 μm/s is used 633 nm-wavelength incident light power (20 mW). Optical scattering ($\mathbf{F_s}$), net fluidic drag ($\mathbf{F_d} + \mathbf{F_{tp}}$), gravitational ($\boldsymbol{W}$) forces acting on a 200 nm exosomes-like bioparticle are shown as a function of particle refractive index (n_e) for (c) 1.9 μm/s flow rate and 100 mW incident power and (d) 0.95 μm/s flow rate and 20 mW incident power. The dashed vertical lines indicate the threshold particle refractive index (n_{th}) for which the net force acting the particles vanishes. Here, the lines are the first-order polynomial curve fits.

Minor differences in internal structure and chemical composition of bioparticles leads to effective refractive index variations that can be exploited for selective separation [151, 154]. A remarkable example of this is a recent study demonstrating that cells with single gene modifications can be distinguished based on their differences in chemical makeup using optical chromatography [150]. Based on the same physical principles, our plasmofluidic platform utilizing optical scattering, thermo-plasmonic convection and fluidic drag forces provides a highly sensitive refractive index-based bioparticle separation capability. In Fig. 3-6c, optical scattering $\mathbf{F_s}$ (red line) and net fluidic drag (black line) $\mathbf{F_d} + \mathbf{F_{tp}}$ forces are compared at the focal point (f_D = 5.32 μm, λ = 633 nm, P = 100 mW) as a function of effective refractive index (n_e) of bioparticles with a diameter of a = 200 nm. Gravitational forces ($\boldsymbol{W}$) acting on these particles are also shown (black dashed line). Here, the optical scattering forces $\mathbf{F_s}$ (red curve) are

calculated for an effective refractive index range spanning from n_e = 1.33 (water) to n_e = 1.6 (i.e., polystyrene particles). $\mathbf{F_s}$ increases with increasing n_e and balances the counter acting the net fluidic resistance force $\mathbf{F_d} + \mathbf{F_{tp}}$ for n_e = 1.46 (i.e., phospholipids and proteins) at a flow rate of $v(f_D)$ = 1.9 μm/s. For nanoparticles that have refractive indices lower than n_e <1.46, the fluidic drag forces are strong enough to carry them against the optical scattering forces through the enlarged center aperture to the chamber below the OPtIC microlens and separate them from a heterogenous mixture. This allows sorting of lower refractive index (n_e <1.46) particles from higher refractive index (n_e >1.46) ones. A particularly prominent observation is the significantly diminished optical scattering forces (~ 4 aN) obtained for the lower refractive index ($n_e \approx$ 1.37 – 1.39) particles, which is two order of magnitude weaker than the optical scattering forces (~ 400 aN) acting on higher refractive index particles with $n_e \approx$ 1.46 under same illumination conditions. Exosomes consisting of a thin phospholipid membrane enclosing a water load have lower effective refractive indices ($n_{exosome} \approx$ 1.37 –1.39) [183-185] that are closer to that of water ($n_{water} \approx$ 1.33). Virions, on the other hand, are a tight assembly of nucleid acids, proteins, and lipids; therefore have higher refractive indices ($n_{virus} \approx$ 1.48) [186]. Accordingly, our platform enables us to use this refractive index difference to separate exosomes from similar size virions (Fig. 3-6c). Similar to the size-based separation (Fig. 3-6a and 3-6b), the threshold refractive index can be tuned to a desired value by adjusting the fluidic flow rate and light power (Fig. 3-6d). As demonstrated by Fig. 3-6d, at a relatively small flow rate (0.95 μm/s) and incident power (20 mW), the net force ($\mathbf{F_s} + \mathbf{F_{tp}} + W + \mathbf{F_d}$) acting on the 200 nm particles

vanishes for particles with higher refractive index ($n_e \approx 1.54$) than those in Fig. 3-6c ($n_e \approx 1.46$). Furthermore, multiple OPtIC microlenses integrated on a single planar chip can be serially implemented to achieve differential sorting using an initial size-based fractionation and a subsequently separation based on differences in bioparticle chemical makeup (refractive index).

3.6 Radial Focusing of the Bioparticles

It is predicted that the instrumental fluctuations associated to variations in fluidic flow velocities can cause spatial dispersion of particles, deteriorating the size-based retention capability of conventional optical chromatography approaches [153]. Instead of mildly focused Gaussian beams, our OPtIC microlenses uses strongly focused the light that can create large optical gradient forces $\mathbf{F_g}$ in radial directions. As shown in Fig. 3-7a,b for 200 nm and 600 nm diameter particles, in addition to the optical gradient forces $\mathbf{F_g}$ (blue curve), the spatial dispersion of particles in our platform is inherently minimized by the fluidic drag $\mathbf{F_{d,r}}$ (black curve) and thermo-plasmonic convection $\mathbf{F_{tp,r}}$ (red curve) forces working together to align particles along the OA ($r = 0$). Here, an incident light ($\lambda = 633$ nm) power of 20 mW and a fluidic velocity of 1.3 μm/s are assumed. For distances up to ±1 μm away from the OA, the optical gradient ($\mathbf{F_g}$), thermo-plasmonic convective flow ($\mathbf{F_{tp,r}}$) and fluidic drag ($\mathbf{F_{d,r}}$) forces are reminiscent of a restoring force of a spring, which tends to align the particles at equilibrium position (along the OA). Here, an important observation is the relative strength of the optical gradient forces $\mathbf{F_g}$ with respect to those of the radial fluidic drag forces $\mathbf{F_{d,r}}$. Although

particles are initially brought towards OPtIC microlens through the fluidic flow, once they are close to high intensity focal point region, their relative alignment along the OA is mainly ensured by the optical gradient force. Therefore, our plasmofluidic optical chromatography technique provides a self-collimating mechanism for particle trajectories that is tolerant of the perturbations in fluidic flow rates.

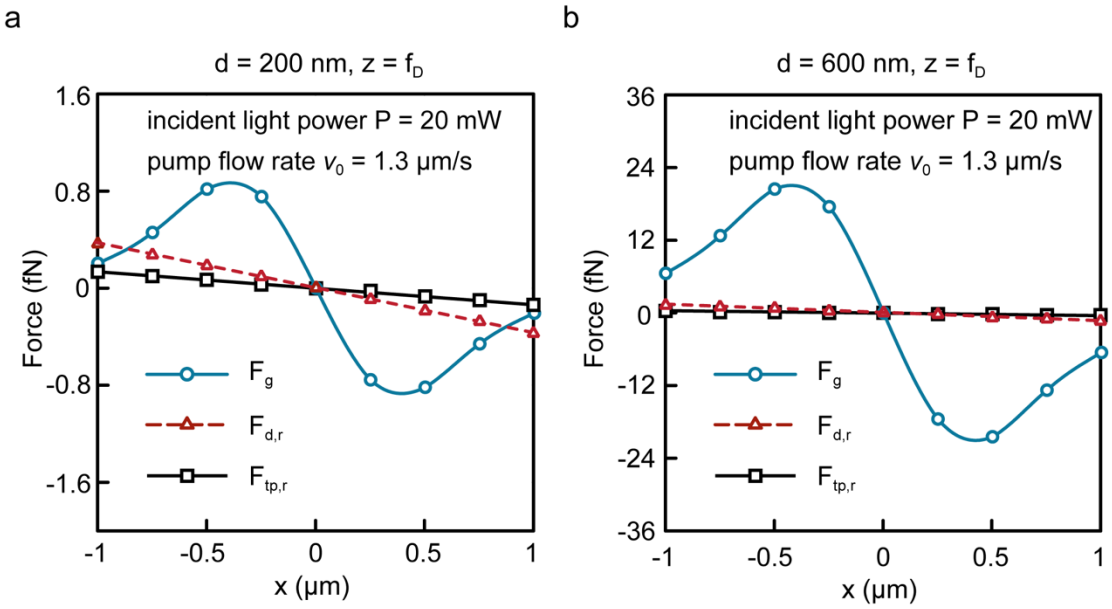

Figure 3-7. Optical gradient ($\mathbf{F_g}$), radial fluidic drag ($\mathbf{F_{d,r}}$), and radial thermo-induced fluidic drag ($\mathbf{F_{tp,r}}$) forces align particle trajectories with OA (x = 0). Force acting on particles are compared for particles with (a) a = 200 nm and (b) a = 600 nm diameter. Here, the curves are sinusoidal fits while the lines are the first-order polynomial curve fits.

3.7 Summary

In this chapter, we introduced a facile on-chip platform enabling optical sorting of nano-bioparticles based on size and chemical composition (refractive index). Unlike existing optical chromatography techniques that require complicated instrumentation (lasers, objectives, precise stages, etc.) for optofluidic alignment and optical scattering force creation [149, 152, 157], our platform achieves objective-free focusing of collimated broadband light and self-alignment of counteracting optical scattering and fluidic drag forces along the optical axis. To accomplish this, we developed a subwavelength thick optofluidic plasmonic (OPtIC) microlens merging focusing capabilities of NHA plasmonic microlenses [160, 168] with nanofluidics. Our OPtIC microlens effortlessly realizes precise alignment of nanoparticles along the optical axis using radially focusing fluidic drag and optical gradient forces. We demonstrated that our plasmofluidic platform facilitates selective separation of nanoparticles below a threshold diameter, which can be tuned to a desired value using fluidic flow rate and the incident light power. Furthermore, we showed that our platform offers a robust separation capability for same size nanoparticles using differences in their chemical composition (refractive index). A major limitation in flow cytometry measurements is the diminished optical signals obtained from small size and lower refractive index nano-bioparticles, such as exosomes [184]. Even with specialized flow cytometers equipped with high sensitivity detectors, the smallest detectable vesicles are typically larger than ~ 200 nm in diameter [184, 187]. Hence, vast majority of exosomes are overlooked in flow cytometry measurements, which is the most commonly used optical

method in clinical and research laboratories. In contrast, our optofluidic platform employs a negative depletion mechanism enabling selective enrichment of exosomes in a readily manner by removing the larger size and higher refractive index particles using optical radiation pressure. Furthermore, our platform could be used for quantification of exosomes passing through the center nanohole aperture through Coulter principle [188]. Two electrodes added on the opposite sides of the OPtIC microlens can detect brief changes (pulses) in the current that flows through the aperture, as the enriched exosomes transverse the enlarged center aperture. Previous studies have shown that resistive pulse sensing (RPS) technologies based on Coulter principle in aperture format are capable of detecting bioparticles smaller than 100 nm [189]. However, clogging of openings due to the larger particles has been a practical limitation when heterogenous samples are analyzed [184]. Our OPtIC microlens keeping larger diameter particles away from the nanoaperture opening using optical scattering forces, when combined with RPS, could overcome these limitations and be used for selective sorting and detection of exosomes from heterogenous samples. To achieve extended periods of operation and high-volume processing, one can incorporate a lateral microcross flow [190] periodically removing the particle microfumes that build up above the focal point of the OPtIC microlens.

Chapter 4

Summary and Outlook

In the last three chapters, I have addressed three important biomedical problems at three different length scales. I first present an innovative and low-cost acousto-microfluidic approach that overcomes the diffusion limitations imposed by laminar flow profile in microfluidic channels at a challenging flow regime corresponding to extremely low Reynolds (Re~10^{-4}) and high Péclet (Pe~10^{6}) numbers. Using this novel approach, we achieve immunoaffinity based isolation of cells using a simple rectangular channel without resorting to chaotic mixing processes or magnetic forces. Our acousto-microfluidic method uses a combination of pure and quasi-standing surface acoustic waves that are generated at a safe power (~ 1-10 W/cm^2) and frequency (~10 MHz) regime comparable to those used in ultrasound imaging (e.g. fetal imaging). By exploiting the local shear forces in the vicinity of the bottom channel boundary (defined capture surface), we achieve selective separation of desired particles/cells using pre-functionalized cell specific biomolecules. We demonstrate selective enrichment of low-abundance T lymphocyte cells with a separation efficiency of about 80% at a high flow rate of 1.2 mL/hr, a separation efficiency that is comparable to most advanced rare cell isolation technologies.

In the second part of my thesis (Chapter 2), I introduce a novel nanophotonic approach for enhanced inactivation of multidrug-resistant bacterial pathogens using visible light at 405 nm. To achieve this, I introduce precisely engineered aluminum nanoantenna

arrays using a space mapping algorithm enabling inverse design of nanostructures from the desired spectral response. The nanoantenna arrays are optimized using radiative decay engineering principles to maximize the near-field enhancements and photothermal heating at 405 nm, a wavelength which bacteria is extremely sensitive to light and used as an emerging light-based disinfection technology alternative to ultraviolent (UV) light. In our experiments with low illumination intensities (2.5 mW/mm^2), we demonstrate that our aluminum nanoantenna array (ANA) enables rapid eradication (~20 min) of multidrug-resistant *Vibrio Cholerae* biofilms with more than 500-fold inactivation efficiency (~99.995%) with respect to the 405 nm light alone.

In the final part of my thesis (Chapter 3), I introduce a subwavelength thick (<200 nm) Optofluidic PlasmonIC (OPtIC) microlens that effortlessly achieves objective-free focusing and self-alignment of opposing optical scattering and fluidic drag forces for selective separation of exosome size bioparticles at low flow rates (< 5 μm/s). Our optofluidic microlens provides a self-collimating mechanism for particle trajectories with a spatial dispersion that is inherently minimized by the optical gradient and radial fluidic drag forces working together to align the particles along the optical axis. I demonstrate that this facile platform facilitates complete separation of small size bioparticles (i.e., exosomes) from a heterogenous mixture through negative depletion and provides a robust selective separation capability for same size nanoparticles based on their differences in chemical composition. Unlike existing optical chromatography techniques that require complicated instrumentation (lasers, objectives and precise alignment stages), our OPtIC microlenses with a foot-print of 4 μm × 4 μm open up the

possibility of multiplexed sorting of nanoparticles on a chip using low-cost broadband light sources (LEDs).

Bibliography

[1] G.M. Whitesides, The origins and the future of microfluidics, Nature, 442 (2006) 368-373.

[2] P. Yager, T. Edwards, E. Fu, K. Helton, K. Nelson, M.R. Tam, B.H. Weigl, Microfluidic diagnostic technologies for global public health, Nature, 442 (2006) 412-418.

[3] E.K. Sackmann, A.L. Fulton, D.J. Beebe, The present and future role of microfluidics in biomedical research, Nature, 507 (2014) 181.

[4] A. Ozcelik, J. Rufo, F. Guo, Y. Gu, P. Li, J. Lata, T.J. Huang, Acoustic tweezers for the life sciences, Nature Methods, 15 (2018) 1021-1028.

[5] E.D. Pratt, C. Huang, B.G. Hawkins, J.P. Gleghorn, B.J. Kirby, Rare Cell Capture in Microfluidic Devices, Chemical engineering science, 66 (2011) 1508-1522.

[6] M. Toner, D. Irimia, Blood-on-a-Chip, Annual Review of Biomedical Engineering, 7 (2005) 77-103.

[7] M.P. MacDonald, G.C. Spalding, K. Dholakia, Microfluidic sorting in an optical lattice, Nature, 426 (2003) 421-424.

[8] A.D. Stroock, S.K.W. Dertinger, A. Ajdari, I. Mezić, H.A. Stone, G.M. Whitesides, Chaotic Mixer for Microchannels, Science, 295 (2002) 647.

[9] S. Nagrath, L.V. Sequist, S. Maheswaran, D.W. Bell, D. Irimia, L. Ulkus, M.R. Smith, E.L. Kwak, S. Digumarthy, A. Muzikansky, P. Ryan, U.J. Balis, R.G.

Tompkins, D.A. Haber, M. Toner, Isolation of rare circulating tumour cells in cancer patients by microchip technology, Nature, 450 (2007) 1235.

[10] S.L. Stott, C.-H. Hsu, D.I. Tsukrov, M. Yu, D.T. Miyamoto, B.A. Waltman, S.M. Rothenberg, A.M. Shah, M.E. Smas, G.K. Korir, F.P. Floyd, A.J. Gilman, J.B. Lord, D. Winokur, S. Springer, D. Irimia, S. Nagrath, L.V. Sequist, R.J. Lee, K.J. Isselbacher, S. Maheswaran, D.A. Haber, M. Toner, Isolation of circulating tumor cells using a microvortex-generating herringbone-chip, Proceedings of the National Academy of Sciences, 107 (2010) 18392.

[11] H.A. Stone, Introduction to Fluid Dynamics for Microfluidic Flows, in: H. Lee, R.M. Westervelt, D. Ham (Eds.) CMOS Biotechnology, Springer US, Boston, MA, 2007, pp. 5-30.

[12] D. Di Carlo, D. Irimia, R.G. Tompkins, M. Toner, Continuous inertial focusing, ordering, and separation of particles in microchannels, Proceedings of the National Academy of Sciences, 104 (2007) 18892.

[13] Z. Csuka, R. Olšiak, The profile of shear stress in the liquid at turbulent flow, AIP Conference Proceedings, 1768 (2016) 020032.

[14] R. Fitzpatrick, Theoretical Fluid Mechanics, IOP Publishing2017.

[15] J.C. Giddings, Field-flow fractionation: analysis of macromolecular, colloidal, and particulate materials, Science, 260 (1993) 1456.

[16] J.M. Martel, M. Toner, Inertial Focusing in Microfluidics, Annual Review of Biomedical Engineering, 16 (2014) 371-396.

[17] D. Di Carlo, J.F. Edd, K.J. Humphry, H.A. Stone, M. Toner, Particle Segregation and Dynamics in Confined Flows, Physical Review Letters, 102 (2009) 094503.

[18] M.M. Wang, E. Tu, D.E. Raymond, J.M. Yang, H. Zhang, N. Hagen, B. Dees, E.M. Mercer, A.H. Forster, I. Kariv, P.J. Marchand, W.F. Butler, Microfluidic sorting of mammalian cells by optical force switching, Nature Biotechnology, 23 (2005) 83-87.

[19] L.R. Huang, E.C. Cox, R.H. Austin, J.C. Sturm, Continuous Particle Separation Through Deterministic Lateral Displacement, Science, 304 (2004) 987.

[20] J. McGrath, M. Jimenez, H. Bridle, Deterministic lateral displacement for particle separation: a review, Lab on a Chip, 14 (2014) 4139-4158.

[21] B.R. Lutz, J. Chen, D.T. Schwartz, Hydrodynamic Tweezers: 1. Noncontact Trapping of Single Cells Using Steady Streaming Microeddies, Analytical Chemistry, 78 (2006) 5429-5435.

[22] S. Saito, H. Himeno, K. Takahashi, M. Urago, Kinetic control of a particle by voltage sequence for a nonimpact electrostatic micromanipulation, Applied Physics Letters, 83 (2003) 2076-2078.

[23] K. Takahashi, H. Kajihara, M. Urago, S. Saito, Y. Mochimaru, T. Onzawa, Voltage required to detach an adhered particle by Coulomb interaction for micromanipulation, Journal of Applied Physics, 90 (2001) 432-437.

[24] P.C.H. Li, D.J. Harrison, Transport, Manipulation, and Reaction of Biological Cells On-Chip Using Electrokinetic Effects, Analytical Chemistry, 69 (1997) 1564-1568.

[25] P.K. Wong, C.-Y. Chen, T.-H. Wang, C.-M. Ho, Electrokinetic Bioprocessor for Concentrating Cells and Molecules, Analytical Chemistry, 76 (2004) 6908-6914.

[26] A.E. Cohen, W.E. Moerner, Method for trapping and manipulating nanoscale objects in solution, Applied Physics Letters, 86 (2005) 093109.

[27] R. Probst, B. Shapiro, Three-dimensional electrokinetic tweezing: device design, modeling, and control algorithms, Journal of Micromechanics and Microengineering, 21 (2011) 027004.

[28] A.R. Bausch, W. Möller, E. Sackmann, Measurement of local viscoelasticity and forces in living cells by magnetic tweezers, Biophysical journal, 76 (1999) 573-579.

[29] N.M. Karabacak, P.S. Spuhler, F. Fachin, E.J. Lim, V. Pai, E. Ozkumur, J.M. Martel, N. Kojic, K. Smith, P.-i. Chen, J. Yang, H. Hwang, B. Morgan, J. Trautwein, T.A. Barber, S.L. Stott, S. Maheswaran, R. Kapur, D.A. Haber, M. Toner, Microfluidic, marker-free isolation of circulating tumor cells from blood samples, Nature protocols, 9 (2014) 694-710.

[30] F. Fachin, P. Spuhler, J.M. Martel-Foley, J.F. Edd, T.A. Barber, J. Walsh, M. Karabacak, V. Pai, M. Yu, K. Smith, H. Hwang, J. Yang, S. Shah, R. Yarmush, L.V. Sequist, S.L. Stott, S. Maheswaran, D.A. Haber, R. Kapur, M. Toner, Monolithic Chip for High-throughput Blood Cell Depletion to Sort Rare Circulating Tumor Cells, Scientific Reports, 7 (2017) 10936.

[31] X. Ding, Z. Peng, S.-C.S. Lin, M. Geri, S. Li, P. Li, Y. Chen, M. Dao, S. Suresh, T.J. Huang, Cell separation using tilted-angle standing surface acoustic waves,

Proceedings of the National Academy of Sciences of the United States of America, 111 (2014) 12992-12997.

[32] P. Li, Z. Mao, Z. Peng, L. Zhou, Y. Chen, P.-H. Huang, C.I. Truica, J.J. Drabick, W.S. El-Deiry, M. Dao, S. Suresh, T.J. Huang, Acoustic separation of circulating tumor cells, Proceedings of the National Academy of Sciences, 112 (2015) 4970.

[33] J. Shi, H. Huang, Z. Stratton, Y. Huang, T.J. Huang, Continuous particle separation in a microfluidic channelvia standing surface acoustic waves (SSAW), Lab on a Chip, 9 (2009) 3354-3359.

[34] D.J. Collins, B. Morahan, J. Garcia-Bustos, C. Doerig, M. Plebanski, A. Neild, Two-dimensional single-cell patterning with one cell per well driven by surface acoustic waves, Nature Communications, 6 (2015) 8686.

[35] F. Guo, Z. Mao, Y. Chen, Z. Xie, J.P. Lata, P. Li, L. Ren, J. Liu, J. Yang, M. Dao, S. Suresh, T.J. Huang, Three-dimensional manipulation of single cells using surface acoustic waves, Proceedings of the National Academy of Sciences, 113 (2016) 1522.

[36] Z. Mao, Y. Xie, F. Guo, L. Ren, P.-H. Huang, Y. Chen, J. Rufo, F. Costanzo, T.J. Huang, Experimental and numerical studies on standing surface acoustic wave microfluidics, Lab on a Chip, 16 (2016) 515-524.

[37] M.A. Burguillos, C. Magnusson, M. Nordin, A. Lenshof, P. Augustsson, M.J. Hansson, E. Elmér, H. Lilja, P. Brundin, T. Laurell, T. Deierborg, Microchannel Acoustophoresis does not Impact Survival or Function of Microglia, Leukocytes or Tumor Cells, PLOS ONE, 8 (2013) e64233.

[38] M. Wiklund, Acoustofluidics 12: Biocompatibility and cell viability in microfluidic acoustic resonators, Lab on a Chip, 12 (2012) 2018-2028.

[39] Y. Ai, C.K. Sanders, B.L. Marrone, Separation of Escherichia coli Bacteria from Peripheral Blood Mononuclear Cells Using Standing Surface Acoustic Waves, Analytical Chemistry, 85 (2013) 9126-9134.

[40] A. Carovac, F. Smajlovic, D. Junuzovic, Application of ultrasound in medicine, Acta informatica medica : AIM : journal of the Society for Medical Informatics of Bosnia & Herzegovina : casopis Drustva za medicinsku informatiku BiH, 19 (2011) 168-171.

[41] S.B. Barnett, G.R. Ter Haar, M.C. Ziskin, H.-D. Rott, F.A. Duck, K. Maeda, International recommendations and guidelines for the safe use of diagnostic ultrasound in medicine, Ultrasound in Medicine & Biology, 26 (2000) 355-366.

[42] J. Friend, L.Y. Yeo, Microscale acoustofluidics: Microfluidics driven via acoustics and ultrasonics, Reviews of Modern Physics, 83 (2011) 647-704.

[43] L.P. Gorkov, On the Forces Acting on a Small Particle in an Acoustical Field in an Ideal Fluid, 6 (1962) 773-775.

[44] B.A. Auld, Acoustic fields and waves in solids, John Wiley & Sons1973.

[45] X. Ding, P. Li, S.-C.S. Lin, Z.S. Stratton, N. Nama, F. Guo, D. Slotcavage, X. Mao, J. Shi, F. Costanzo, T.J. Huang, Surface acoustic wave microfluidics, Lab on a Chip, 13 (2013) 3626-3649.

[46] S.-C.S. Lin, X. Mao, T.J. Huang, Surface acoustic wave (SAW) acoustophoresis: now and beyond, Lab on a Chip, 12 (2012) 2766-2770.

[47] G.W. Farnell, E.L. Adler, 2 - Elastic Wave Propagation in Thin Layers, in: W.P. Mason, R.N. Thurston (Eds.) Physical Acoustics, Academic Press1972, pp. 35-127.

[48] H.F. Pollard, Sound Waves in Solids, Pion Limited, London, 1977.

[49] L.Y. Yeo, J.R. Friend, Surface Acoustic Wave Microfluidics, Annual Review of Fluid Mechanics, 46 (2014) 379-406.

[50] M. Gedge, M. Hill, Acoustofluidics 17: Theory and applications of surface acoustic wave devices for particle manipulation, Lab on a Chip, 12 (2012) 2998-3007.

[51] V. Yantchev, J. Enlund, I. Katardjiev, L. Johansson, A micromachined Stoneley acoustic wave system for continuous flow particle manipulation in microfluidic channels, Journal of Micromechanics and Microengineering, 20 (2010) 035031.

[52] K. Dransfeld, E. Salzmann, 4 - Excitation, Detection, and Attenuation of High-Frequency Elastic Surface Waves, in: W.P. Mason, R.N. Thurston (Eds.) Physical Acoustics, Academic Press1970, pp. 219-272.

[53] J.D.N. Cheeke, Fundamentals and Applications of Ultrasonic Waves, CRC Press2002.

[54] D.J. Collins, Z. Ma, J. Han, Y. Ai, Continuous micro-vortex-based nanoparticle manipulation via focused surface acoustic waves, Lab on a Chip, 17 (2017) 91-103.

[55] R. Barnkob, P. Augustsson, T. Laurell, H. Bruus, Acoustic radiation- and streaming-induced microparticle velocities determined by microparticle image

velocimetry in an ultrasound symmetry plane, Physical Review E, 86 (2012) 056307.

[56] M. Wiklund, R. Green, M. Ohlin, Acoustofluidics 14: Applications of acoustic streaming in microfluidic devices, Lab on a Chip, 12 (2012) 2438-2451.

[57] N. Riley, STEADY STREAMING, Annual Review of Fluid Mechanics, 33 (2001) 43-65.

[58] C. Eckart, Vortices and Streams Caused by Sound Waves, Physical Review, 73 (1948) 68-76.

[59] D.J. Collins, Z. Ma, Y. Ai, Highly Localized Acoustic Streaming and Size-Selective Submicrometer Particle Concentration Using High Frequency Microscale Focused Acoustic Fields, Analytical Chemistry, 88 (2016) 5513-5522.

[60] M.B. Dentry, L.Y. Yeo, J.R. Friend, Frequency effects on the scale and behavior of acoustic streaming, Physical Review E, 89 (2014) 013203.

[61] S. Li, X. Ding, F. Guo, Y. Chen, M.I. Lapsley, S.-C.S. Lin, L. Wang, J.P. McCoy, C.E. Cameron, T.J. Huang, An On-Chip, Multichannel Droplet Sorter Using Standing Surface Acoustic Waves, Analytical Chemistry, 85 (2013) 5468-5474.

[62] D.J. Collins, A. Neild, Y. Ai, Highly focused high-frequency travelling surface acoustic waves (SAW) for rapid single-particle sorting, Lab on a Chip, 16 (2016) 471-479.

[63] H. Schlichting, Berechnung ebener periodischer Grenzschichtstromungen, Physikalische Zeit., 33 (1932) 327-335.

[64] L.D. Landau, E.M. Lifshitz, Fluid Mechanics, Course of Theoretical Physics, Butterworth-Heinemann2006.

[65] V.F.K. Bjerknes, Fields of Force, Columbia University Press, New York, 1906.

[66] V. King Louis, On the acoustic radiation pressure on spheres, Proceedings of the Royal Society of London. Series A - Mathematical and Physical Sciences, 147 (1934) 212-240.

[67] K. Yosioka, Y. Kawasima, Acoustic radiation pressure on a compressible sphere, Acta Acustica united with Acustica, 5 (1955) 167-173.

[68] T. Hasegawa, K. Yosioka, Acoustic-Radiation Force on a Solid Elastic Sphere, The Journal of the Acoustical Society of America, 46 (1969) 1139-1143.

[69] T. Hasegawa, Comparison of two solutions for acoustic radiation pressure on a sphere, The Journal of the Acoustical Society of America, 61 (1977) 1445-1448.

[70] T. Hasegawa, Acoustic radiation force on a sphere in a quasistationary wave field—theory, The Journal of the Acoustical Society of America, 65 (1979) 32-40.

[71] M. Settnes, H. Bruus, Forces acting on a small particle in an acoustical field in a viscous fluid, Physical Review E, 85 (2012) 016327.

[72] T. Hasegawa, Y. Watanabe, Acoustic radiation pressure on an absorbing sphere, The Journal of the Acoustical Society of America, 63 (1978) 1733-1737.

[73] P. Glynne-Jones, P.P. Mishra, R.J. Boltryk, M. Hill, Efficient finite element modeling of radiation forces on elastic particles of arbitrary size and geometry, The Journal of the Acoustical Society of America, 133 (2013) 1885-1893.

[74] R. Habibi, C. Devendran, A. Neild, Trapping and patterning of large particles and cells in a 1D ultrasonic standing wave, Lab on a Chip, 17 (2017) 3279-3290.

[75] E. Hanukah, Higher order closed-form model for isotropic hyperelastic spherical shell (3D solid), arXiv e-prints2013.

[76] H. Bruus, Acoustofluidics 2: Perturbation theory and ultrasound resonance modes, Lab on a Chip, 12 (2012) 20-28.

[77] J. Karlsen, P. Augustsson, H. Bruus, Acoustic Force Density Acting on Inhomogeneous Fluids in Acoustic Fields, 2016.

[78] S. Oberti, A. Neild, J. Dual, Manipulation of micrometer sized particles within a micromachined fluidic device to form two-dimensional patterns using ultrasound, The Journal of the Acoustical Society of America, 121 (2007) 778-785.

[79] C. Devendran, T. Albrecht, J. Brenker, T. Alan, A. Neild, The importance of travelling wave components in standing surface acoustic wave (SSAW) systems, Lab on a Chip, 16 (2016) 3756-3766.

[80] J.K. Tsou, J. Liu, A.I. Barakat, M.F. Insana, Role of Ultrasonic Shear Rate Estimation Errors in Assessing Inflammatory Response and Vascular Risk, Ultrasound in Medicine & Biology, 34 (2008) 963-972.

[81] Y. Xia, G.M. Whitesides, SOFT LITHOGRAPHY, Annual Review of Materials Science, 28 (1998) 153-184.

[82] X.Y. Du, Y.Q. Fu, J.K. Luo, A.J. Flewitt, W.I. Milne, Microfluidic pumps employing surface acoustic waves generated in ZnO thin films, Journal of Applied Physics, 105 (2009) 024508.

[83] J. Nam, C.S. Lim, A conductive liquid-based surface acoustic wave device, Lab on a Chip, 16 (2016) 3750-3755.

[84] E.P. Diamandis, T.K. Christopoulos, The biotin-(strept)avidin system: principles and applications in biotechnology, Clinical Chemistry, 37 (1991) 625.

[85] E.S. Asmolov, The inertial lift on a spherical particle in a plane Poiseuille flow at large channel Reynolds number, Journal of Fluid Mechanics, 381 (1999) 63-87.

[86] S. Mittal, I.Y. Wong, A.A. Yanik, W.M. Deen, M. Toner, Discontinuous Nanoporous Membranes Reduce Non-Specific Fouling for Immunoaffinity Cell Capture, Small, 9 (2013) 4207-4214.

[87] S. Mittal, Ian Y. Wong, William M. Deen, M. Toner, Antibody-Functionalized Fluid-Permeable Surfaces for Rolling Cell Capture at High Flow Rates, Biophysical Journal, 102 (2012) 721-730.

[88] R. Mukhopadhyay, When Microfluidic Devices Go Bad, Analytical Chemistry, 77 (2005) 429 A-432 A.

[89] M. Ali, A.L. Lopez, Y. You, Y.E. Kim, B. Sah, B. Maskery, J. Clemens, The global burden of cholera, 2012.

[90] K. Diaconu, J. Falconer, F. O'May, M. Jimenez, J. Matragrano, B. Njanpop-Lafourcade, A. Ager, Cholera diagnosis in human stool and detection in water: protocol for a systematic review of available technologies, Systematic reviews, 7 (2018) 29-29.

[91] J. Perez-Saez, A.A. King, A. Rinaldo, M. Yunus, A.S.G. Faruque, M. Pascual, Climate-driven endemic cholera is modulated by human mobility in a megacity, Advances in Water Resources, 108 (2017) 367-376.

[92] M. Phelps, M.L. Perner, V.E. Pitzer, V. Andreasen, P.K.M. Jensen, L. Simonsen, Cholera Epidemics of the Past Offer New Insights Into an Old Enemy, The Journal of infectious diseases, 217 (2018) 641-649.

[93] J. Mandal, K.P. Dinoop, S.C. Parija, Increasing antimicrobial resistance of Vibrio cholerae OI biotype E1 tor strains isolated in a tertiary-care centre in India, Journal of health, population, and nutrition, 30 (2012) 12-16.

[94] J.P. Burnham, M.A. Olsen, M.H. Kollef, Re-estimating annual deaths due to multidrug-resistant organism infections, Infection Control & Hospital Epidemiology, 40 (2019) 112-113.

[95] E. Endarko, M. Maclean, I.V. Timoshkin, S.J. MacGregor, J.G. Anderson, High-Intensity 405 nm Light Inactivation of Listeria monocytogenes, Photochemistry and Photobiology, 88 (2012) 1280-1286.

[96] M.-J. Kim, M. Mikš-Krajnik, A. Kumar, V. Ghate, H.-G. Yuk, Antibacterial effect and mechanism of high-intensity 405±5nm light emitting diode on Bacillus cereus, Listeria monocytogenes, and Staphylococcus aureus under refrigerated condition, Journal of Photochemistry and Photobiology B: Biology, 153 (2015) 33-39.

[97] M. Maclean, K. McKenzie, J.G. Anderson, G. Gettinby, S.J. MacGregor, 405 nm light technology for the inactivation of pathogens and its potential role for

environmental disinfection and infection control, Journal of Hospital Infection, 88 (2014) 1-11.

[98] K. McKenzie, M. Maclean, I.V. Timoshkin, E. Endarko, S.J. MacGregor, J.G. Anderson, Photoinactivation of Bacteria Attached to Glass and Acrylic Surfaces by 405 nm Light: Potential Application for Biofilm Decontamination, Photochemistry and Photobiology, 89 (2013) 927-935.

[99] T. Dai, The antimicrobial effect of blue light: What are behind?, Virulence, 8 (2017) 649-652.

[100] M. Maclean, S.J. MacGregor, J.G. Anderson, G. Woolsey, Inactivation of Bacterial Pathogens following Exposure to Light from a 405-Nanometer Light-Emitting Diode Array, Applied and Environmental Microbiology, 75 (2009) 1932.

[101] M.W. Knight, N.S. King, L. Liu, H.O. Everitt, P. Nordlander, N.J. Halas, Aluminum for Plasmonics, ACS Nano, 8 (2014) 834-840.

[102] M.W. Knight, L. Liu, Y. Wang, L. Brown, S. Mukherjee, N.S. King, H.O. Everitt, P. Nordlander, N.J. Halas, Aluminum Plasmonic Nanoantennas, Nano Letters, 12 (2012) 6000-6004.

[103] V. Giannini, A.I. Fernández-Domínguez, S.C. Heck, S.A. Maier, Plasmonic Nanoantennas: Fundamentals and Their Use in Controlling the Radiative Properties of Nanoemitters, Chemical Reviews, 111 (2011) 3888-3912.

[104] A. Kinkhabwala, Z. Yu, S. Fan, Y. Avlasevich, K. Müllen, W.E. Moerner, Large single-molecule fluorescence enhancements produced by a bowtie nanoantenna, Nature Photonics, 3 (2009) 654.

[105] K.A. Willets, R.P. Van Duyne, Localized Surface Plasmon Resonance Spectroscopy and Sensing, Annual Review of Physical Chemistry, 58 (2007) 267-297.

[106] H.A. Atwater, A. Polman, Plasmonics for improved photovoltaic devices, Nature Materials, 9 (2010) 205.

[107] S. Lal, S. Link, N.J. Halas, Nano-optics from sensing to waveguiding, Nature Photonics, 1 (2007) 641.

[108] E. Ozbay, Plasmonics: Merging Photonics and Electronics at Nanoscale Dimensions, Science, 311 (2006) 189.

[109] J.N. Anker, W.P. Hall, O. Lyandres, N.C. Shah, J. Zhao, R.P. Van Duyne, Biosensing with plasmonic nanosensors, Nature Materials, 7 (2008) 442.

[110] R. Adato, A.A. Yanik, J.J. Amsden, D.L. Kaplan, F.G. Omenetto, M.K. Hong, S. Erramilli, H. Altug, Ultra-sensitive vibrational spectroscopy of protein monolayers with plasmonic nanoantenna arrays, Proceedings of the National Academy of Sciences, 106 (2009) 19227.

[111] R. Adato, A.A. Yanik, C.-H. Wu, G. Shvets, H. Altug, Radiative engineering of plasmon lifetimes in embedded nanoantenna arrays, Opt. Express, 18 (2010) 4526-4537.

[112] V.G. Kravets, A.V. Kabashin, W.L. Barnes, A.N. Grigorenko, Plasmonic Surface Lattice Resonances: A Review of Properties and Applications, Chemical Reviews, 118 (2018) 5912-5951.

[113] B. Auguié, W.L. Barnes, Collective Resonances in Gold Nanoparticle Arrays, Physical Review Letters, 101 (2008) 143902.

[114] J.W. Bandler, Q.S. Cheng, S.A. Dakroury, A.S. Mohamed, M.H. Bakr, K. Madsen, J. Sondergaard, Space mapping: the state of the art, IEEE Transactions on Microwave Theory and Techniques, 52 (2004) 337-361.

[115] S. Koziel, Q.S. Cheng, J.W. Bandler, Space mapping, IEEE Microwave Magazine, 9 (2008) 105-122.

[116] M.H. Chowdhury, K. Ray, S.K. Gray, J. Pond, J.R. Lakowicz, Aluminum Nanoparticles as Substrates for Metal-Enhanced Fluorescence in the Ultraviolet for the Label-Free Detection of Biomolecules, Analytical Chemistry, 81 (2009) 1397-1403.

[117] V. Canalejas-Tejero, S. Herranz, A. Bellingham, M.C. Moreno-Bondi, C.A. Barrios, Passivated Aluminum Nanohole Arrays for Label-Free Biosensing Applications, ACS Applied Materials & Interfaces, 6 (2014) 1005-1010.

[118] M. Lee, J.U. Kim, K.J. Lee, S. Ahn, Y.-B. Shin, J. Shin, C.B. Park, Aluminum Nanoarrays for Plasmon-Enhanced Light Harvesting, ACS Nano, 9 (2015) 6206-6213.

[119] L. Zhou, C. Zhang, M.J. McClain, A. Manjavacas, C.M. Krauter, S. Tian, F. Berg, H.O. Everitt, E.A. Carter, P. Nordlander, N.J. Halas, Aluminum Nanocrystals as

a Plasmonic Photocatalyst for Hydrogen Dissociation, Nano Letters, 16 (2016) 1478-1484.

[120] P.R. West, S. Ishii, G.V. Naik, N.K. Emani, V.M. Shalaev, A. Boltasseva, Searching for better plasmonic materials, Laser & Photonics Reviews, 4 (2010) 795-808.

[121] M.B. Ross, G.C. Schatz, Radiative effects in plasmonic aluminum and silver nanospheres and nanorods, Journal of Physics D: Applied Physics, 48 (2014) 184004.

[122] I. Zorić, M. Zäch, B. Kasemo, C. Langhammer, Gold, Platinum, and Aluminum Nanodisk Plasmons: Material Independence, Subradiance, and Damping Mechanisms, ACS Nano, 5 (2011) 2535-2546.

[123] N. Cabrera, N.F. Mott, Theory of the oxidation of metals, Reports on Progress in Physics, 12 (1949) 163-184.

[124] E. Prodan, C. Radloff, N.J. Halas, P. Nordlander, A Hybridization Model for the Plasmon Response of Complex Nanostructures, Science, 302 (2003) 419.

[125] N.J. Halas, S. Lal, W.-S. Chang, S. Link, P. Nordlander, Plasmons in Strongly Coupled Metallic Nanostructures, Chemical Reviews, 111 (2011) 3913-3961.

[126] P. Nordlander, C. Oubre, E. Prodan, K. Li, M.I. Stockman, Plasmon Hybridization in Nanoparticle Dimers, Nano Letters, 4 (2004) 899-903.

[127] M.B. Ross, G.C. Schatz, Aluminum and Indium Plasmonic Nanoantennas in the Ultraviolet, The Journal of Physical Chemistry C, 118 (2014) 12506-12514.

[128] V.G. Kravets, F. Schedin, A.N. Grigorenko, Extremely Narrow Plasmon Resonances Based on Diffraction Coupling of Localized Plasmons in Arrays of Metallic Nanoparticles, Physical Review Letters, 101 (2008) 087403.

[129] L. Zhao, K.L. Kelly, G.C. Schatz, The Extinction Spectra of Silver Nanoparticle Arrays: Influence of Array Structure on Plasmon Resonance Wavelength and Width, The Journal of Physical Chemistry B, 107 (2003) 7343-7350.

[130] S. Zou, N. Janel, G.C. Schatz, Silver nanoparticle array structures that produce remarkably narrow plasmon lineshapes, The Journal of Chemical Physics, 120 (2004) 10871-10875.

[131] C. Langhammer, M. Schwind, B. Kasemo, I. Zorić, Localized Surface Plasmon Resonances in Aluminum Nanodisks, Nano Letters, 8 (2008) 1461-1471.

[132] T. Jensen, L. Kelly, A. Lazarides, G.C. Schatz, Electrodynamics of Noble Metal Nanoparticles and Nanoparticle Clusters, Journal of Cluster Science, 10 (1999) 295-317.

[133] M. Meier, A. Wokaun, Enhanced fields on large metal particles: dynamic depolarization, Opt. Lett., 8 (1983) 581-583.

[134] S.A. Maier, Plasmonics: Fundamentals and Applications, Springer Science & Business Media2007.

[135] D.E. Gómez, Y. Hwang, J. Lin, T.J. Davis, A. Roberts, Plasmonic Edge States: An Electrostatic Eigenmode Description, ACS Photonics, 4 (2017) 1607-1614.

[136] J. Li, J. Ye, C. Chen, L. Hermans, N. Verellen, J. Ryken, H. Jans, W. Van Roy, V.V. Moshchalkov, L. Lagae, P. Van Dorpe, Biosensing Using Diffractively

Coupled Plasmonic Crystals: the Figure of Merit Revisited, Advanced Optical Materials, 3 (2015) 176-181.

[137] B.D. Thackray, V.G. Kravets, F. Schedin, G. Auton, P.A. Thomas, A.N. Grigorenko, Narrow Collective Plasmon Resonances in Nanostructure Arrays Observed at Normal Light Incidence for Simplified Sensing in Asymmetric Air and Water Environments, ACS Photonics, 1 (2014) 1116-1126.

[138] E. Palik, Handbook of Optical Constants of Solids; , Academic: New York1985.

[139] M.H. Bakr, J.W. Bandler, K. Madsen, J. Søndergaard, Review of the Space Mapping Approach to Engineering Optimization and Modeling, Optimization and Engineering, 1 (2000) 241-276.

[140] M. George, S. Nielson, R. Petrova, J. Frasier, E. Gardner, Wafer-scale aluminum nano-plasmonics, 2014.

[141] C. Dahmen, B. Schmidt, G. von Plessen, Radiation Damping in Metal Nanoparticle Pairs, Nano Letters, 7 (2007) 318-322.

[142] M. Berney, H.U. Weilenmann, A. Simonetti, T. Egli, Efficacy of solar disinfection of Escherichia coli, Shigella flexneri, Salmonella Typhimurium and Vibrio cholerae, Journal of Applied Microbiology, 101 (2006) 828-836.

[143] G. Baffou, R. Quidant, C. Girard, Heat generation in plasmonic nanostructures: Influence of morphology, Applied Physics Letters, 94 (2009) 153109.

[144] K.L. Meibom, M. Blokesch, N.A. Dolganov, C.-Y. Wu, G.K. Schoolnik, Chitin Induces Natural Competence in <em>Vibrio cholerae</em&gt, Science, 310 (2005) 1824.

[145] A.S. Utada, R.R. Bennett, J.C.N. Fong, M.L. Gibiansky, F.H. Yildiz, R. Golestanian, G.C.L. Wong, Vibrio cholerae use pili and flagella synergistically to effect motility switching and conditional surface attachment, Nature Communications, 5 (2014) 4913.

[146] S. Beyhan, K. Bilecen, S.R. Salama, C. Casper-Lindley, F.H. Yildiz, Regulation of rugosity and biofilm formation in Vibrio cholerae: comparison of VpsT and VpsR regulons and epistasis analysis of vpsT, vpsR, and hapR, Journal of bacteriology, 189 (2007) 388-402.

[147] F.H. Yildiz, X.S. Liu, A. Heydorn, G.K. Schoolnik, Molecular analysis of rugosity in a Vibrio cholerae O1 El Tor phase variant, Molecular Microbiology, 53 (2004) 497-515.

[148] T. Imasaka, Y. Kawabata, T. Kaneta, Y. Ishidzu, Optical chromatography, Anal. Chem., 67 (1995) 1763-1765.

[149] C.G. Hebert, A. Terray, S.J. Hart, Toward Label-Free Optical Fractionation of Blood-Optical Force Measurements of Blood Cells, Anal. Chem., 83 (2011) 5666-5672.

[150] Z. Ma, K.J.L. Burg, Y. Wei, X.-C. Yuan, X. Peng, B.Z. Gao, Laser-guidance based detection of cells with single-gene modification, Appl. Phys. Lett., 92 (2008) 213902.

[151] S.J. Hart, A. Terray, T.A. Leski, J. Arnold, R. Stroud, Discovery of a Significant Optical Chromatographic Difference between Spores of Bacillus anthracis and Its Close Relative, Bacillus thuringiensis, Anal. Chem., 78 (2006) 3221-3225.

[152] T. Kaneta, Y. Ishidzu, N. Mishima, T. Imasaka, Theory of optical chromatography, Anal. Chem., 69 (1997) 2701-2710.

[153] J. Makihara, T. Kaneta, T. Imasaka, Optical chromatography: Size determination by eluting particles, Talanta., 48 (1999) 551-557.

[154] S.J. Hart, A.V. Terray, Refractive-index-driven separation of colloidal polymer particles using optical chromatography, Appl. Phys. Lett., 83 (2003) 5316-5318.

[155] J.D. Taylor, A. Terray, S.J. Hart, Analytical particle measurements in an optical microflume, Anal. Chim. Acta., 670 (2010) 78-83.

[156] A. Terray, C.G. Hebert, S.J. Hart, Optical chromatographic sample separation of hydrodynamically focused mixtures, Biomicrofluidics., 8 (2014) 064102.

[157] A. Terray, J.D. Taylor, S.J. Hart, Cascade optical chromatography for sample fractionation, Biomicrofluidics., 3 (2009) 044106.

[158] L. Verslegers, P.B. Catrysse, Z. Yu, J.S. White, E.S. Barnard, M.L. Brongersma, S. Fan, Planar lenses based on nanoscale slit arrays in a metallic film, Nano. Lett., 9 (2008) 235-238.

[159] F.M. Huang, T.S. Kao, V.A. Fedotov, Y. Chen, N.I. Zheludev, Nanohole array as a lens, Nano. Lett., 8 (2008) 2469-2472.

[160] H. Gao, J.K. Hyun, M.H. Lee, J.-C. Yang, L.J. Lauhon, T.W. Odom, Broadband plasmonic microlenses based on patches of nanoholes, Nano. Lett., 10 (2010) 4111-4116.

[161] A. Ashkin, Acceleration and trapping of particles by radiation pressure, Phys. Rev. Lett., 24 (1970) 156.

[162] A. Ashkin, J. Dziedzic, Optical trapping and manipulation of viruses and bacteria, Science., 235 (1987) 1517-1520.

[163] A.A. Yanik, A.E. Cetin, M. Huang, A. Artar, S.H. Mousavi, A. Khanikaev, J.H. Connor, G. Shvets, H. Altug, Seeing protein monolayers with naked eye through plasmonic Fano resonances, Proc. Natl. Acad. Sci., (2011).

[164] T.W. Ebbesen, H.J. Lezec, H.F. Ghaemi, T. Thio, P.A. Wolff, Extraordinary optical transmission through sub-wavelength hole arrays, Nature., 391 (1998) 667-669.

[165] Mart, iacute, L. n-Moreno, Garc, F.J. a-Vidal, H.J. Lezec, K.M. Pellerin, T. Thio, J.B. Pendry, T.W. Ebbesen, Theory of Extraordinary Optical Transmission through Subwavelength Hole Arrays, Phys. Rev. Lett. , 86 (2001) 1114.

[166] C. Genet, T.W. Ebbesen, Light in tiny holes, Nature., 445 (2007) 39-46.

[167] A.A. Yanik, X. Wang, S. Erramilli, M.K. Hong, H. Altug, Extraordinary midinfrared transmission of rectangular coaxial nanoaperture arrays, Appl. Phys. Lett., 93 (2008) 081104-081103.

[168] A.A. Yanik, M. Huang, A. Artar, T.-Y. Chang, H. Altug, Integrated nanoplasmonic-nanofluidic biosensors with targeted delivery of analytes, Appl. Phys. Lett., 96 (2010) 021101-021103.

[169] M. Huang, A.A. Yanik, T.-Y. Chang, H. Altug, Sub-wavelength nanofluidics in photonic crystal sensors, Opt. Express., 17 (2009) 24224-24233.

[170] K.W. Oh, K. Lee, B. Ahn, E.P. Furlani, Design of pressure-driven microfluidic networks using electric circuit analogy, Lab. Chip., 12 (2012) 515-545.

[171] M.R. Dennis, N.I. Zheludev, F.J.G. de Abajo, The plasmon Talbot effect, Opt. Express., 15 (2007) 9692-9700.

[172] H.F. Ghaemi, T. Thio, D.E. Grupp, T.W. Ebbesen, H.J. Lezec, Surface plasmons enhance optical transmission through subwavelength holes, Phys. Rev. B., 58 (1998) 6779.

[173] P. Ruffieux, T. Scharf, H.P. Herzig, R. Völkel, K.J. Weible, On the chromatic aberration of microlenses, Opt. Express., 14 (2006) 4687-4694.

[174] S. Saxena, R.P. Chaudhary, A. Singh, S. Awasthi, S. Shukla, Plasmonic Micro Lens for Extraordinary Transmission of Broadband Light, Sci. Rep., 4 (2014).

[175] K. Okamoto, S. Kawata, Radiation force exerted on subwavelength particles near a nanoaperture, Phys. Rev. Lett., 83 (1999) 4534.

[176] X. Wang, X.-B. Wang, P.R. Gascoyne, General expressions for dielectrophoretic force and electrorotational torque derived using the Maxwell stress tensor method, J. Electrostat., 39 (1997) 277-295.

[177] G. Baffou, C. Girard, R. Quidant, Mapping Heat Origin in Plasmonic Structures, Phys. Rev. Lett., 104 (2010) 136805.

[178] J.S. Donner, G. Baffou, D. McCloskey, R. Quidant, Plasmon-Assisted Optofluidics, ACS. Nano., 5 (2011) 5457-5462.

[179] J. Kim, Joining plasmonics with microfluidics: from convenience to inevitability, Lab. Chip., 12 (2012) 3611-3623.

[180] B.J. Roxworthy, A.M. Bhuiya, S.P. Vanka, K.C. Toussaint Jr, Understanding and controlling plasmon-induced convection, Nat. Commun., 5 (2014) 3173.

[181] J.D. Jackson, Classical Electrodynamics, John Wiley and Sons, Hoboken, NJ, 1999.

[182] J.C. Ndukaife, A.V. Kildishev, A.G.A. Nnanna, V.M. Shalaev, S.T. Wereley, A. Boltasseva, Long-range and rapid transport of individual nano-objects by a hybrid electrothermoplasmonic nanotweezer, Nat. Nanotechnol., 11 (2015) 53.

[183] E. van der Pol, L. de Rond, F.A.W. Coumans, E.L. Gool, A.N. Böing, A. Sturk, R. Nieuwland, T.G. van Leeuwen, Absolute sizing and label-free identification of extracellular vesicles by flow cytometry, Nanomedicine., 14 (2018) 801-810.

[184] E. van der Pol, F. Coumans, Z. Varga, M. Krumrey, R. Nieuwland, Innovation in detection of microparticles and exosomes, J. Thromb. Haemost., 11 (2013) 36-45.

[185] C. Gardiner, M. Shaw, P. Hole, J. Smith, D. Tannetta, C.W. Redman, I.L. Sargent, Measurement of refractive index by nanoparticle tracking analysis reveals heterogeneity in extracellular vesicles, J. Extracell. Vesicles., 3 (2014) 25361.

[186] S. Wang, X. Shan, U. Patel, X. Huang, J. Lu, J. Li, N. Tao, Label-free imaging, detection, and mass measurement of single viruses by surface plasmon resonance, Proc. Natl. Acad. Sci., 107 (2010) 16028-16032.

[187] H.B. Steen, Flow cytometer for measurement of the light scattering of viral and other submicroscopic particles, Cytometry. A., 57A (2004) 94-99.

[188] R. Vogel, G. Willmott, D. Kozak, G.S. Roberts, W. Anderson, L. Groenewegen, B. Glossop, A. Barnett, A. Turner, M. Trau, Quantitative Sizing of

Nano/Microparticles with a Tunable Elastomeric Pore Sensor, Anal. Chem., 83 (2011) 3499-3506.

[189] E. van der Pol, F.A.W. Coumans, A.E. Grootemaat, C. Gardiner, I.L. Sargent, P. Harrison, A. Sturk, T.G. van Leeuwen, R. Nieuwland, Particle size distribution of exosomes and microvesicles determined by transmission electron microscopy, flow cytometry, nanoparticle tracking analysis, and resistive pulse sensing, J. Thromb. Haemost., 12 (2014) 1182-1192.

[190] S. Mittal, I.Y. Wong, A.A. Yanik, W.M. Deen, M. Toner, Discontinuous Nanoporous Membranes Reduce Non-Specific Fouling for Immunoaffinity Cell Capture, Small., 9 (2013) 4207-4214.